PB98-112337

DEVELOPMENT OF FIBER OPTIC DYNAMIC WEIGHT-IN-MOTION SYSTEMS. FINAL REPORT

AUG 97

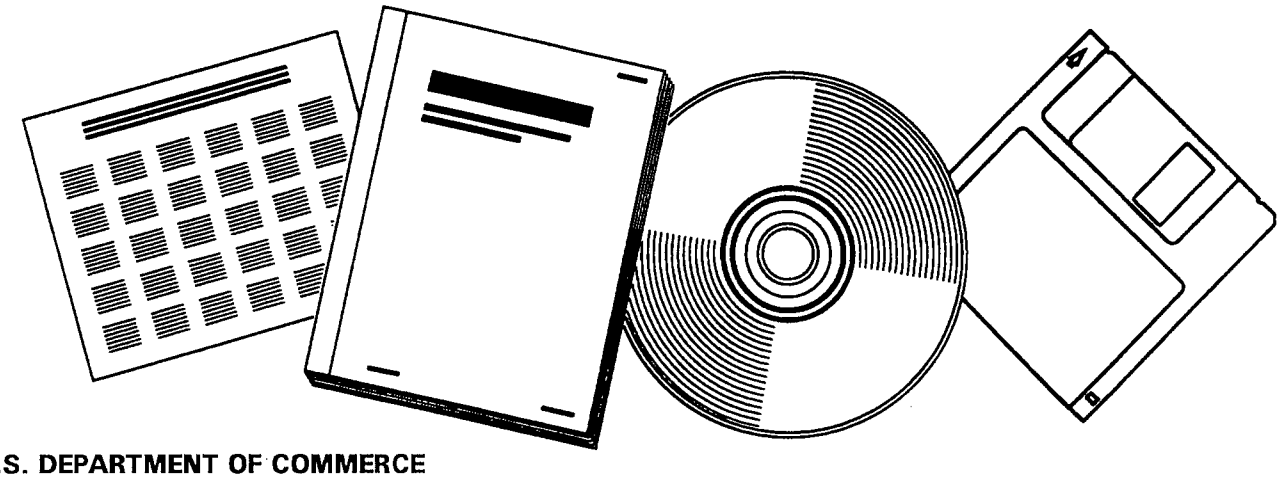

U.S. DEPARTMENT OF COMMERCE
National Technical Information Service

Final Report

Development of Fiber Optic Dynamic Weigh-in-Motion Systems

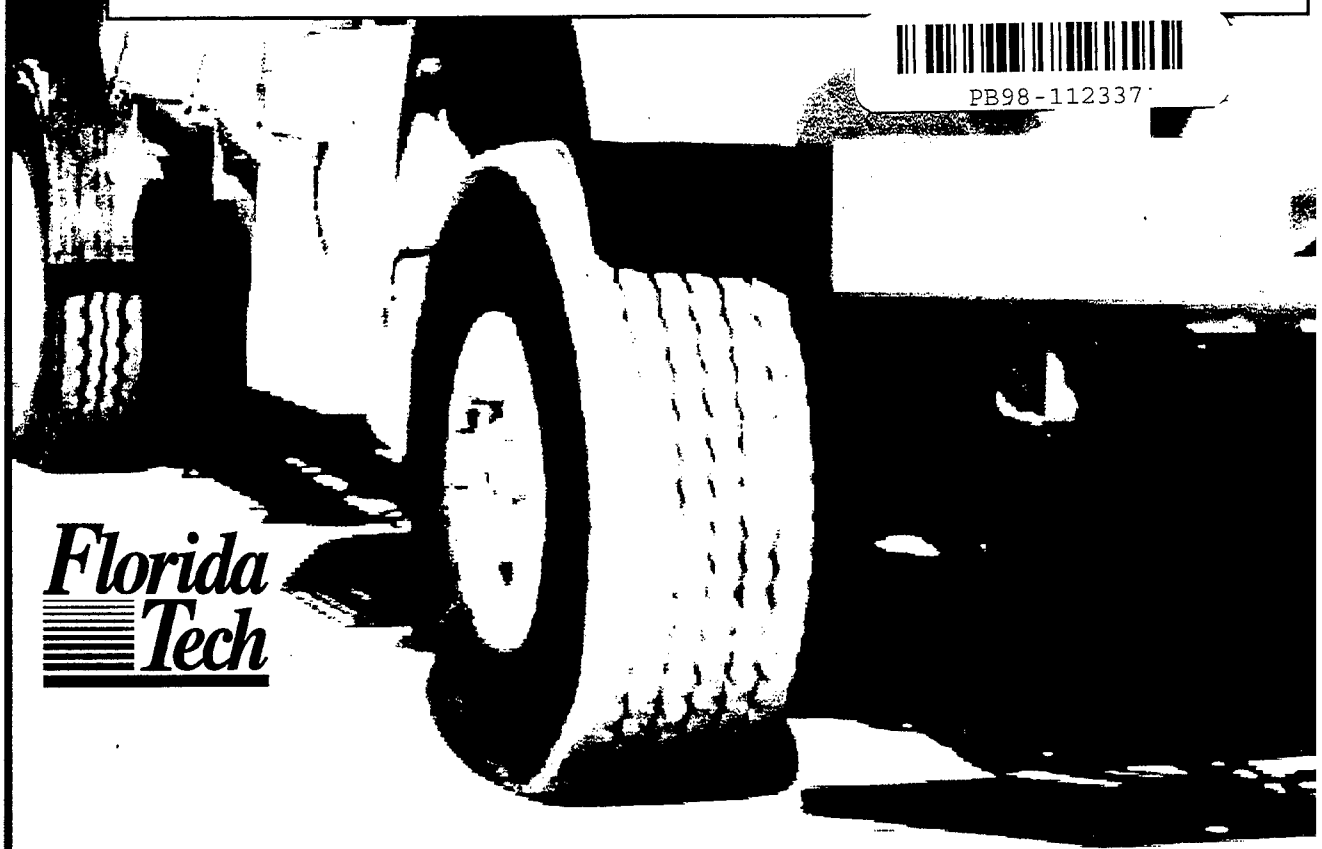

Florida Tech

August, 1997

Paul J. Cosentino, Ph.D., P.E., Principal Investigator
Barry G. Grossman, Ph.D., Co-Principal Investigator

Submitted to Administrator, Transportation Statistics Office
Florida Department of Transportation, Tallahassee Florida 32399-0450
(904) 488-4111 • SunCom: 278-4111 • Fax: (904) 488-4752
WPA Item Number 0510726 • Contract Number BA021
State Job Number 99700-3303-010

Florida Institute of Technology
150 West University Blvd.
Melbourne, Florida 32901-6975
(407) 674-7555

Technical Report Documentation Page

1. Report No.	2. Government Accession No.	3. Recipient's Catalog No.
WPA Item Number 0510726		

4. Title and Subtitle	5. Report Date
Development of Fiber Optic Dynamic Weigh-in-Motion System	October 3, 1997
	6. Performing Organization Code
	8. Performing Organization Report No.
7. Author's	
P. J. Cosentino, B. G. Grossman	
9. Performing Organization Name and Address	10. Work Unit No. (TRAIS)
Florida Institute of Technology (407) 674-7555 Civil Engineering Program 150 West University Blvd. Melbourne, FL 32901-6988	11. Contract or Grant No. BA-021
12. Sponsoring Agency Name and Address	13. Type of Report and Period Covered
Florida Department of Transportation 605 Suwannee Street Tallahassee, Florida 32399-0450	Final Report January 1996 to October 1997
	14. Sponsoring Agency Code 99700-3303-010

15. Supplementary Notes

16. Abstract

Flexible fiber optic sensors were successfully deployed in both flexible and rigid pavements subjected to heavy truck traffic. Vehicles were classified and weighed in both pavement types. The sensors, manufactured in any desirable lengths are about 0.25 inches (7 mm) wide by 0.0625 inches (1.7 mm) thick. For vehicle classification and weigh-in-motion (WIM) sensors are typically constructed 6 to 7 feet (1.8 to 2.1 m) long. These sensors were epoxied into pavement grooves, covered with a flexible filler material and the leads were connected to a specially designed optical-electronic box. The optical-electronic interface contains light emitting diodes that focus the light into the core of the optical fiber and photodetection equipment that converts light intensity to voltage. Voltage can then be used either for WIM or vehicle classification. Sharp, clear signals were obtained using the system developed. They show changes in light intensity for each single or dual tire assembly that passes over the sensor. The intensity changes vary according to the load on the tire and the vehicle speed. The fiber-optic system can be manufactured for costs comparable to piezoelectric sensor systems. It is noncorrosive and unaffected by power surges.

Laboratory tests were developed to categorize the engineering behavior the sensors and the materials used in sensor construction. A static compression test was developed that yielded load versus light intensity curves at any location along the length of the sensors. A second test was developed to categorize the variation in sensor response along its length. A motorized and weighted cart was guided along the sensor while light intensity variations were monitored. This test yielded light intensity versus sensor position data, that showed the repeatability of the signal versus location on the sensor. A new fiber failure test was developed to determine the breaking strength of the various fiber and mesh microbend combinations. An optical time domain reflectometer was used to determine the load at which the optical fiber would break during compression. The test results showed that Tefzel® mesh was preferred over polypropylene, nylon and polyester meshes because it yielded the highest fiber failure load.

Five sensors were placed in field sites subjected to controlled heavy truck repititions. In January 1997, three sensors were placed in the Portland cement concrete entrance road of a local ready-mix concrete plant. About 1,000 trucks use this road monthly. To date over 8,000 trucks have passed over these sensors. In June 1997, two sensors were placed in the asphalt-concrete entrance road of a local hot-mix plant that rents space to a second ready mix concrete company. Approximately 2,000 trucks use this access road monthly. These sensors experienced from 2,000 to 4,000 heavy trucks. As of August 21, 1997 three of the five sensors had failed. One sensor, placed 0.3 inches (9 mm) below the surface, in the rigid pavement failed in mid-August. The two remaining sensors were placed at depths of 0.5 (13 mm) and 0.85 (26 mm) below the surface. Both sensors placed in the asphalt-concrete pavement failed within a two month period. Causes of the failures are under investigation. Failure may have resulted from the heavy loads, or poor field installation techniques.

17. Key Words	18. Distribution Statement
Fiber optic sensors, Microbend, Traffic classification, Axle counts, Axle weights	Document is available to the U.S. public through the National Technical Information Service, Springfield, Virginia 22161

19. Security Classif. (of this report)	20. Security Classif. (of this page)	21. No of Pages	22. Price
Unclassified	Unclassified	153	

Form DOT 1700.7 (8-72)

Reproduction of completed page authorized

Table of Contents

List of Figures

List of Tables

CHAPTER 1

1.0 INTRODUCTION

1.1 PROBLEM DESCRIPTION

Pavement and traffic management systems are critical to proper maintenance of any highway system. Passage of the Intermodal Surface Transportation Efficiency Act in 1992 requires that traffic and pavement management techniques be implemented on all types of roadways, from major arterials managed by the state to local streets managed by cities and counties. To properly manage these systems, the number of vehicles, vehicle types, speeds, weights and pavement layer conditions are required. This tabulation of data requires the use of accurate sensing devices. With the harsh loading and climatic conditions that exist on today's roadways, many of the current sensors malfunction.

The Florida Department of Transportation (FDOT) uses piezoelectric sensors for weigh-in-motion (WIM) and traffic classification. These sensors have failed prematurely for a variety of reasons. Reports from field personnel indicate that they corrode, they are destroyed by sharp objects being dragged across them and that power surges affect them. Additionally, their signals can be affected by vehicles in adjacent lanes. FDOT is looking for alternatives to the standard piezoelectric sensors. They would like sensors with a lifetime of 10 years or more to simplify their current traffic sensor maintenance program.

Fiber-optic sensors have important advantages over current techniques. Their small size makes them ideal for *in situ* monitoring, because they are immune to corrosion and electromagnetic interference, they cannot cause fires, and multiple fiber-optic sensors can be placed in series on one optical fiber (i.e., multiplexing) (Kim and Shaw, 1989), (Wolfbeis, 1989). They are flexible, moisture insensitive, reliable and rugged. Another unique advantage is the chemical stability of the plastics and glasses that make up the optical fibers. Fiber sensors used in areas contaminated with hazardous compounds would be immune to chemical breakdown. These advantages, along with the economics of fiber-optic sensors, have led to a significant research effort aimed at developing fiber-optic sensors (Ansari, 1993), (Cosentino, et al., 1994), (Grossman, et al., 1994).

During a 12-month study for FDOT, researchers at Florida Tech proved that relatively inexpensive fiber-optic traffic sensors could be used for traffic classification and WIM applications (Cosentino and Grossman, 1996).

1.2 OBJECTIVE

The objective of this research was to improve on the fiber-optic traffic sensor (FOTS) developed at Florida Tech, by increasing its sensitivity, studying its usefulness in both flexible and rigid pavements and to explore its WIM accuracy.

CHAPTER 2

2.0 TRAFFIC AND FIBER-OPTIC SENSOR LITERATURE

2.1 CURRENT TRAFFIC SENSOR TECHNOLOGIES

There are many types of traffic sensor systems in use today. Typically, combinations of electromagnetic loops and piezoelectric sensors are used in conjunction with data acquisition systems, to determine information such as vehicle weights, axle counts and vehicle speeds. These systems are installed in pavement grooves and secured in place with epoxies. Road tubes, which are placed on the pavement, are commonly used to determine seasonal traffic counts. However, these surface-mounted devices can often be damaged by towed vehicles or sharp objects dragged along the road surface.

Electromagnetic loop detectors are relatively simple and inexpensive systems that include wires placed in rectangular pavement grooves. These sensors are relatively robust, however, they can only be used to detect the presence of a vehicle. Piezoelectric sensors are relatively complicated devices that rely on impact loads to cause a voltage change in a ceramic material manufactured with an electrical charge.

2.2 TRAFFIC CLASSIFICATION

Traffic classification, as defined by the U.S. Department of Transportation in its *Traffic Monitoring Guide,* is "the observation of highway vehicles and the subsequent sorting of the resulting data into a fixed set of categories" (US DOT, 1992). Traffic data is currently grouped into 14 classes, with class 1 to 4 being light vehicles and class 5 and above consisting of buses and trucks. Current vehicle classification systems use a combination of inductive loops, piezoelectric sensors or road tubes, placed together in a single lane connected to a dedicated traffic computer. A common classification configuration is presented in Figure 2.1. FDOT currently has over 6,000 traffic classification sites statewide, plus an additional 28 WIM sites.

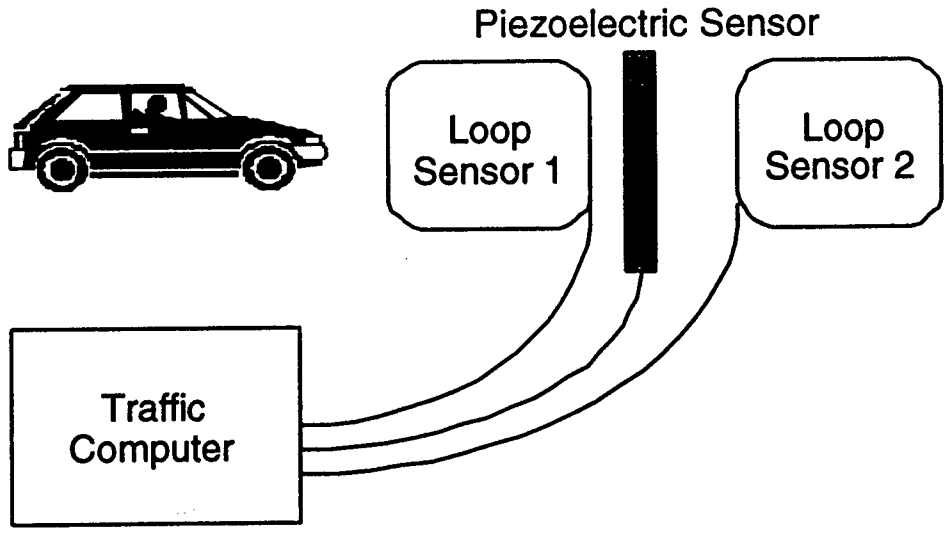

Figure 2.1 Typical Inductive Loop and Piezoelectric Layout for Vehicle Classification

2.3 WIM SYSTEMS

Weigh-in-motion (WIM) scales are defined in the U.S. Department of Transportation's *Traffic Monitoring Guide* as "dynamic weighing systems that determine weights while vehicles are in motion" (US DOT, 1992). The dynamic weight measured by WIM scales should ideally correlate to the static weight of a vehicle. However, measurement of the weight of a vehicle in motion has additional variables that are not present or significant at static weight scales. These factors include wind, pavement roughness, vehicle speed, suspension, etc. Therefore, the American Society for Testing and Materials (ASTM) created the *Standard Specification for Highway Weigh-in-Motion (WIM) Systems with User Requirements and Test Method*, (ASTM E 1318 - 92) to outline specifications on the design of a WIM site and to help control and minimize the factors affecting dynamic weight measurement (ASTM E 1318 - 92).

Types of common WIM sensors include bending plates and piezoelectric strip sensors. The bending plate sensors consist of a large metal plate, the width of the lane by a few feet along the lane, that is level with the surface of the road. When an axle of a vehicle passes on top of the sensor, the forces exerted on the plate are transferred to a load cell or a strain gauge, which in turn is recorded by WIM electronics. The weights of each axle of the vehicle are added together to get the total vehicle weight.

The piezoelectric sensors used in traffic classification and WIM produce an output voltage that is proportional to the force applied to it by a moving tire. In a fiber-optic microbend sensor, the output intensity is also proportional to the force applied to it. Figure 2.2 shows typical waveforms from piezoelectric and fiber-optic microbend sensors. The fiber-optic sensor signal variations can be either a decrease in voltage, as shown in the figure, or increased depending on the opto-electronic interface that is used.

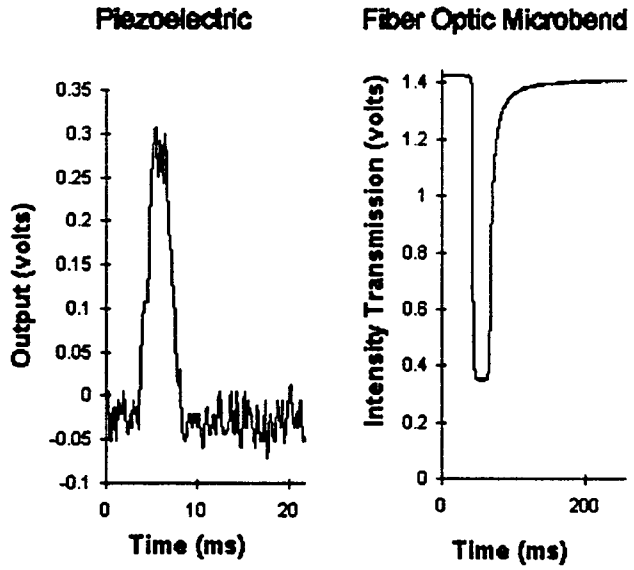

Figure 2.2. Piezoelectric and Fiber-Optic Microbend Output Waveforms

Based on the similarities of signals from both sensors, it was concluded that a fiber-optic microbend sensor could be used as an alternative to piezoelectric sensors for traffic applications. Table 2.1 lists advantages and disadvantages of both piezoelectric and fiber-optic microbend sensors. The fiber-optic microbend sensors have many advantages over the piezoelectric sensors, including corrosion resistance and electromagnetic interference (EMI) immunity. The main disadvantage of the fiber-optic microbend sensor is its newness.

Table 2.1. Advantages and Disadvantages of Piezoelectric and Fiber-Optic Microbend Sensors

	PIEZOELECTRIC	FIBER-OPTIC MICROBEND
Advantages	* Proven technology * Flexible * Installed below pavement	* Flexible * Corrosion resistant * Installed below pavement surface * Immune to lightning and EMI interference * Can be remotely located
Disadvantages	* Some models rigid * Some models installed above pavement surface * Electrical contacts erode * Susceptible to EMI and lightning	* New technology

2.4 FIBER-OPTIC SENSORS

Fiber-optics have revolutionized the communications field over the last 15 years by allowing faster and higher bandwidth connections than previously possible with conventional wire systems. The increased demand for optical fibers has driven down the prices and made optical fibers and their components more widely available. This increase in availability has resulted in an increased development of fiber-optic sensors.

Fiber-optic sensors fall into two broad categories—extrinsic and intrinsic. Both types require a light source, such as a laser, to be focused or coupled into the core region of the fiber. Lasers are fairly high-intensity light sources, while light emitting diodes (LEDs) are fairly inexpensive low-intensity light sources. If possible, it is advantageous to develop sensors that require less light and can function with LEDs.

Extrinsic optical fiber sensors transmit light to a measurement section of the fiber. Here, the light is externally modulated by various types of external effects (i.e., load, displacement, color change, etc.). The light then is returned to a measurement system that gives output readings in voltage and uses laboratory calibrations to predict changes.

Intrinsic means that the light in the optical fiber is internally modulated by environmental effects. Intrinsic fiber-optic sensors can be split into two subclasses—intensity-based modulation and interferometric-based modulation. Interferometric fiber-optic sensors are the most sensitive of all fiber-optic sensors. They operate by using measurements of phase changes induced by environmental effects between one or more of energy levels (termed modes) of light propagating down the fiber. The intensity modulated sensors operate by using measurements of the change in the light intensity propagating down the fiber;

however, they are approximately three orders of magnitude less sensitive than interferometric sensors. Changes in the intensity of light are caused either by scattering or by modal coupling of light out of the core. The latter effect is produced by microbending the fiber in the desired sensing region. The microbend sensor is the type of fiber-optic sensor used in this research. It requires the least expensive light source (i.e., an LED) and therefore, becomes a very economical sensor.

The microbend effect is caused by periodic changes in the geometry of the fiber causing the light guided in the core of the fiber to be coupled out of the core into the cladding (Figure 2.3).

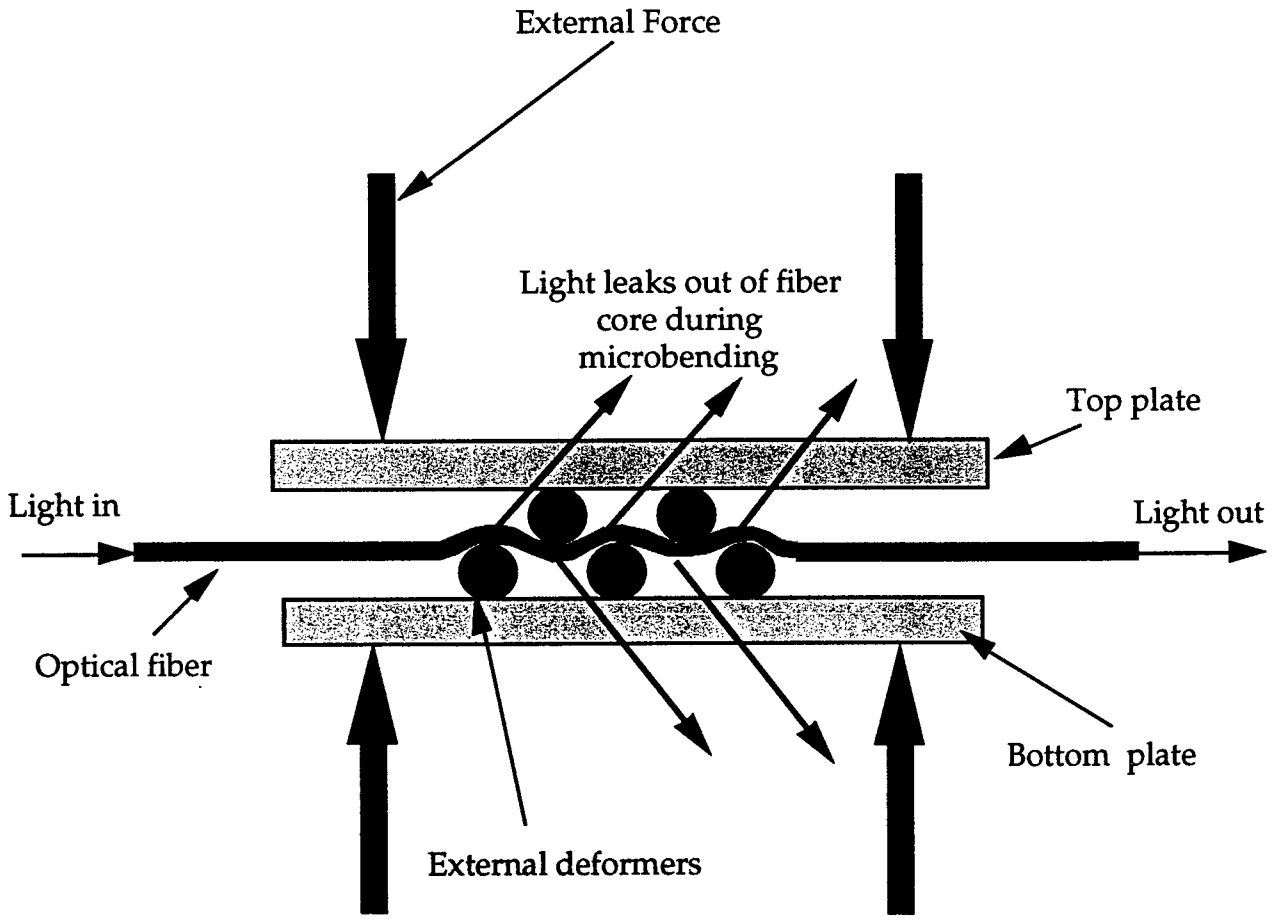

Figure 2.3. Typical Microbend Sensor

In the cladding the light is "weakly" guided and the intensity will couple out into the coating. The microbend sensor is a good sensor because it is easy to build and requires only a few low-cost components for the transmission and detection of the light. The mechanical deformers used to induce the microbend effect can be just about any periodic material, including polymer and metal meshes or sandpaper. To make a sensor, optical fiber is placed between a segment of a periodic structure and connected to optical components. External forces on the periodic structure induce changes in the propagating light intensity that are monitored with a photodetector.

2.5 MICROBEND LOSS THEORY

Microbending losses cause the propagating light intensity to be coupled out of the core. The loss occurs when the guided, higher-order core modes are coupled to the weakly guided cladding modes (radiative modes) in multimode fibers. This mode coupling occurs when the fiber geometry is changed by environmental effects that induce physical periodic bends in the fiber. These small changes in geometry cause low-order core modes to be coupled to the higher-order core modes, and at the same time, the higher-order core modes to radiative modes. To understand the microbend effect, this mode coupling must be examined. This theory is too complex for this report; however, a complete description is included in many fiber-optic texts and was adequately summarized by Taylor, (1996).

The key concepts affecting microbend sensors are the spacing of the deformer(s), the size or length of the sensing region, plus the elastic properties of the fiber and surrounding deformers. The amount of light lost during microbending changes with the spacing of the deformers. There may not be a linear relationship between light loss and sensor contact length (i.e., the amount of light lost over a 4-inch (10.16 cm) length may not be four times the loss over a 1-inch (2.54 cm) length). The elastic response of the fiber and surrounding deformers can affect the sensitivity and useful range of the microbend sensor.

CHAPTER 3

3.0 TESTING PROGRAM

Traffic sensors are subjected to extremely hazardous loading and climatic conditions. Millions of heavy trucks, with tire pressures of 100 psi, (700 kPa) pass over them while temperatures in the pavement vary from below freezing to over 140° F. There are very few standardized tests that can be applied to determine the strength and deformation characteristics of traffic sensors subjected to these conditions. A complete testing program would require analysis of the internal components of the sensor, plus the entire sensing system.

An extensive laboratory testing program was conducted to characterize the various components of the sensor. The stresses in the fiber were analyzed along with the variation in signal that result from loading the microbend sensors. The optical fiber is the weakest component of the sensor. It is weak in shear, and the microbend process applies shear stresses to the fiber. The microbends for the traffic sensors are formed by pressing the fiber against a mesh that is secured between two hard plastic plates (Figure 3.1). There are inherent variations in the meshes used that result in changes of the output light intensity along the length of the sensors.

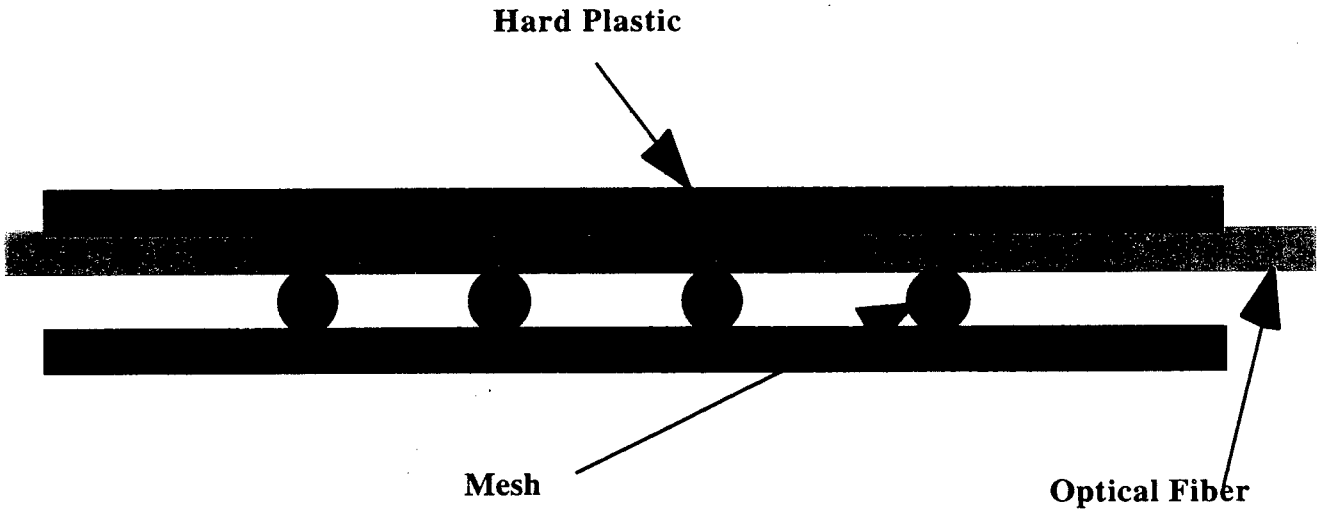

Figure 3.1. Basic Microbend Traffic Sensor Configuration

3.1 FIBER DESCRIPTION

The optical fiber used in this investigation was Corning® 50/125/250 acrylate coated fiber (Figure 3.2). It is a commonly available grade that has been successfully used in other fiber-optic microbend sensor designs (Cosentino and Grossman, 1996). This fiber has a glass core, glass cladding and acrylate coating with an outside diameter of 50 μm, 125 μm and 250 μm, respectively. Within the coating, are two layers of acrylate—an inner and outer layer (Figure 3.2). The outside diameters of the inner and outer layers are190 μm and 250 μm. Inside the FOTS, the fiber is lined along the grid of the mesh that lays within an aluminum channel. The mesh strands support the bottom of the fiber. As a load is applied to the sensor, it

transfers to the fiber and continues perpendicular along the mesh. This loading scenario was used in modeling the magnitude of stress experienced by the fiber in a FOTS.

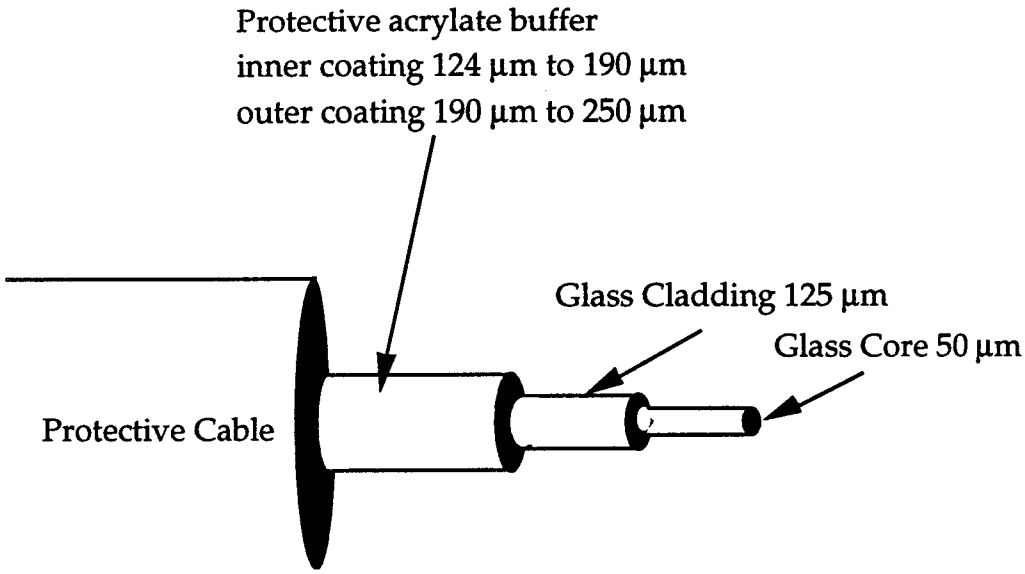

Figure 3.2. Corning® 50/125/250 Acrylate Coated Fiber

3.2 MODELING THE STRESSES IN THE FIBER

Three special considerations were encountered when determining how to model the stresses between the fiber and mesh under crushing loading conditions. All three were a result of the fiber and microbending mesh's small diameter. Typical material tests are conducted on sufficiently large samples to make clear engineering conclusions from load versus deflection data. However, with an outside diameter of 250 μm determining whether ductile or rigid failure occured, or determining if the fiber was subjected to shear, tensile or torsional stresses was very difficult.

First, the size of both the fiber and mesh were so small that visually confirming the type of failure was very difficult, (i.e., whether it was shear, flexural, compressive, or tensile). A scanning electron microscope photo of an optical fiber fractured from contact with microbending metal teeth revealed only a crack in the fiber coating, which was not enough evidence to state that a ductile or brittle failure occurred (Figure 3.3).

Second, when trying to model the stress transfer throughout the fiber, the portion of stress going through both the acrylate and the glass versus just through the acrylate is unknown. When modeling fiber failure, it was assumed that the entire stress transferred through the center of the fiber, through the acrylate, glass, then acrylate again (Figure 3.4). This assumption was believed to be conservative because it resulted in the highest stress being applied to the glass core.

Third, the elastic properties, namely Young's modulus, of the fiber can vary depending on the coating material and diameter (Figure 3.2). Knowing the percentage of the acrylate and glass contained in the fiber, a composite modulus was estimated based on the rule of mixtures (Askeland, 1994). The rule of

mixtures can be applied when fibers are unidirectional and uniform. Because the layers within the fiber were also unidirectional and uniform, a composite modulus was calculated by adding the volume of each layer per modulus of that layer. The complete explanation of this process is described in Section 3.3.1

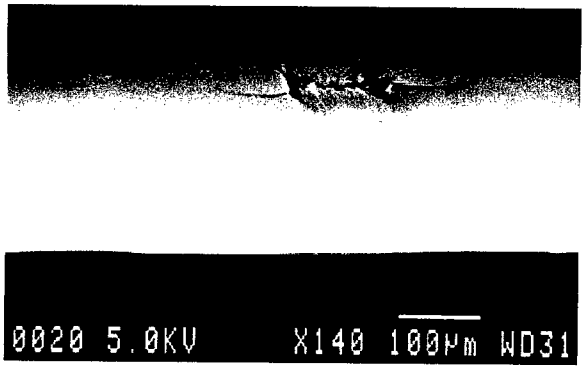

Figure 3.3. Crack in Fiber Taken with Scanning Electron Microscope

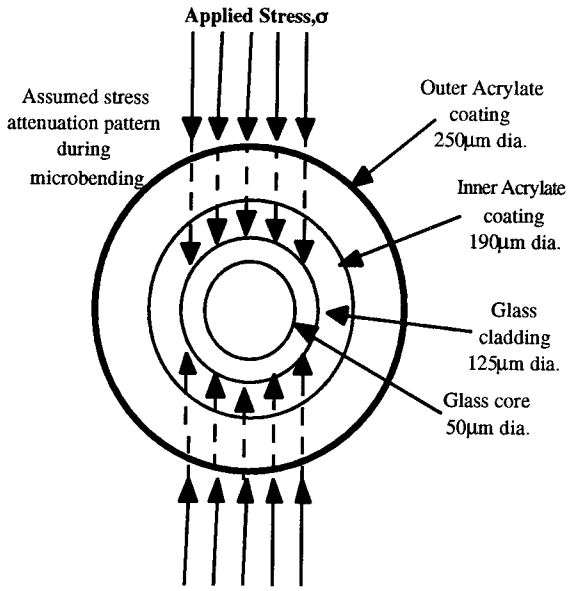

Figure 3.4. Assumed Stress Attenuation Through 50/125/250 Optical Fiber During Microbending

3.2.1 Comparative Fiber Stresses

In developing a laboratory testing program, guidelines or criteria need to be established beforehand to help determine the validity of tests or accurateness of predictions. In this case, predicting the maximum stress in a fiber at failure was the goal. To determine if the calculated stress from analytical models was reasonable, handbook values for the strength of glass, strength of optical fibers reported by Corning, and strengths of optical fibers reported by Biswas (1991) were found.

An average strength for manufactured fibers is reported to be in the range of 700,000 psi (4.9×10^6 kPa); however, the mean strength of high-quality optical fibers can be as high as 2×10^6 psi (14×10^6 kPa) (Biswas, 1991). This range in strength is a function of surface flaws and internal defects, fibers with no flaws or defects have the upper values of reported strengths (Biswas, 1991). At Corning's plant, all

fibers manufactured are subjected to a proof test that exposes the fibers to a minimum tensile stress of 50,000 psi ($3.5x10^5$ kPa) along the length of the fiber before distribution (Corning, 1988). The two optical fibers used in this investigation (i.e., the 50/125/250 and 62.5/125/250 acrylate coating fibers) were proof tested at a higher stress, 100,000 psi ($7x10^5$ kPa) (Corning, 1988). Proof testing guarantees that the tensile strength of the fiber is greater than 100,000 psi ($7x10^5$ kPa).

Because the most fragile component of the fiber was assumed to be the glass, the strength properties of glass were also used as comparison values when determining the use of the analytical model (Table 3.1). Glass rods can have a tensile strength of between 40,000 psi ($2.8x10^5$ kPa) and 115,000 psi ($7.9x10^5$ kPa), depending on the diameter size, the larger the diameter the weaker the tensile strength (Tooley, 1953). The reported compressive strength of glass was 290,000 psi ($2.0x10^6$ kPa) (Tooley, 1953) and the reported flexural strength was 9,000 psi ($6.2x10^4$ kPa) (Askeland, 1994).

Table 3.1. Summary of Reported Fiber and Glass Strengths

Handbook values for the strengths of bulk glass[1]			"Tensile" Proof Test[2]	Reported average strength for manufactured fibers[3]	Reported mean strength of optical fibers[4]
Flexural	Tensile	Compressive			
(psi)	(psi)	(psi)	(psi)	(psi)	(psi)
9,000	40,000–115,000	290,000	100,000	700,000	2,000,000

[1] From Tooley, 1953
[2] From Corning, 1988
[3] From Biswas, 1991
Note: 1 psi = 7 kPa (soft conversion)

3.2.2 Analytical Fiber Stress Models

Three existing mathematical models were originally examined to predict the magnitude of stresses experienced by the fiber in a FOTS—beam analysis, indirect tensile analysis, and contact stress analysis.

When evaluating the use of the beam equations, assumptions for deflection and fiber modulus of elasticity were necessary. The amount of deflection, if any, is uncertain due to the small size of the fiber and mesh. Also, as a load is applied to the sensor, the fiber is assumed to be deforming at the point of contact with the mesh, rather than deflecting between the mesh strands (Figure 3.5). Therefore, the bending stresses predicted from the beam models were discarded.

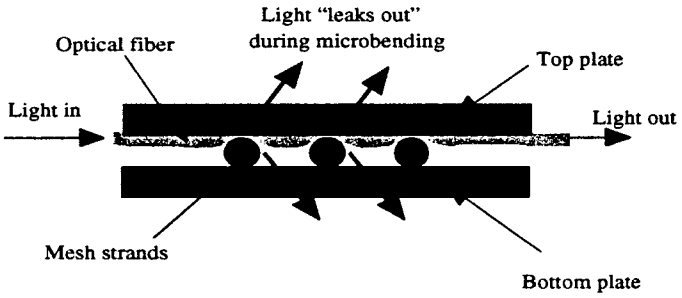

Figure 3.5. Assumed Deformation Pattern for Fiber-Optic Traffic Sensor Configuration

Optical fibers' tensile strengths were examined. Characterization of fiber failure based on the indirect tensile test was used to perform a second microbending stress analysis. The indirect tensile test involved loading a cylindrical specimen with a compressive load. These tests are typically run on concrete, a brittle material that fails suddenly. The manner in which the specimen is loaded results in a relatively uniform tensile stress acting perpendicular to and along the diametrical plane of the applied load (Figure 3.6). This loading results in a splitting failure generally along the diametrical plane and results in a maximum tensile stress of

$$\sigma_c = \frac{15P}{\pi td} \qquad (3.1)$$

where

P = total applied load
t = specimen thickness (mesh diameter)
d = specimen diameter (fiber diameter)

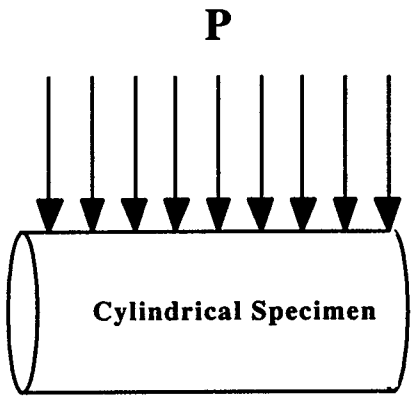

Figure 3.6. Load Applied to Cylindrical Specimen During Indirect Tensile Test (Yoder, 1975)

In examining the microbend effect on the fiber against the mesh, the direction of the applied load onto the fiber in a FOTS is similar to the loading of a specimen during the indirect tensile test (Figure 3.6). However, a flat platen is placed below the cylindrical specimen, rather than another cylindrical specimen, such as the test between the fiber and mesh. The fiber and mesh were assumed to act as two cylindrical specimens perpendicular to each other. The boundary conditions for the indirect tensile analysis were not representative of those between the fiber and mesh; therefore, the analysis was not expected to be used for further investigation.

The third analysis performed was based on equations for stresses between two perpendicular cylindrical bodies, which is the scenario between the fiber and mesh in a FOTS (Figure 3.7). The equations were based on Hertz's theory for the surface stresses and deformations produced by pressures between cylindrical bodies (Roark, 1943). When a specimen is under pressure, there is a maximum compressive stress that occurs at the center of the surfaces of contact (Roark, 1943). In 1895, Hertz developed an equation

to predict the maximum compressive stress between two perpendicular cylinders.
The expression for the maximum compressive stress due to pressure on these bodies was given as

$$\sigma_c = \frac{15P}{\pi td} \qquad (3.2)$$

where

P = load per unit length
c, d = major and minor semiaxis of elliptical contact area

The expressions for c and d were given as

$$c = \alpha \sqrt[3]{P \frac{D_1 D_2}{D_1 + D_2} \left[\frac{1-\nu_1^2}{E_1} + \frac{1-\nu_2^2}{E_2} \right]} \qquad (3.3)$$

$$d = c\beta \qquad (3.4)$$

where

α and β = Constants that depend upon D_1/D_2
D_1 and D_2 = Mesh and fiber diameter, respectively
n_1 and n_2 = Poisson's ratio for the mesh and fiber, respectively
E_1 and E_2 = Young's modulus for the mesh and fiber, respectively

Hertz provided a table with values for α and β. When D_1/D_2 was between 1 and 10, α would range between 0.908 and 2.175 and β would range between 1 and 0.221 (Roark, 1943).

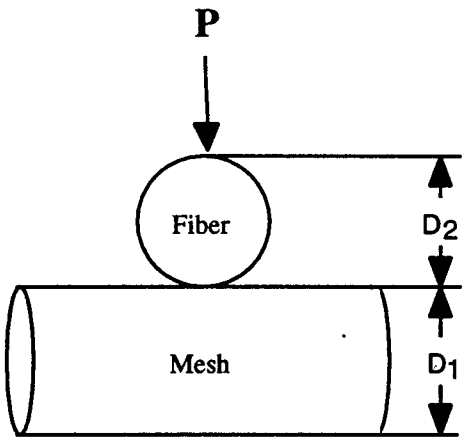

Figure 3.7. Representation of Fiber/Mesh Contact Using Two Perpendicular Cylinders (After Roark, 1943)

3.3 ANALYSIS OF STRESSES IN A FIBER-OPTIC TRAFFIC SENSOR

3.3.1 Properties of the Fiber Components

To make acurate stress predictions, based on Hertz's theory, the elastic moduli and Poisson's ratio for Corning fiber were defined. Poisson's ratio for acrylate coating fibers is not reported in handbooks because the acrylate is a proprietary product of Corning (Kerbein, 1997). Typically, Poisson's ratio ranges between 0.15 and 0.5 for all materials; and for plastics, the ratio is 0.33 (Askeland, 1994). This relatively small range results in little sensitivity in terms of stress and strain. An assumption was also made that the glass was the critical material in the fiber because once it failed, the fiber and therefore the sensor, failed. The reported Poisson's ratio for glass was 0.14 (Tooley, 1953). These two ratios were used as variables in the stress predictions.

Another property that had to be defined was the modulus of elasticity of the fiber. This elastic property varies due to the layers of acrylate and glass within the fiber. The modulus of elasticity for the fiber was not reported by the manufacturers, therefore, it was calculated based on three cases. The first case was based on the assumption that the glass was the most critical element of the fiber, and therefore, the modulus of elasticity for glass, 1.05×10^7 psi (7.35×10^7 kPa), was used in the equation (3.5) (Tooley, 1953).

The second and third cases required an estimate of the composite modulus of elasticity. Assuming the rule of mixtures applies and that the fibers components are continuous and unidirectional, a composite modulus of elasticity was estimated (Askeland, 1994) using the following equation:

$$\frac{1}{E_c} = \frac{f_g}{E_g} + \frac{f_a}{E_a} \qquad (3.5)$$

where

E_c = composite modulus of elasticity
E_g = modulus of elasticity for glass
E_a = modulus of elasticity for acrylate
f_g = volume fraction of glass
f_a = volume fraction of acrylate

Corning® 50/125/250 acrylate coated fiber consists of 75% acrylate and 25% glass. The acrylate coating consists of an inner and outer layer (Figure 3.8). The modulus of elasticity of the inner and outer layer are 246 psi (1750 kPa) and 84,100 psi (5.9×10^5 kPa), respectively (Kerbein, 1997).

For the second case only the modulus of the outer layer of acrylate was considered due to the large difference in moduli between the inner and outer layer. Because the outer moduli was much larger, it was assumed that the inner layer did not contribute significantly to the elastic resistance of the fiber. The inner acrylate layer was assumed to act as an energy absorption barrier around the glass. This

assumption led to a composite modulus of elasticity of 112,000 psi ($7.8x10^5$ kPa). For the third approach, the entire acrylate coating was considered, taking into account both the inner and outer layer.

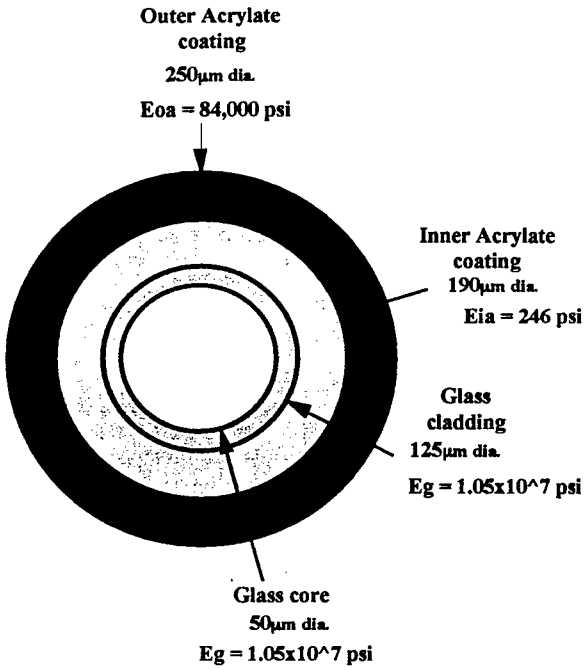

Figure 3.8. Corning® 50/125/250 Fiber Elastic Properties

It was assumed that a third ratio could be added to equation (3.5) to include the effect of the inner acrylate layer. The resulting composite modulus of elasticity under this approach was 1,020 psi ($7.1x10^3$ kPa).

3.3.2 Model Predictions

A sensitivity analysis was performed using Hertz's equation for the compressive stress between the fiber and the mesh. Four cases were developed assuming various combinations of composite moduli and critical fiber diameter (Table 3.2). Stress calculations using these four cases were performed based on the assumption that a 100 psi (700 kPa) truck tire, 16-inch (45 cm) wide, passes over a one-half inch wide sensor resulting in an applied load of 800 lbs (363 kgs) (Table 3.3). These tire pressures and dimensions are common for large asphalt- or concrete-mix trucks.

Table 3.3 shows the anticipated compressive stresses from the four cases. The mesh used in these calculations was a 10 mil (0.25 mm) diameter nylon mesh. Its modulus of elasticity was 400,000 psi ($2.8x10^6$ kPa) and Poisson's ratio was 0.48 (Beer and Johnston, 1992). This mesh type was chosen due to the ease in finding the material properties of nylon and it was considered a readily available mesh. It has been successfully used in some traffic sensors. The variables of the four cases were summarized in Table 3.2.

Table 3.2. Summary of Variables Used in Stress Calculations for Four Cases

	Fiber Diameter D_2 (in)	Composite Modulus of Elasticity for the fiber E_2 (psi)	Poisson's Ratio for the fiber υ_2
Case 1	0.01	10,500,000	0.14
Case 2	0.005	10,500,000	0.14
Case 3	0.01	112,000	0.14
Case 4	0.01	1,020	0.14

Note: 1 psi = 7 kPa (soft conversion)

Case 1: Assumed only glass resists load but glass modulus used over the entire fiber diameter.

Case 2: Assumed only glass resists load and glass modulus used only with glass diameter.

Case 3: Assumed the composite modulus was from the outer acrylate layer and the glass resists load, while the entire fiber diameter used for calculations.

Case 4: Assumed the composite modulus was from the outer and inner acrylate layer and the glass, the entire fiber diameter and Poisson's ratio for glass.

Table 3.3. Estimated Compressive Stresses Between 50/125/250 Acrylate Coated Fiber and Nylon Mesh

	Diameter		Modulus of Elasticity		Poisson's Ratio		Applied Load[1]	Predicted Compressive Stress[2]
	Mesh D_1 (in)	Fiber D_2 (in)	Mesh E_1 as reported (psi)	Fiber E_2 as calculated (psi)	Mesh υ_1	Fiber υ_2	P (lbs)	σ_c (psi)
Case 1	0.01	0.01	400,000	10,500,000	0.48	0.14	800	1,269,000
Case 2	0.01	0.005	400,000	10,500,000	0.48	0.14	800	1,268,000
Case 3	0.01	0.01	400,000	112,000	0.48	0.14	800	418,000
Case 4	0.01	0.01	400,000	1,020	0.48	0.14	800	20,800

[1] Assuming 16" wide 100 psi truck tire over a 0.5" sensor

[2] Calculated form Hertz, 1895: $\sigma_c = \frac{15P}{\pi cd}$

Note: 1 psi = 7 kPa (soft conversion)
1 in = 2.54 cm
1 lb = 0.4541 kgs

Hertz's compressive stresses were determined for each of the four cases. The results, shown in Table 3.3 were compared as follows.

Case 1 and Case 2: In these cases, only the fiber diameter changed from 0.01 in. (0.025 cm) to 0.005 in. (0.013 cm), a factor of 50% that correlated to a very small decrease in area. According to Table 3.3, the decrease in diameter caused a change of only 1,000 psi ($7x10^3$ kPa) in stress. Both cases predicted a stress the same order of magnitude as the mean strength of high quality fibers ($2x10^6$ psi $1.4x10^7$ kPa)). The sensor should be designed with a factor of safety on the ultimate strength to ensure durability. If in the field the stresses are $1.3x10^3$ psi ($8.9x10^3$ kPa), as anticipated, then careful measures should be taken to install the sensor deep enough to prevent these stresses from reaching the sensor.

Case 1, Case 3 and Case 4: In these cases only the modulus of elasticity of the fiber changed from $1.05x10^6$ psi to $0.11x10^6$ psi to $1x10^3$ psi ($7.3x10^6$ kPa to $7.7x10^5$ kPa to $7x10^3$ kPa). According to Table 3.3, the decrease in moduli caused a significant decrease in stress, $1.3x10^6$ psi to $0.42x10^6$ psi to $0.2x10^5$ psi ($9.1x10^6$ kPa to $2.9x10^6$ kPa to $1.4x10^5$ kPa). With these cases, it was concluded that stress was largely dependent upon the modulus of elasticity of the mesh. Understanding the relationship between the modulus of elasticity of the mesh and the failure load can aid in the FOTS design process.

Case 3 and Case 4: In these cases only the modulus of elasticity of the fiber changed from 112,000 psi to 1,020 psi ($7.8x10^5$ kPa to $7.1x10^3$ kPa), almost a 99% decrease. According to Table 3.3, this decrease in moduli also caused a decrease in stress of about 95%, 418,000 psi to 20,800 psi ($2.9x10^6$ kPa to $1.4x10^5$ kPa). Again, stress was proven to be greatly influenced by the modulus of elasticity of the mesh. The stress from Case 3 was close to the compressive strength of glass, 290,000 psi ($2.0x10^6$ kPa). Case 4, 18,000 psi ($1.2x10^5$ kPa) compared with the flexural strength of glass, 9,000 psi ($6.3x10^4$ kPa). Because Hertz's theory predicted a compressive stress, the assumptions used in Case 4 were not expected to be correct, but Case 3 seems probable.

3.3.3 Laboratory Testing Program for Determining Fiber Stresses

The contact stresses between rubber from a tire and pavement surface are very complex. Multilayered pavement, finite element models have been developed for this problem (Yoder, 1975). When a tire contacts a smooth pavement surface, a contact area less than the entire footprint will occur, making it difficult to determine the actual contact stress. Static stresses for truck tires average around 100 psi (700 kPa); however, stress concentrations can cause much higher values (Yoder, 1975). In the process of designing a reliable and sturdy sensor to withstand heavy vehicle conditions without breaking, the ultimate failure load has become an important parameter to consider.

3.3.4 OTDR Failure Test

To determine the ultimate failure load of an optical fiber over a given mesh type, a test named the OTDR failure test was developed. An optical time domain reflectometer (OTDR) was used to monitor fiber failure during static loading conditions. The test required 10 minutes to complete.

An OTDR is considered one of the most sophisticated instrument systems available for testing fiber-optic cable and detecting a break in the fiber (Laser Precision Corporation, 1991). It projects a laser pulse through the fiber and measures the amount of backscattered light it receives. The reflections are then collected and produce a "scan" of the fiber. There are two parts to a scan—continuous and spiked. The continuous component represents the backscattered light through the fiber and the spikes can indicate a connection, a mechanical splice or a break in the fiber. Using the horizontal scale on the OTDR, the connection, splice or break can be distinguished depending on the location of the spike.

3.3.5 OTDR Test Procedure

One fiber, the Corning® 50/125/250 acrylate coating, and five mesh types (1 polyester, nylon and Tefzel®, and 2 polypropylenes) were selected for testing. Twenty trials of each combination of fiber and mesh were conducted to obtain an average fracture load and to determine if repeatable results could be obtained. Details of the testing procedure are given in Appendix A.

3.3.6 Experimental Results

After each test was conducted, the fiber and mesh were examined to evaluate any deformation that may have occurred. In all samples, the fiber was broken in two pieces and the mesh was deformed at the point of contact with the fiber. This was an indication that not only the fiber but also the mesh were taking a certain degree of stress.

The results of the OTDR failure test are summarized in Table 3.4. Twenty samples of each combination were tested. The average, median, and standard deviation of the failure loads were determined for each set of data. Histograms were also developed to visualize any trends that may have existed (Appendix B). The average failure load for a polyester mesh, 50/125/250 fiber combination was experimentally found to be 102 lbs (46 kgs) with a standard deviation or failure range of 114 lbs (52 kgs). Forty-five percent of the samples failed within the first 100 lbs (45 kgs) nine of which failed under 30 lbs (14 kgs). The large variance made a definite conclusion difficult. The test procedure was carefully reviewed; however, no problems were found. Therefore, further analysis was performed.

Analysis of the raw test results indicated two trends. First, failure load was a function of mesh material and the second, the failure load was not a function of mesh diameter. The average failure load was highest for the Tefzel® mesh, 499 lbs (226 kgs), and lowest for the polyester mesh, 102 lbs, (46 kgs) with a difference of almost 400 lbs (181 kgs) between the two indicating that the fracture load was a function of mesh material.

The average fracture loads for both polypropylene mesh strands, 10 and 20 mils (0.025 cm, 0.05 cm) in diameter, were close to 300 lbs (136 kgs). This gave an indication that the fracture load was not a function of mesh diameter. From all the combinations, however, a wide range of failure loads were recorded and standard deviations larger or close to half the failure loads were calculated.

Table 3.4. Summary of OTDR Failure Testing on Corning 50/125/250 Fiber

Mesh Diameter	Polyester 20 mil (lbs)	Polypropylene 20 mil (lbs)	Polypropylene 10 mil (lbs)	Nylon 10 mil (lbs)	Tefzel® 10 mil (lbs)
Average	102	295	304	334	499
Median	59	284	243	332	459
Std. Dev.	114	140	173	151	244

Failure Loads, P (lbs)

Note: 1 lb = 0.4541 kgs

The validity of the test was questionable due to the large variation in results. Variability could be a function of mesh being woven and the corresponding contact area is not controlled, because the meshes do not cross perpendicular to each other. Also, the deformations could cause irregularities in the mesh. Variability may also be inherent in the mesh. Its design purpose is not for use in fiber-optic sensors. These materials are typically used for filtration purposes such as ropes, garment and industrial applications, and tire fabric (Lumite, 1996).

3.3.7 Modified OTDR Failure Test With Straight Strands

To determine if the deformities in the mesh may have contributed to the randomness of the failure loads straight strands of a high-quality 20 mil (0.05 cm) diameter nylon fishing line and steel wire were used in replace of the woven mesh strands. Ten samples were tested using the same procedure and the failure loads for each were recorded.

Table 3.5. Results of OTDR Failure Test Using Nylon Fishing Line and Steel Wire

	Nylon fishing line 10 mil dia. (lbs)	Steel wire 20 mil dia. (lbs)
Average	458	1.6
Median	455	1.5
Std. Dev.	11	0.2

Note: 1 mil = 2.54×10^{-3} cm
1 lb = 0.4541 kgs

For the fishing line, an average failure load of 458 lbs (208 kgs) was found with a standard deviation of 11 lbs (5 kgs) (Table 3.5). Deformation of the nylon fishing line was apparent after testing, which indicated that the nylon absorbed a portion of stress during loading. The average failure load recorded for the steel wire was 1.6 lbs (0.7 kgs) with a standard deviation of 0.2 lbs (0.09 kgs) (Table 3.5). No damage to the steel was apparent after each test, which was in contrast to the nylon, polyester, polypropylene, and Tefzel® meshes. Therefore, it was concluded that the fiber was taking all the stress.

Based on the reasonably small standard deviations from these two sets of OTDR failure tests, it was assumed that the imperfections in the woven mesh strands were the cause of the large variation. The failure loads based on the fishing line and steel wire results were then used to estimate failure stresses. Using the same four cases presented earlier, new calculations were made based on actual failure loads. The results are presented in Tables 3.6 and 3.7.

Table 3.6. Experimental Failure Stresses For 50/125/250 Acrylate Coated Fiber with Nylon Fishing Line

	Diameter		Modulus of Elasticity		Poisson's Ratio		Failure	Calculated
	Mesh	Fiber	Mesh	Fiber	Mesh	Fiber	Load[1]	Failure
	D_1	D_2	E_1	E_2	u_1	u_2	P	Stress[2]
			as reported	as calculated				σ_c
	(in)	(in)	(psi)	(psi)			(lbs)	(psi)
Case 1	0.01	0.01	400,000	10,500,000	0.48	0.14	458	1,054,000
Case 2	0.01	0.005	400,000	10,500,000	0.48	0.14	458	1,053,000
Case 3	0.01	0.01	400,000	112,000	0.48	0.14	458	17,200
Case 4	0.01	0.01	400,000	1,020	0.48	0.14	458	18,400

[1] Failure Loads from OTDR failure test

[2] Calculated form Hertz, 1895: $\sigma_c = \frac{15P}{\pi cd}$

Note: 1 psi = 7 kPa (soft conversion)
1 in = 2.54 cm
1 lb = 0.4541 kgs

Table 3.7. Experimental Failure Stresses for 50/125/250 Acrylate Coated Fiber with a Steel Wire

	Diameter		Modulus of Elasticity		Poisson's Ratio		Failure	Calculated
	Mesh	Fiber	Mesh	Fiber	Mesh	Fiber	Load[1]	Failure
	D_1	D_2	E_1	E_2	u_1	u_2	P	Stress[2]
			as reported	as calculated				σ_c
	(in)	(in)	(psi)	(psi)			(lbs)	(psi)
Case 1	0.02	0.01	29,000,000	10,500,000	0.28	0.14	1.6	775,000
Case 2	0.02	0.005	29,000,000	10,500,000	0.28	0.14	1.6	780,000
Case 3	0.02	0.01	29,000,000	112,000	0.28	0.14	1.6	45,500
Case 4	0.02	0.01	29,000,000	1,020	0.28	0.14	1.6	2,000

[1] Failure Loads from OTDR failure test

[2] Calculated form Hertz, 1895: $\sigma_c = \frac{15P}{\pi cd}$

Note: 1 psi = 7 kPa (soft conversion)
1 in = 2.54 cm
1 lb = 0.4541 kgs

Nylon Fishing Line: The same trends found previously, under the assumed 100 psi (700 kPa) truck tire loading condition, were found again using the experimental fishing line/fiber failure load. Comparing the stress predictions to the handbook values, the following observations were made.

Case 1 ($1x10^6$ psi, $7x10^6$ kPa) and Case 2 ($0.7x10^6$ psi, $4.9x10^6$ kPa) were above but in the same range as the average strength, $0.7x10^6$ psi ($4.9x10^6$ kPa), of an optical fiber. Case 1 and 2 are larger than the flexural, tensile, and compressive strength properties of glass and appear to predict a strength of the optical. Based on the type of loading condition applied to the specimen it seem likely that these strengths are crushing strengths of the fiber.

Case 3 (347,000 psi, $2.4x10^6$ kPa)) was close to the compressive strength of glass, 290,000 psi ($2.0x10^6$ kPa). This calculation involved a composite modulus of elasticity using the moduli of glass and outer layer of acrylate and the entire fiber diameter. This assumption may be reasonable for predicting the compressive strength of the fiber over a mesh.

Case 4 (17,200 psi, $1.2x10^5$ kPa)) was close to the flexural strength of glass, 9,000 psi ($6.3x10^4$ kPa). A composite modulus including the glass and both acrylate layers, the entire fiber diameter, and a Poisson's ratio for glass was used in this case. The predicted stress for Case 4 was close to the flexural strength of glass and lower than expected because the fibers were proof tested to 100,000 psi ($7.0x10^5$ kPa). The OTDR test was not designed to simulate bending and the calculations were based on a different phenomenon; therefore, these assumptions were not assumed to be realistic.

Summarizing these cases, the estimated stress values were not less than the flexural strength of glass, 9,000 psi ($6.3x10^4$ kPa), and not greater than the mean strength of optical fibers, $2x10^6$ psi ($1.4x10^7$ kPa) was found. The exact stress value can depend on several variables, especially the modulus of elasticity and the corresponding failure load. Because the equation developed by Hertz predicts a maximum compressive stress at the center of the contact surfaces, the variables used in Case 3 appear to yield the best comparisons with the maximum compressive fiber strength in the glass. Therefore, when estimating the maximum compressive strength, both the modulus of elasticity of the outer acrylate layer and glass need to be taken into consideration along with the entire fiber diameter according to Case 3.

Steel wire: A material properties list reports the modulus of elasticity of a steel wire as $29x10^6$ psi ($2.0x10^8$ kPa) and a Poisson's ratio of 0.28 (Gere, 1990). The stress calculations using the results of the OTDR failure test for this steel wire and 50/125/250 Corning® fiber are presented in Table 3.7. Although the stress estimations are significantly lower than those using a nylon strand, similar trends were found.

Case 1 (775,000 psi, $5.4x10^6$ kPa) and 2 (780,000 psi, $5.4x10^6$ kPa) predicted stresses close to those reported for a typical optical fiber (700,000 psi, $4.9x10^6$ kPa). Case 4 (2,000 psi, $1.4x10^4$ kPa) was less than the flexural strength of glass (9,000 psi, $6.3x10^4$ kPa) and too low to consider. For Case 3 (45,000 psi, $3.1x10^5$ kPa), because the mesh used was so rigid, a higher stress concentration on the fiber may have caused a lower failure stress. From the nylon mesh, the assumptions for Case 3 resulted in a strength close to the compressive strength of glass, but when used with steel, the model predicted a stress less than the proof test of 100,000 psi ($7.0x10^5$ kPa). From this, the assumptions appear inapplicable and may only be suitable for mesh types with a low Young's modulus.

Disregarding the variance in the polyester, polypropylene, and Tefzel® mesh types, when the failure loads and modulus of elasticity's of those materials were used along with the Case 3 assumptions, all the resulting stress predictions came within 150,000 psi ($1.0x10^6$ kPa) and 300,000 psi ($2.1x10^6$ kPa). Therefore, for the polyester, polypropylene, nylon, and Tefzel® materials, Case 3 predicted stress values close to the compressive strength of glass.

3.3.8 Correlation Between Failure Loads

Comparing the average failure loads to the modulus of elasticity's of each mesh type; polyester, polypropylene, nylon, and Tefzel® and then adding the results of the fishing line and steel wire. A graph was generated relating failure load to elastic modulus (Figure 3.9).

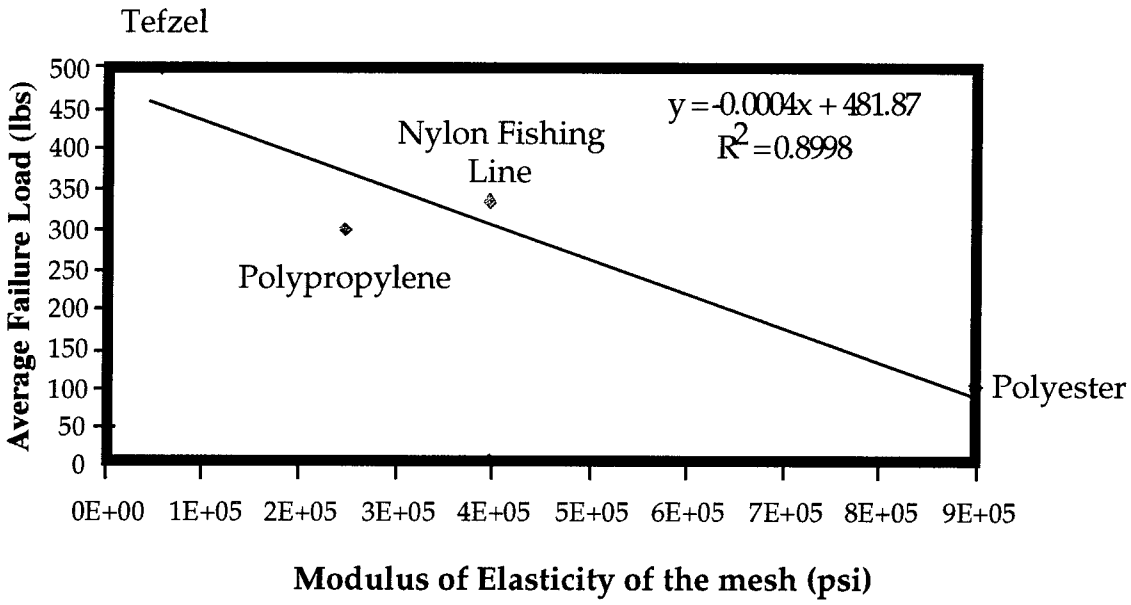

Figure 3.9. Correlation Between Average Failure Load and Modulus of Elasticity of Four Meshes (1 lb = 0.4541 kgs, 1 psi = 7 kPa)

According to Figure 3.9, a general trend was found; as the modulus of elasticity increased, the failure load decreased. The polypropylene, however, had a lower modulus than nylon, which should have resulted in a higher failure load. This inconsistency may have been due to the corrugation of the mesh strand. To establish a better relationship, more tests should be performed with perfect mesh strands of different elasticitys.

3.3.9 OTDR Failure Test Conclusion

The OTDR failure test provided a method of detecting the failure load of various fiber/mesh combinations. Consistent and meaningful results when using perfect mesh strands, like the nylon fishing line and steel wire, were found although the results of the woven mesh strands may also have provided meaningful results when comparing the variance of each mesh type. Because the variance was controlled for both the nylon fishing line and steel wire, it may be an indication that they were subjected to better standards during fabrication versus the woven mesh strands. Even though the variability was large for the polyester, polypropylene, nylon and Tefzel® woven strands, a perfect mesh strand may not be necessary to make meaningful conclusions. Testing the woven strands may provide information on the level of quality control used in the manufacturing process of the mesh and testing perfect strands may provide information necessary to obtain good fiber/mesh combinations and correlations.

3.4 MICROBEND PERIODICITY TESTING

A microbend sensor consists of a mechanical deformer, an optical fiber, a light source and detector circuits. The spatial wavelength or period of the deformers directly effects intensity change in a fiber. A highly sensitive microbend sensor would have the greatest change in optical light intensity with the smallest change in load and deflection. Experiments were required to find the best combinations of deformers and fibers for a microbend sensor. The two main experiments discussed in this section are the measurement of the optimum spatial wavelength for several optical fibers and the comparison of the types of microbend inducing mechanisms. From these two experiments, the microbend sensor design began.

3.4.1 Optimization of Deformer Periodicity

To design a fibe-optic microbend sensor, the relationship between intensity loss and deformer periodicity for the optical fiber must be known. This relationship allows the optimum periodicity or the deformer period at which the greatest intensity loss occurs to be determined. Then intensity versus load curves (or fiber sensitivity) can be measured and used to determine sensor response to external load. To study the periodicity, an experimental microbending mechanism was designed to allow the measurement of intensity versus microbend period for a fiber over a wide range of periods. A batch of optical fibers was chosen and the optimum periodicity for each was measured and compared to the theoretical optimum period. Then, the sensitivity was measured to develop an understanding of each fibers microbend response.

3.4.2 Theoretical Periodicity Calculations

Ten different optical fibers with a variety of core/cladding sizes and coating types were chosen for periodicity measurement. Four of the ten were graded index fibers, while the remaining were step index. Also, to observe if an additional coating would affect the fiber periodicity, one of the graded index fibers was coated in the laboratory with an additional layer of black automobile paint, making a total of 11 samples. Table 3.8 shows pertinent information on the complete set of 11 fibers.

Table 3.8. Manufacturers Information on the Optical Fibers for the Periodicity Test

Specimen			Core	Cladding	Buffer 1	Buffer 2	Coating			
#	Fiber	NA	(um)	(um)	(um)	(um)	Material	Index	Manufacturer	Product Code
1	Corning	0.2	50	125	250	*	Acrylate	GI	Corning	Corning 50/125
2	Corning	0.2	50	125	250	Blk Paint	Acrylate	GI	Corning	Corning 50/125
3	Corning	0.275	62.5	125	250	*	Acrylate	GI	Corning	Corning 62.5/125
4	AGI	0.2	50	125	145	*	Polyimide	GI	Fiberguide	**
5	AGI	0.2	50	125	155	*	Gold	GI	Fiberguide	**
6	APC	0.4	100	200	270	*	Nylon	SI	Fiberguide	APC100N
7	SFS	0.22	105	125	145	*	Polyimide	SI	Fiberguide	SFS105/125T
8	SFS	0.22	200	220	320	480	TEFZEL	SI	Fiberguide	SFS200/220Z
9	SFS	0.22	200	240	**	*	Black TEFZEL	SI	Fiberguide	**
10	SFS	0.22	200	240	265	*	Polyimide	SI	Fiberguide	SFS200/240T
11	SFS	0.22	200	240	310	*	Aluminum	SI	Fiberguide	SFS200/240A

Where GI = graded-index, SI = step-index, NA = numerical aperture, um = micrometers, Blk = Black
* = not present, and ** = information not available

Each of the fibers in Table 3.8 has an optimum periodicity based on its core and cladding diameters, numerical aperture, and index type. Calculation of the theoretical optimum for graded and step index fibers can be achieved with Equations (3.6) and (3.7).

$$\Lambda_{SI} = \frac{\sqrt{2}\pi a n_0}{NA} \qquad (3.6)$$

$$\Lambda_{GI} = \frac{2\pi a n_0}{NA} \qquad (3.7)$$

where Λ_{GI} is the fundamental optimum period for graded-index fibers, L_{SI} is the fundamental optimum period for step-index fibers, a is the diameter of the fiber core, n_0 is the index of refraction at the center of the core, and NA is the numerical aperture of the fiber. Using these equations, the optimum periodicity (spatial wavelength) for each of the optical fibers was calculated and is shown in Table 3.9, along with the possible variation in optimum periodicity based on the manufacturers variation in numerical aperture (NA).

Table 3.9. Theoretical Calculation of the Optimum Periodicity

Specimen #	Core Radius (um)	Manufacturers Data NA	Variation in NA	Core Index (No)	Calculated Theoretical Period (mm)	Manufactured Variation in Theoretical Period (mm) Minimum	Maximum
1	25	0.200	0.015	1.490	1.17	1.089	1.265
2	25	0.200	0.015	1.490	1.17	1.089	1.265
3	31.25	0.275	0.015	1.496	1.07	1.013	1.130
4	25	0.2	*	1.465	1.15	*	*
5	25	0.2	*	1.465	1.15	*	*
6	50	0.4	*	1.453	0.81	*	*
7	52.5	0.22	0.02	1.458	1.55	1.417	1.700
8	100	0.22	0.02	1.458	2.94	2.699	3.239
9	100	0.22	0.02	1.458	2.94	2.699	3.239
10	100	0.22	0.02	1.458	2.94	2.699	3.239
11	100	0.22	0.02	1.458	2.94	2.699	3.239

Where NA = numerical aperture, um = micrometers, and * = not available

3.4.3 Microbend Testing Equipment

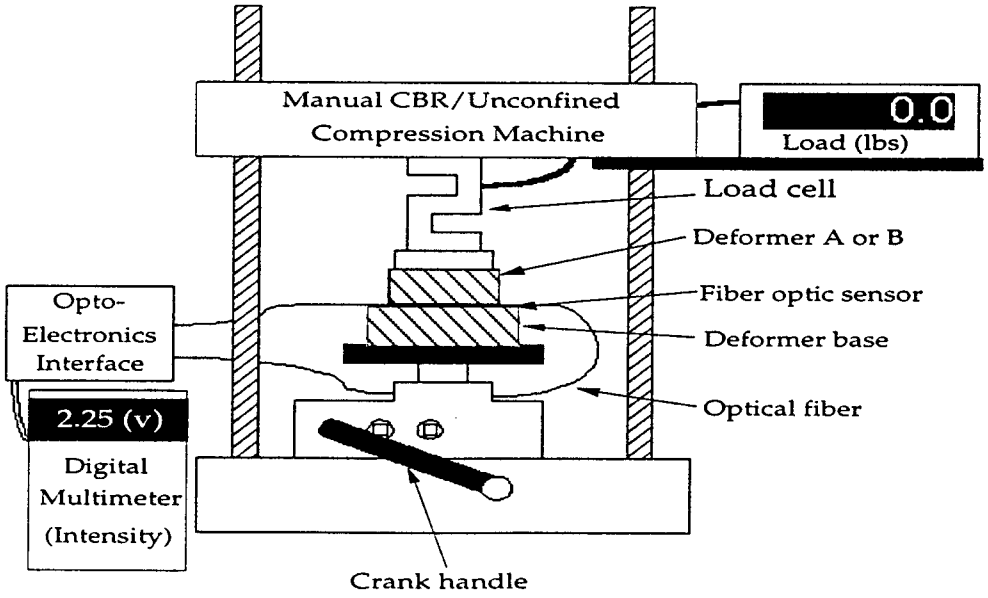

Figure 3.10. Schematic of Microbend Periodicity Test Setup

The bulk of the system consisted of a CBR (California Bearing Ratio) unconfined compression machine complete with a three-speed jack and 500 lb (227 kgs) load cell connected to a transducer indicator that gives the compression load in pounds. In the compression machine is the periodic deformer, consisting of two parts (Figure 3.11).

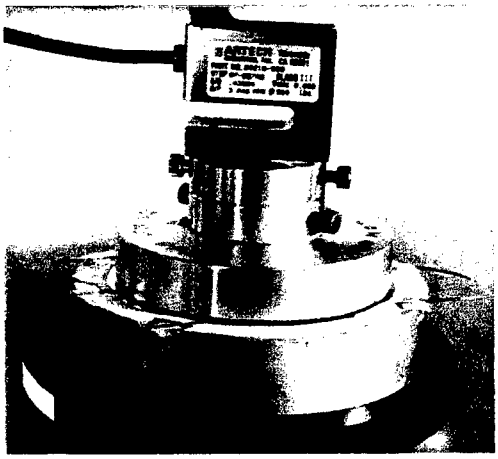

Figure 3.11. Top Deformer Plate and Bottom Base Plate in the CBR Machine

On the bottom, a polished base plate is used as a mount for the optical fiber and to indicate the degree at which the deformer plate is rotated. On the top, the deformer plate with periodically spaced teeth is set on the fiber. Figure 3.12 shows a view of the bottom base plate with a fiber and degree markings.

Figure 3.12. View of Top Plate with Deformer Corrugations and Base Plate Showing the Fiber and Degree Markings Used to Set Periodicity

To give an increased periodic range, two deformer plates were built and designated as plates A and B. The periodic range of deformer A was 1016-2032 μm and deformer B was 2007-4013 μm. Table 3.10 shows a summary of the deformer properties.

Table 3.10. Properties of the Microbend Deformer Plates

Deformer Plate	Tooth Height (μm/mils)	Tooth Width (μm/mils)	Period (μm/mils)	Periodic Sweep for 0°-60° Rotation (μm)	Contact Area (%)
deformer A	762/30	381/15	1016/40	1016-2032	37.5
deformer B	762/30	381/15	2007/79	2007-4013	19

The remaining portions of the system consisted of an opto-electronic interface and voltmeter. The optical fiber (connectorized with type ST bare fiber adapters) was plugged into the opto-electronics interface where the lead-in fiber was excited with an 850 nm LED (Light Emitting Diode). The optical power from the lead-out fiber was collected with a PIN (p-type, intrinsic, and n-type semiconductor) diode. The opto-electronic interface converted the received optical power to a voltage that could then be monitored with a DMM (Digital Multimeter). A detailed test procedure is given in Appendix C.

3.4.4 Investigation of Periodicity Testing Results

Periodicity Data

Figure 3.13 shows the load versus periodicity at 3dB intensity loss for the three acrylate coated Corning fibers subjected to microbending.

From Figure 3.13, three different optimum periodicities can be seen for each fiber. The first optimum is called the fundamental and the 2nd and 3rd are the harmonics. They are called harmonics because their periods are integer multiples of the fundamental's period. It is apparent from the graph that at the 1st harmonic period, each of the fibers had slightly greater sensitivity to load. Also, at each increase in harmonic period a corresponding increase in the width of the periodic range (i.e., width of the u-shaped curve) occurred. For the 62.5 μm core fiber (specimen 3), this width is less than half that of the 50 μm core fiber (specimen 1).

The 50/125/250 black auto-paint fiber, specimen 2, is the same as specimen 1, except for the layer of black automobile paint around its acrylate coating. Specimen 2 was more sensitive than either specimen 1 or specimen 3 at all of the peaks. Also, the width of the periodic range was more than twice that of specimen 1. It could be stated that the extra coating around the fiber affected the sensitivity of the fiber, increasing it in this case.

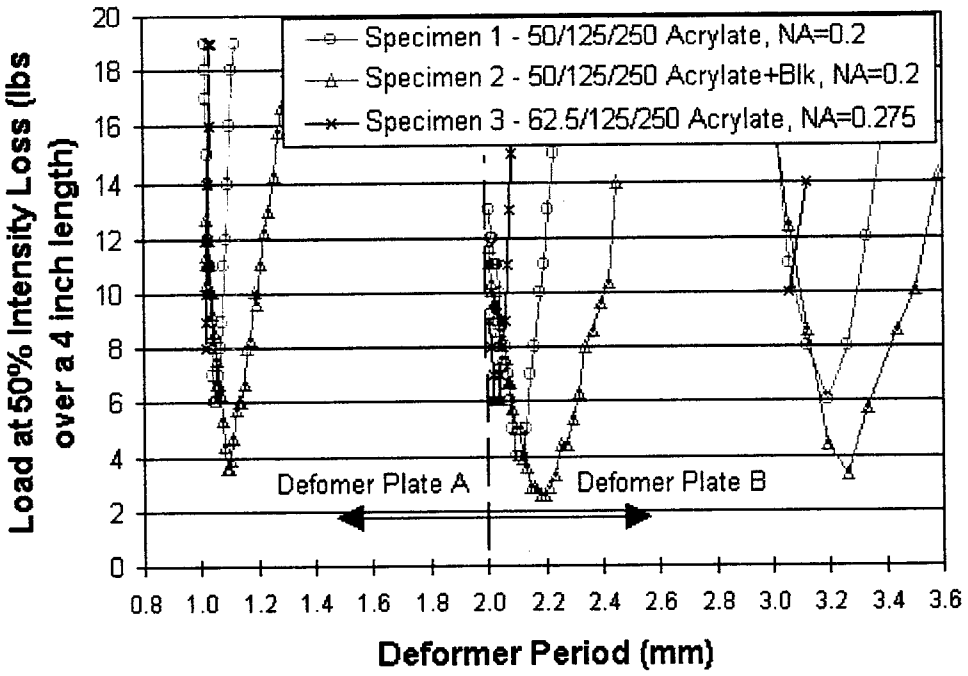

Figure 3.13. Load versus Period at 3dB Intensity Loss for Acrylate Coated Fibers

For the graded index gold and polyimide coated fibers (specimen 5 and specimen 4, respectively), the intensity losses were not as high as the acrylate coated fibers (35% and 65% intensity loss at 20 lbs (9 kgs) compared to 50% intensity loss at about 4 lbs, 1.8 kgs). Only the fundamental and 1st harmonic periods were measured. The polyimide coated fiber was almost twice as sensitive as the gold coated fiber at each peak. Figure 3.14 shows the intensity loss versus period for the gold and polyimide coated acrylate fibers.

As predicted for the step index fibers, the light loss was very small. For three of the six step index fibers tested, the optimum period could not be determined. For the three remaining fibers, the 105/125/145 polyimide, 200/240/265 polyimide, and the 200/240/310 aluminum (specimens 7, 10, and 11, respectively), the optimum periods are depicted in Figure 3.15.

The polyimide fiber with the smaller core (105/125) had more than twice the intensity loss at 20 lbs (9 kgs) than the polyimide fiber with a larger core (200/240). The numerical aperture and core index for all three of these fibers were the same (Table 3.9). The aluminum coated fiber had the same core size as the large core polyimide fiber, except for a thicker coating and in turn had an optimum intensity loss much closer to the large core polyimide fiber.

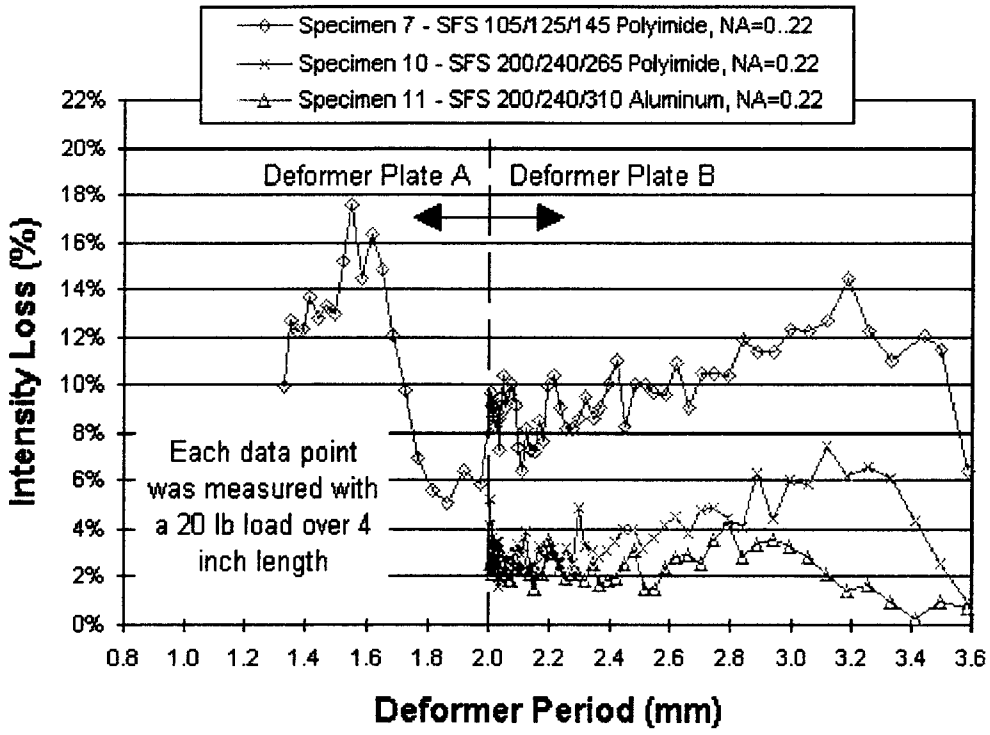

Figure 3.14. Intensity Loss versus Period at a 20 lb Load for Gold and Polyimide Coated Graded Index Fibers

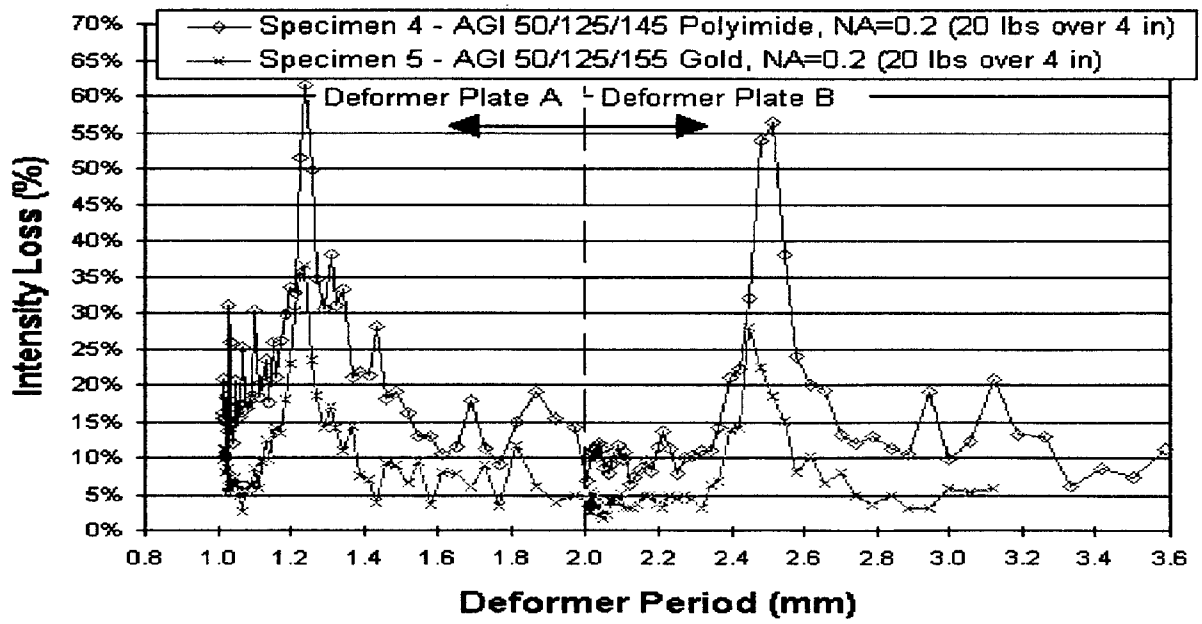

Figure 3.15. Intensity Loss versus Period for the Two Polyimide and One Aluminum Coated Step Index Fibers

A summary of the optimum periodicity tests results is presented in Table 3.11. The experimental period column gives the three optimum periods of each specimen. The fundamental period (labeled 1) is the period where the theory predicts the maximum sensitivity for microbending to occur. The next two periods are harmonics of the fundamental and their values are two and three times the fundamental period, respectively. The applied load at experimental period shows the load required to reach the desired intensity loss. This loss is given in the column labeled % intensity loss at experimental period.

Table 3.11. Experimental Periodicity Results

Spec. #	Core Dia. (um)	NA	Coating	Calculated Theoretical Period (mm)	Experimental Period (mm)			Applied Load at Experimental Period (lbs over 4 in)			% Intensity Loss at Experimental Period		
					1	2	3	1	2	3	1	2	3
1	50	0.2	Acrylate	1.17	1.06	2.11	3.19	6	4	6	50	50	50
2	50	0.2	Blk Auto Paint [1]	1.17	1.09	2.19	3.26	4	3	3	50	50	50
3	62.5	0.28	Acrylate	1.07	1.03	2.04	3.1	8	6	10	50	50	50
4	50	0.2	Polyimide	1.15	1.24	2.51	*	20	20	*	61	56	*
5	50	0.2	Gold	1.15	1.24	2.45	*	20	20	*	37	28	*
6	100	0.4	Nylon	0.81	Could not be determined								
7	105	0.22	Polyimide	1.55	1.55	3.19	*	20	20	*	17.6	14.5	*
8	200	0.22	TEFZEL	2.94	Could not be determined								
9	200	0.22	Blk TEFZEL	2.94	Could not be determined								
10	200	0.22	Polyimide	2.94	3.12	*	*	20	*	*	7.4	*	*
11	200	0.22	Aluminum	2.94	2.79	*	*	20	*	*	4.2	*	*

Where NA = numerical aperture, um = micrometers, * = could not be determined, and
1 = on an acrylate coated fiber

The data in Table 3.11 imply that the optimum experimental periods agree, with the manufacturers variation in numerical aperture (Table 3.10), except for a 3% difference for specimen 1. The applied load at experimental period indicates that the acrylate coated fibers were the most sensitive and the step-index fibers were the least sensitive.

For the design of microbend sensors, conversions of the experimental optimum periods in Table 3.11 were made. These conversions are presented in Table 3.12. Of particular use is the experimental period in bpi (bumps per inch), which corresponds directly to the (opi) openings per inch of mesh that could be used as microbend deformers. Opening size in mils is also given.

Table 3.12. Unit Conversions for the Optimum Periods from the Periodicity Tests

Spec. #	Core (um)	Coating	Experimental Period (bpi) 1	2	3	Experimental Period (mils) 1	2	3
1	50	Acrylate	24.0	12.0	8.0	41.7	83.1	125.6
2	50	Blk Auto Paint [1]	23.3	11.6	7.8	42.9	86.2	128.3
3	62.5	Acrylate	24.7	12.5	8.2	40.6	80.3	122.0
4	50	Polyimide	20.5	10.1	*	48.8	98.8	*
5	50	Gold	20.5	10.4	*	48.8	96.5	*
6	100	Nylon	Could not be determined			Could not be determined		
7	105	Polyimide	16.4	8.0	*	61.0	125.6	*
8	200	TEFZEL	Could not be determined			Could not be determined		
9	200	Blk TEFZEL	Could not be determined			Could not be determined		
10	200	Polyimide	8.1	*	*	122.8	*	*
11	200	Aluminum	9.1	*	*	109.8	*	*

Where NA = numerical aperture, um = micrometers, bpi = bumps per inch,
* = could not be determined, and 1 = on an acrylate coated fiber

Intensity versus Load Data

The sensitivity curves (intensity versus load) for each fiber are shown in Figure 3.16. The fibers with thicker coatings were much more sensitive to single-sided microbending effect than the thin coating fibers, with more than an order of magnitude difference in the sensitivities. The acrylate coated fibers have the largest usable ranges (95% intensity loss over loaded region) while the gold coated fiber has the next largest sensing range (50% intensity loss over loaded region). Both polyimide fibers have very small usuable ranges.

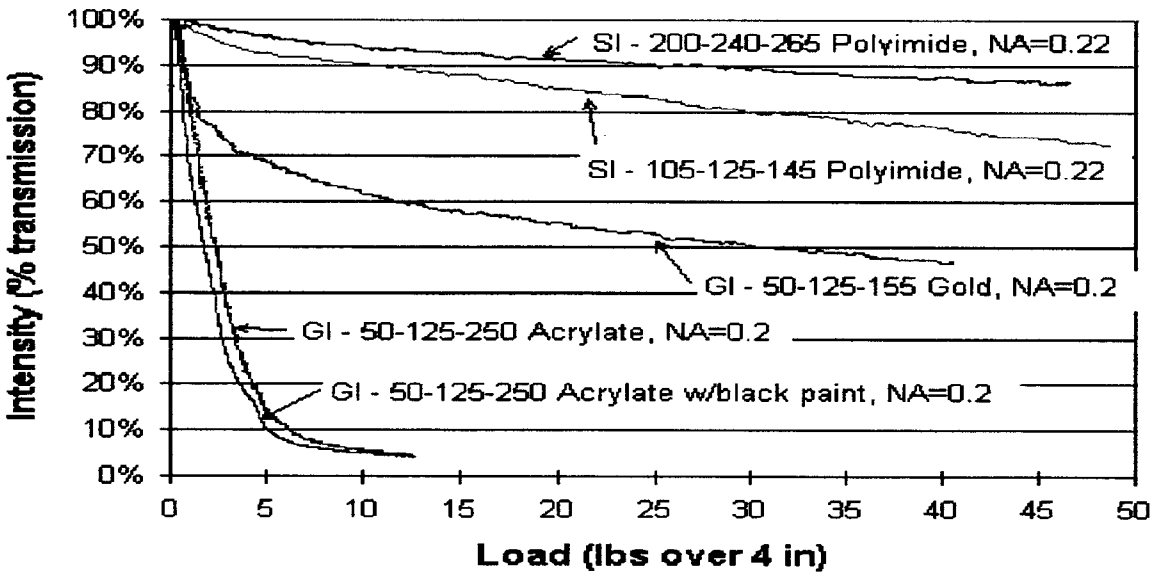

Figure 3.16. Sensitivity Curves for 5 of the Fibers Tested in the Periodicity Experiment (1 lb = 0.4541 kgs)

3.4.5 Summary of Periodicity Testing

The main conclusion that can be drawn from this experiment is that the optimum periodicity for all graded index and most step index fibers can be accurately measured using the experimental setup described. For each of the fibers the predicted fundamental periodicity was obtained within the limits of the numerical aperture variation.

For the black-painted acrylate fiber, the intensity loss and the periodic sensitivity range below 20 lbs (9 kgs) were greater than both of the other acrylate fibers. This variation may be due to an increase in the coating thickness; however, further testing should be done to determine the effects coatings have on sensitivity.

The lack of apparent intensity loss at the optimum periods for all of the other fibers (Specimen's 4–11) may be true only for the particular type of deformer (single-sided) used in this experiment. A test of each type of fiber with the original method of inducing the microbends (double-sided) at the optimum periods should be performed to observe the characteristics of the sensitivity for that type of sensor design. An experiment discussed in the next section was performed with two fibers from this test to observe some of these characteristics. The intensity versus load measured with the periodicity experiment would only be valid for the single-sided deformer, but the optimum period is valid regardless of the deformer technique.

3.5 COMPARISON BETWEEN SINGLE AND DOUBLE-SIDED MICROBEND DEFORMERS

In the reviewed references, the classical method of inducing the microbends has been the double-sided technique (Diemeer, M.B.J. and Trommel, E.S., 1984), (Lagaskos, N., 1987). The fiber is placed between two alternated sets of teeth and the two sides are compressed together to deform the fiber. This method is illustrated in Figure 3.17.

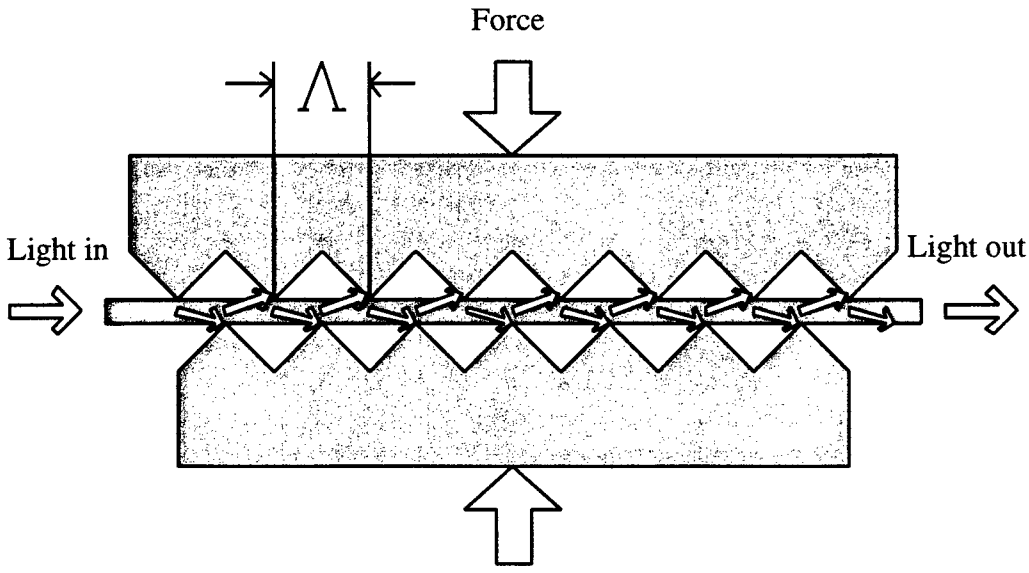

Figure 3.17. Double-Sided Microbend Inducing Mechanism

To measure periodicity, circular plates were designed with flat ridges to induce microbending in an optical fiber. To simplify the design of these measurement devices, only the top plate was designed with microbending teeth. The bottom plate was polished flat. Figure 3.18 illustrates the single-sided microbend deformers.

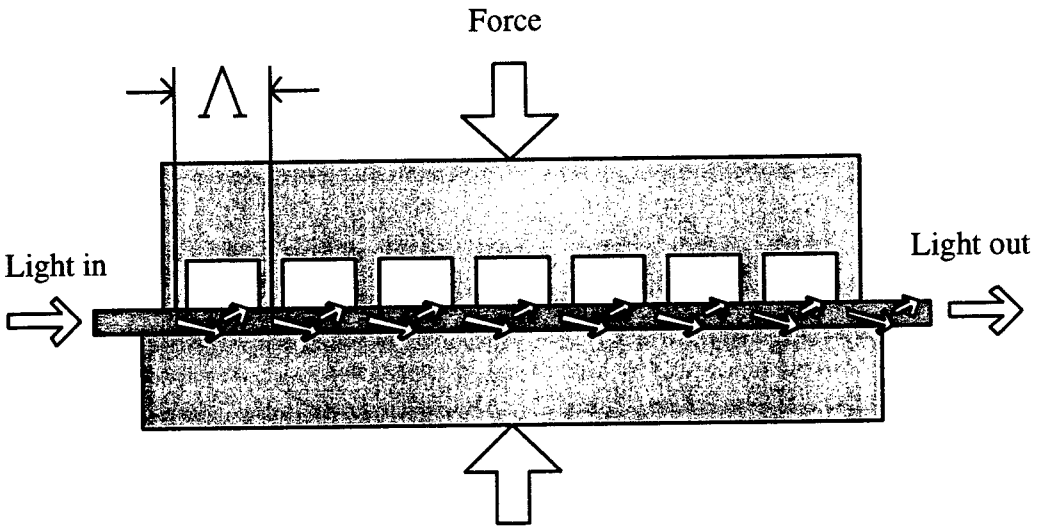

Figure 3.18. Single-Sided Microbend Inducing Mechanism

The comparison between single and double-sided microbending was investigated to examine their differences. Specifically, the intensity, load, and deflection information for polyimide and acrylate coated graded-index fibers will be examined.

3.5.1 Single and Double-Sided Microbend Deformer Testing

To conduct a microbend experiment acrylate and polyimide coated fibers with the same core/cladding diameter were placed into either single-sided or double-sided microbenders. The intensity, load, and deflection were measured during each test for each combination. Table 3.13 summarizes the properties of each fiber.

Table 3.13. Physical Properties of the Fibers for the Microbend Inducing Experiment

Coating Type	Silica Core/Cladding Diameters (μm)	Outer Diameter of Coating (μm)	Numerical Aperture
Acrylate Polyimide	50/125 50/125	250 145	0.200 0.2

The core/cladding size for each fiber was the same, but the coating type and thickness were different. The slight difference in numerical aperture meant that the modal coupling period of each fiber would be slightly different.

Figure 3.19 diagrams the design of the base deformer with its matching top deformer. The round rods for the deformers were made of steel and the mounting plates were made of flat, polished aluminum.

Figure 3.20 is a photograph of the top and bottom microbend deformers with a fiber laid across the teeth of the bottom plate to show the placement of the fiber during testing. A detailed procedure for these experiments is given in Appendix D.

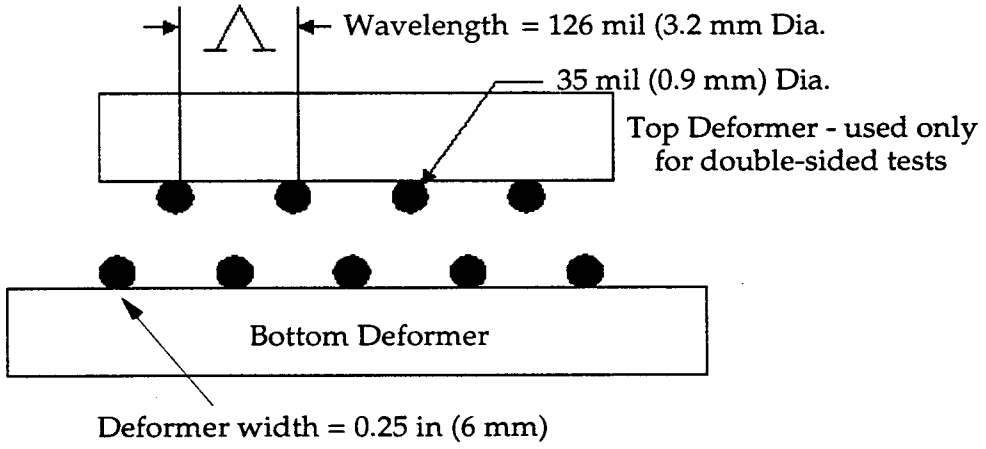

Polyimide fiber dia. = 5.7 mils (145 μm)
Acrylate fiber dia. = 9.8 mils (250 μm)

Figure 3.19. Microbend Deformer Dimensions

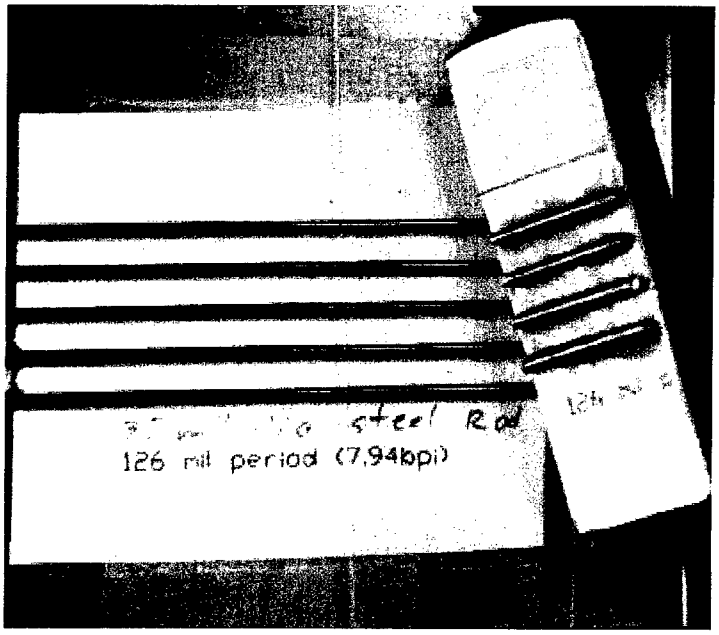

Figure 3.20. Photograph of the Top and Bottom Deformers for the Microbend Inducing Experiment

3.5.2 Results of the Single and Double-Sided Microbend Deformer Testing

The intensity versus load curves for the acrylate and polyimide fibers for both microbend processes are presented in Figure 3.21.

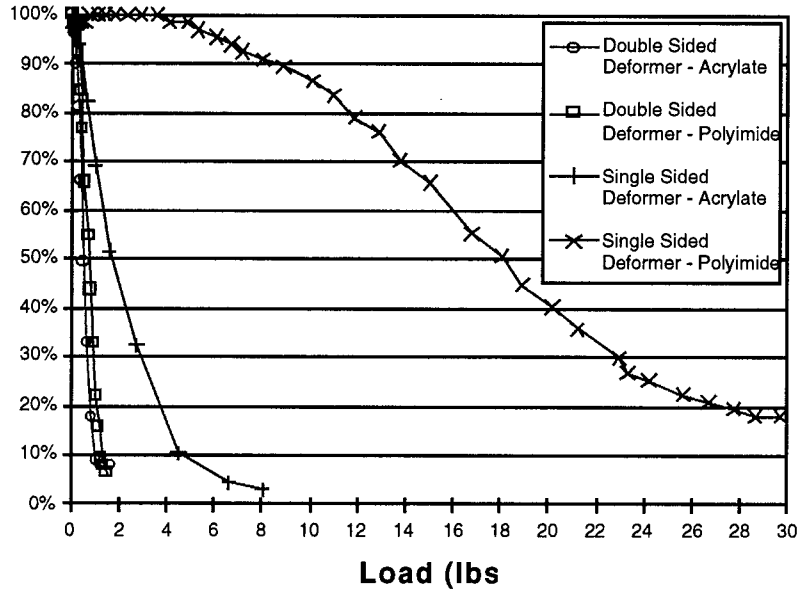

Figure 3.21. Intensity versus Load for the Polyimide and Acrylate Coated Fibers in the Single and Double-Sided Microbend Deformers

For both fibers with double-sided deformers, the intensity loss curve was nearly the same and the sensitivity at 50% light loss was very small (just under 1 lb at 50% intensity). Both curves exhibited high intensity loss once the load was applied, decreasing in a linear fashion to about 20% intensity transmission. The intensity loss curves for the single-sided deformers, however, were different from the double-sided deformers. For the acrylate coated fiber, the curve decreased in an exponential manner once the load was applied to nearly zero light intensity transmission. For the polyimide coated fiber the intensity did not begin to decrease until nearly 4 lbs (1.8 kgs) of load was applied, after which it decreased in a nonlinear manner, leveling off at about 18% intensity transmission around 29 lbs (13 kgs). From Figure 3.21 it can be concluded that fibers in the double-sided deformers are more sensitive and have a greater linearity than those in the single-sided deformers.

Intensity versus displacement results for the four combinations of fibers/deformers arepresented in Figure 3.22.

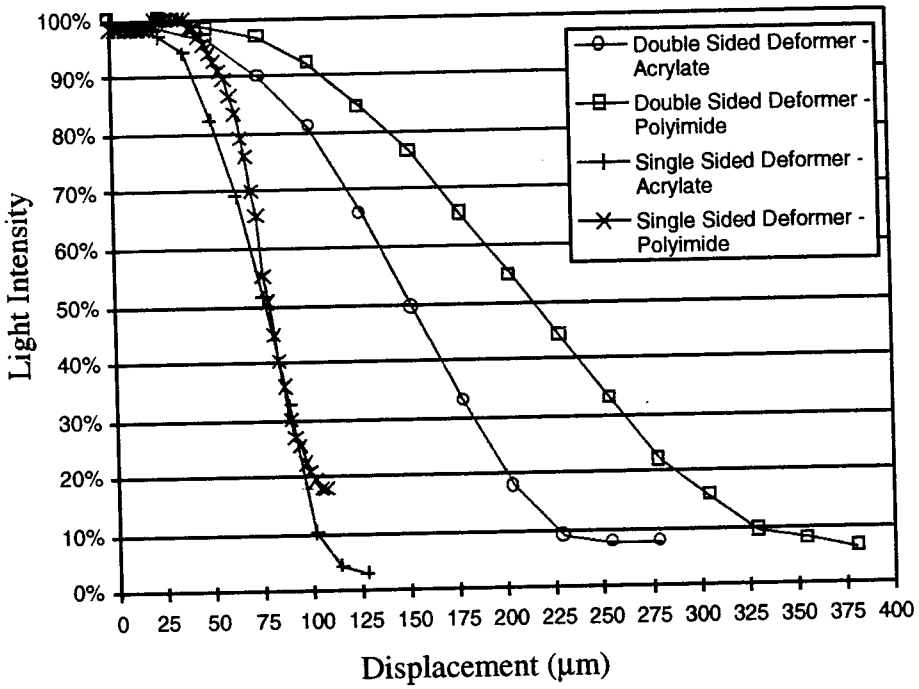

Figure 3.22. Intensity versus Displacement for the Polyimide and Acrylate Coated Fibers in the Single and Double-Sided Microbend Deformers

The intensity versus displacement curves for all cases exhibited similar shapes with varying degrees of magnitude in displacement. For the polyimide fiber in the single-sided deformer, though, the intensity drop, occurred over a smaller displacement range than the other combinations (about 40 μm from 90% to 20% intensity transmission). It appears that fibers in the double-sided deformers can traverse a much greater displacement than those in the single-sided deformers. However, changes in the spatial wavelength and deformer diameter/shape of the double-sided mechanism could change how much displacement the fiber may undergo, which in turn affects the amount of intensity loss that may occur. The same statement may also be made about the design of the single-sided deformers. Table 3.14 summarizes

several characteristics of the fiber and deformer combinations extracted from Figure 3.21 and Figure 3.22.

Table 3.14. Load and Displacement Characteristics for the Four Fiber/Microbend Inducing Combinations

Fiber	Deformer Type	Load at 50% Intensity (lbs)	Change in Load form 90% to 20% Intensity (lbs)	Displacement at 50% Intensity (υm)	Change in Displacement form 90% to 20% Intensity (υm)
Acrylate	Double-Sided	0.6	0.6	150	125
Polyimide	Double-Sided	0.9	0.7	215	175
Acrylate	Single-Sided	1.7	3.4	76	50
Polyimide	Single-Sided	18.2	19	78	40

3.5.3 Summary

From this experiment it was demonstrated that fibers in a double-sided deformer are more sensitive than the same fibers in a single-sided deformer with the same period. However, larger displacements are necessary to achieve this sensitivity. As the load versus deflection data indicates the sensor with double-sided deformers is not as stiff as the single-sided microbender. For the traffic sensor to work properly it may be advantageous to have the sensor work at smaller deflections.

The thinly coated polyimide fiber, in the single-sided deformer, is not as sensitive as the thickly coated acrylate fiber (*18.2 lbs (8.2 kgs) at 50% intensity loss versus 1.7 lbs (0.8 kgs) at 50% intensity loss, respectively*). This finding would support the observations in sensitivity from the optimum periodicity experiment, where the thinly coated fibers, even at their optimum period, were not as sensitive as the thick-coated acrylate fibers with the same basic core/cladding characteristics (*6.0 lbs (2.7 kgs) at 50% intensity loss versus 20 lbs (9 kgs) at 61% intensity loss, respectively*). It can now be stated that of the fibers tested, the thick-coated acrylate fibers would be the most desirable choice for a sensor design with single-sided deformers.

CHAPTER 4

4.0 FIBER-OPTIC MICROBEND TRAFFIC SENSOR DESIGN

A fiber-optic microbend sensor has been designed for use in traffic applications. The sensor design was performed using the results of the optimum periodicity and microbend, inducing experiments discussed in Chapter 3. A mesh/fiber combination was chosen and constructed into a long, flexible microbend sensor. The flexible sensor was then placed into a watertight packaging. Laboratory testing of the optical sensor was performed to determine sensor characteristics prior to field installation.

4.1 CHOOSING A FIBER AND MESH FOR THE MICROBEND SENSOR

The acrylate coated optical fibers were chosen for the microbend sensor design because of their good sensitivity with the single-sided microbending mechanism, optimum periodic spacing, and availability. Table 4.1 shows the various parameters for these fibers including the optimum periodicity as experimentally determined in the previous section. Using the value of optimum periodicity in bumps per inch, four types of readily available mesh were obtained with periodic spacings covering a range near the optimum for both of the acrylate fibers. Table 4.2 lists the four types of mesh and their spacing.

Table 4.1. Properties of the Corning Acrylate Coated Fibers

	Fiber 1	Fiber 2
Manufacturer	Corning	Corning
Core Diameter (μm)	50	62.5
Cladding Diameter (μm)	125	125
Coating Diameter (μm)	250	250
Coating Material	Acrylate	Acrylate
1st Optimum Periodicity (mm)	1.06	1.03
1st Optimum Periodicity (bumps per inch)	24.0	24.7

Note: 1 inch = 2.54 cm

Table 4.2. Four Types of Mesh Selected for Determining the Most Sensitive Microbend Sensor

Mesh Material	Spacing (bumps per inch)
Polypropylene A*	24^{1} x 20
Polypropylene B*	23^{1} x 23
Tefzel®	23.5^{1} x 23.5
Nylon	24.7^{1} x 25.1

[1] designates deformation period on fiber
*polypropylene A is not the same mesh as polypropylene B
Note: 1 inch = 2.54 cm

Eight microbend sensors were built using each of the four meshes with each of the two acrylate fibers. They were six-inches long, one-fourth-inch wide, and had a loop at one end. Figure 4.1 diagrams their construction. First, spray adhesive was used to hold the mesh to the bottom piece of G10 fiberglass.

Then, it was used to hold the optical fiber onto the mesh, where the fiber was placed so it did not cross the lengthwise strips of the mesh. Spray adhesive was finally used to hold the top piece of G10 fiberglass to the fiber, completing the construction process.

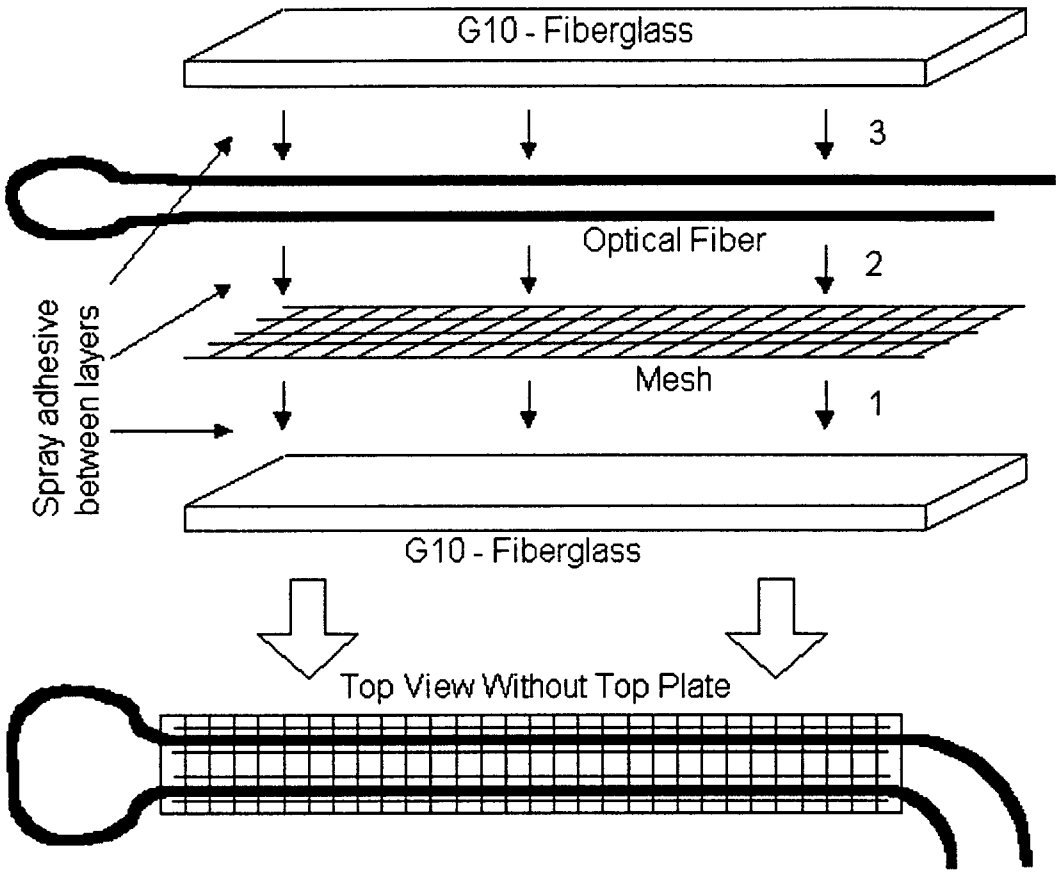

Figure 4.1. Six-Inch Sensor Construction

Once all eight sensors were built, the lead-in and lead-out fibers were stripped and cleaved. Each sensor was subjected to load versus intensity testing in the CBR loading machine. The lead-in and lead-out fibers were fitted with the bare fiber adapters and inserted into the opto-electronics interface. A digital storage scope was connected both to the output of the load cell indicator and the opto-electronics interface to record the load in terms of voltage and output intensity, respectively.

The digital storage scope was set to sample at 5 seconds per division for 50 seconds of total storage. After pressing the hold button to begin the acquisition on the scope, the low-speed handle of the CBR machine was slowly rotated, increasing the load on the sensor. This process was continued until the decrease in light intensity appeared to stop. The hold button was pushed to stop the acquisition and the load was released from the sensor. The data on the scope was downloaded to the laptop computer for later analysis. This procedure was repeated three times with each of the eight sensors.

The data from the scope was brought into a spreadsheet where the intensity was normalized and the load was scaled from voltage to pounds. Plots of the intensity versus load was constructed for each of the eight sensors (Appendix E).

Table 4.3 summarizes the results of the intensity versus load testing for the eight microbend sensors. Each of the curves in Appendix E have a similar shape where there is an initial steep linear region followed by a flat region at the end of the sensors range. The linear range went from 100% intensity transmission to an average of about 45% intensity loss. The maximum extent of this linear range was 70% intensity loss with the Corning 62.5/125/250 fiber, polypropylene mesh. The minimum extent of linear range was 15% intensity loss associated with the Corning 62.5/125/250 fiber and Tefzel® mesh. The differences between these two sensors are the diameter of the mesh strands, the mesh material, and the periodicity of the mesh.

Table 4.3. Load at 50% Intensity for the Eight Six-Inch Microbend Sensors

Mesh Material	Mesh Period (mm)	Fiber	% Difference in Period	Load at 50% Intensity (lbs) Curve 1	Curve 2	Curve 3	Curve Average
Polypropylene A*	1.06	50 mm	0%	4	6.5	11	5.38
Polypropylene A*	1.06	62.5 mm	3%	4.9	4.9	5.2	3.76
Polypropylene B*	1.10	50 mm	4%	6.3	9	10.3	6.41
Polypropylene B*	1.10	62.5 mm	7%	7.5	8.5	9	6.27
Tefzel**	1.08	50 mm	2%	3	3.5	4	2.63
Tefzel	1.08	62.5 mm	5%	***	***	***	***
Nylon	1.03	50 mm	3%	11.5	12.5	13.5	9.38
Nylon**	1.03	62.5 mm	0%	4	4.4	5	3.35

*polypropylene A is not the same mesh as polypropylene B
**denotes most sensitive combinations
***intensity did not fall below 50%

The sensor with the maximum extent in linear range would be the most desirable. Excellent repeatability and useful ranges were shown with Corning 62.5/125/250 - 24x20 polypropylene, Corning 62.5/125/250 - 23x23 polypropylene, and Corning 50/125/250 - 23.5x23.5 Tefzel® combinations. All three of these combinations could have been used; however, because of availability of materials, the Corning 50/125/250 fiber on Tefzel® mesh was chosen as the microbend sensor for WIM. The extent of its linear range was about 55% and had a very smooth flattening out. The final intensity loss at 30 lbs (13.6 kgs) was 96%, but was at 90% intensity loss at only 12 lbs (5.4 kgs). The 50/125/250 fiber on Tefzel® mesh had the least load at 50% intensity loss, meaning it had the steepest linear range of all eight combinations.

4.2 PACKAGING THE MICROBEND SENSOR

A microbend sensor installed into the surface layers of a pavement must have adequate protection from its surroundings, but not so much that it significantly affects the sensor operation. Of utmost importance is the protection against water intrusion. Because the microbend sensor functions by displacing between the top and bottom plates to cause microbending in the optical fiber, any material within this space needs to be easily compressible. Water does not easily compress in the range of stresses expected. If it comes

between the top and bottom plates and the sensor is loaded at a high rate, the increase in water pressure would cause the fiber to move from between the plates, possibly shifting the fiber on the mesh. The microbend sensor may quickly become inoperable.

A unique method of packaging the microbend sensor was developed. Using the dimensions of the 50 mm fiber sensor with the Tefzel® mesh and fiberglass top and bottom plates (custom length × 1/4 inch wide × approximately 1/16-inch (0.16 cm) thick), a 1/4-inch (0.64 cm) diameter heat shrink tube was acquired, cut to length, and slid over the fiber-optic sensor. The entire assembly was then placed on top of 300° F aluminum plates, where the heat shrink slowly and evenly shrank around the structure of the microbend sensor. After about 30 seconds, the sensor was flipped over and placed back on the plates for another 15 to 30 seconds. The sensor was then placed on top of a flat surface to cool to room temperature. The heat-shrink package was thin and flexible, leaving only the lead-in/lead-out and loop ends to seal, which was accomplished with other pieces of heat-shrink tubing and 5-minute epoxy.

This packaging technique was adaptable to any sensor length by overlapping long pieces of heat shrink by 1/2 inch (1.3 cm) and heating them. The packaged sensor was thin, flexible, sensitive, and waterproof. For this research, a 6-foot-long (1.8 m) microbend sensor was constructed, as depicted previously in Figure 4.1, with a 50/125/250 mm acrylate coated Corning fiber on a Tefzel® 23.5x23.5 bpi mesh (designated ARL 1) after which it was packaged in the heat-shrink tubing described above. The completed sensor then underwent various tests in the laboratory to determine its characteristics prior to field installation.

4.3 LABORATORY SENSOR EVALUATION

Several properties of a long microbend sensor are critical for its use. The intensity versus load curve can be used to give the sensitivity of the sensor over a fixed loading length (such as 2 inches (5 cm)). By using different loading lengths (i.e., 2 and 6 inches (5 and 15 cm)), the effect of loading length if significant should be observed in the sensitivity. These curves can also be taken at various positions along the 6-foot (1.8 m) sensor to determine signal variations with length. In addition to the CBR testing, a special test was designed to evaluate signal variations along the sensor. A loaded, rigid roller was moved along sensors fixed to a flat surface. While moving along the sensor, the intensity was monitored with a digital storage scope, giving an estimate of the variation in sensitivity along the sensor length.

4.3.1 Discontinuous Intensity Versus Length Evaluation

The procedure for measuring the intensity versus load was previously described. The lead-in and lead-out fibers of the sensor were stripped, cleaved, and inserted into bare fiber adapters that were connected to the opto-electronics interface. A digital storage scope was used to capture the load and intensity voltages for the microbend sensor.

The slow handle of the CBR (71.1 mm per revolution) was rotated while the storage scope captured the load and intensity voltages. The load was increased until the intensity was within a few percent of zero or until it stopped changing. The storage scope signals were captured and the load was released from the sensor. The sensor was then moved to a different position for testing and the data downloaded from the scope to a computer for analysis. This procedure was repeated for six positions along the sensor.

The procedure of measuring the intensity versus load was performed on the microbend sensor ARL 1 built for this research using a 2-inch and 6-inch (5 and 15 cm) loading length. Figure 4.2 shows the sensitivity for the 2-inch (5 cm) platen while Figure 4.3 shows the sensitivity for the 6-inch platen.

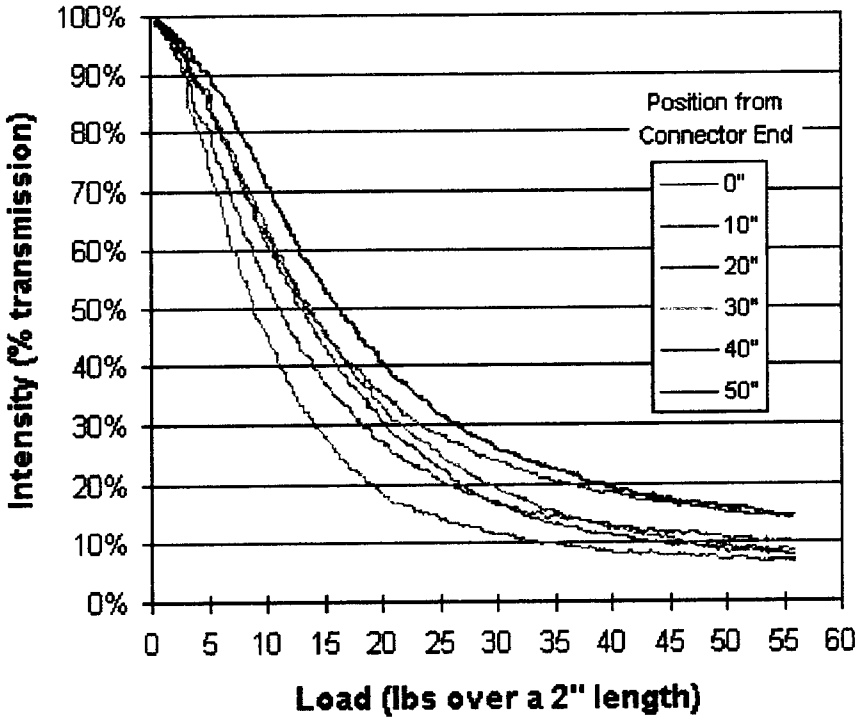

Figure 4.2. Intensity versus Load for a 2-Inch Platen (1 inch = 2.54 cm, 1 lb = 0.4541 kgs)

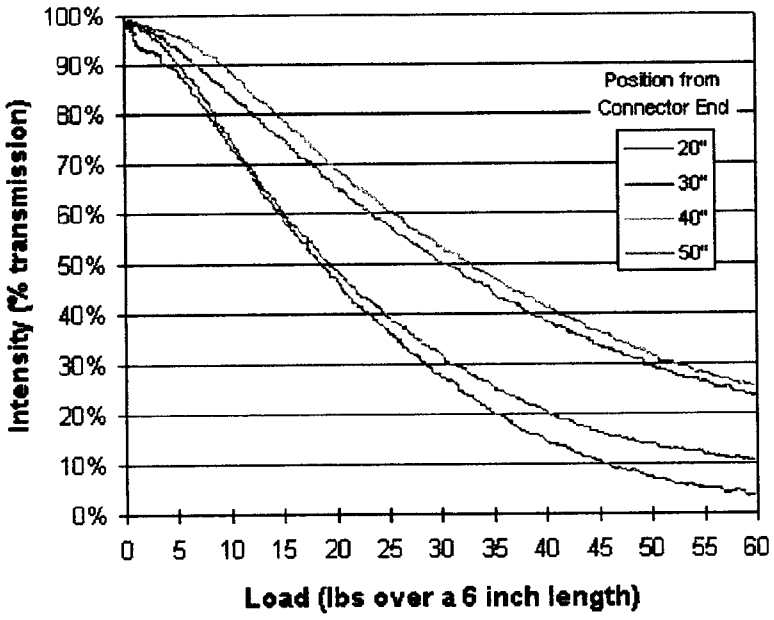

Figure 4.3. Intensity versus Load for 6-Inch Platen (1 inch = 2.54 cm, 1 lb = 0.4541 kgs)

Table 4.4 presents the load at 50% intensity from the curves in Figure 4.2 and Figure 4.3.

Table 4.4. Summary of the Loads at 50% Intensity Loss for Microbend Sensor ARL 1

Position from Connector End (in)	2-Inch Platen Load at 50% Intensity (lbs)	6 Inch Platen Load at 50% Intensity (lbs)
0	13	*
10	9	*
20	12.5	30
30	14	19
40	11	18
50	16	32.5
Average	12.6	24.9
Standard Deviation	2.4	7.4

*data not available
Note: 1 inch = 2.54 cm, 1 lb = 0.4541 kgs

The slope of the intensity versus load curves for the 2-inch (5 cm) platen is greater than the slope for the 6-inch (15 cm) platen, showing that it is more sensitive. The average load at 50% intensity for the 2-inch (5 cm) top plate is 12.6lbs (5.7 kgs) while it is more than double this for the 6 inch (15 cm) platen, it is 24.9 lbs (11.3 kgs). The standard deviation for the 6-inch (15 cm) platen is more than double the standard deviation for the 2-inch (5 cm) platen. The variation of the curves appears to be random. The linear range for the 2-inch (5 cm) platen is from about 90% to 50% intensity transmission, which is larger than the linear range of 90% to 60% intensity transmission for the 6-inch (15 cm) platen. It can be seen that for both cases, the sensitivity varies along the length. The force per unit length for the 6-inch (15 cm) platen is less than the force per unit length for the 2-inch (5 cm) platen. This was determined by dividing the average load at 50% intensity loss by the platen length ($\frac{L_{50\%\_I}}{l_{platen}}$), giving 6.29 lbs/in (5.46 kg/cm) and 4.15 lbs/in (3.6 kg/cm) for the 2-inch and 6-inch (5 and 15 cm) platens, respectively.

4.3.2 Continuous Intensity Versus Length Evaluation

Because the variation along the sensor was so great, a method of exclusively measuring the sensitivity along the length, called the track test was developed. The testing setup consisted of two long aluminum rails 3/4-inches (1.9 cm) high spaced 7.25-inches (18.4 cm) apart mounted to a solid wood table. The microbend sensor under test was taped down symmetrically in the center of the two rails and the lead-in and lead-out fibers were connected to an opto-electronics interface. A digital oscilloscope was connected to the voltage output of the opto-electronics interface and the intensity transmission with zero load was recorded. A self-propelled cart built from LEGO® components with a rigid roller in its center was placed in the track, with the rigid wheel centered on top of the sensor. A four-pound lead weight was then placed on the cart, directly above the roller (Figure 4.4). The electric motor was started and the cart was rolled down the sensor at a constant velocity. During testing, the digital storage scope recorded the light intensity from the sensor. The contact area of the rigid roller was estimated as the width of the sensor (5/16-inch, 0.8 cm)) by 1/16-inch (0.16 cm), or 0.02 in^2 (0.13 cm^2).

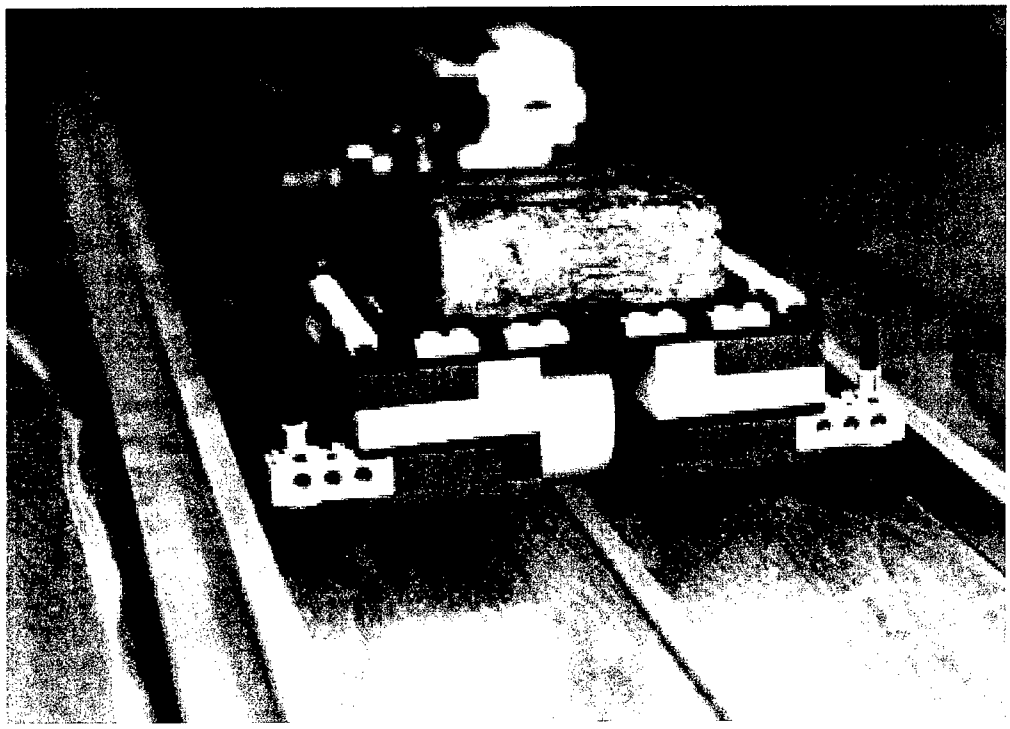

Figure 4.4. Loaded Cart with Rigid Roller for Sensor Intensity versus Length Testing

The sensitivity along the length of microbend sensor ARL 1 was measured four times with this testing setup. The intensity transmission along the length for the first and last measurements were presented in Figure 4.5. To quantify the variation along the length, the frequency of occurrence of intensity loss from the first and last measurements were presented in Figure 4.6.

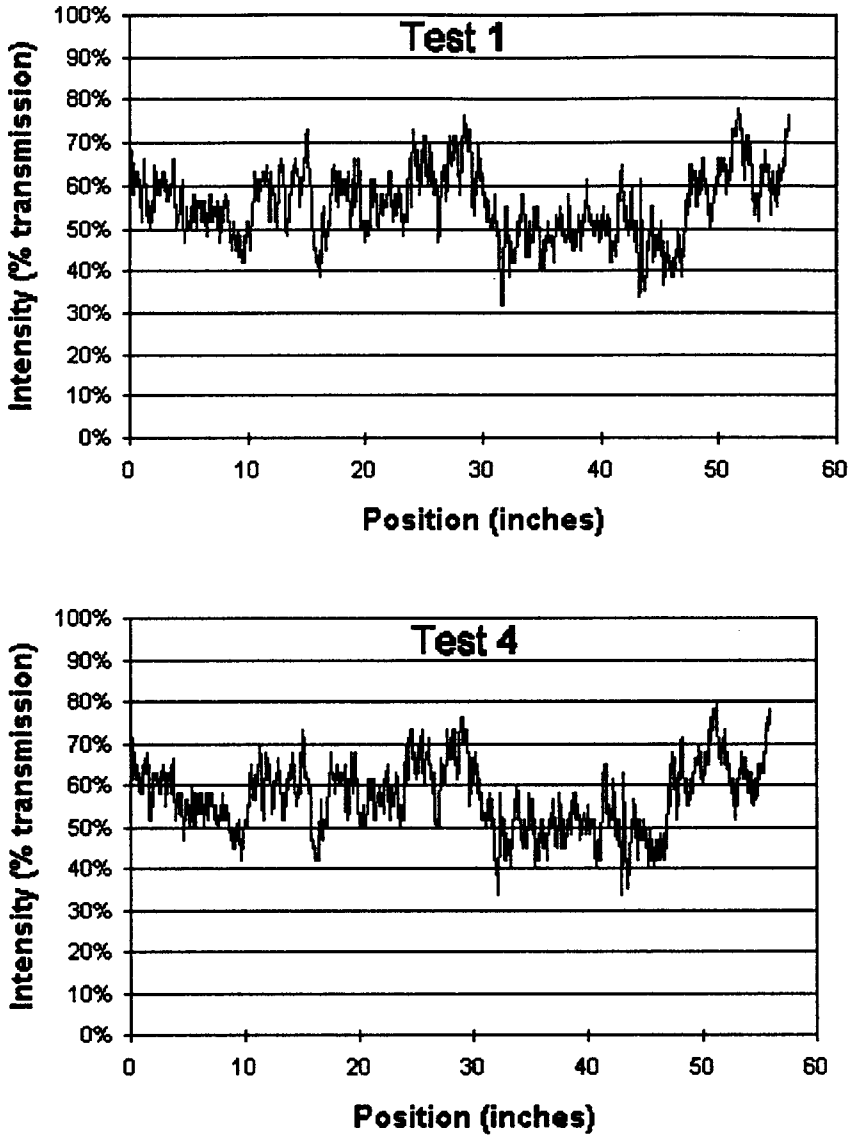

Figure 4.5. Intensity versus Length for Microbend Sensor ARL 1 (Tests 1 and 4) (1 inch = 2.54 cm)

From Figure 4.5 both the first and last intensity curves look identical. The mean and standard deviation for the first and fourth test are 44.3% intensity loss with a 7.9% deviation and a 42.9% intensity loss with an 8.0% deviation. From maximum to minimum, a 40% variation in intensity transmission existed. The causes of this variation are very narrow and may not have been seen with the large loading lengths of the CBR machine. Figure 4.6 presents the frequency distribution of intensity loss (5% bins) for tests 1 and 4 and confirms that the track test produces repeatable results.

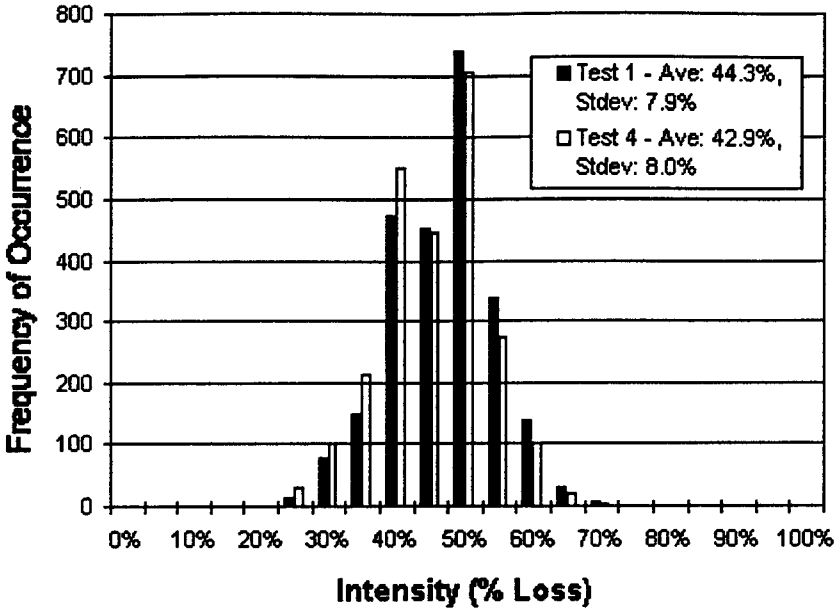

Figure 4.6. Distribution of Intensity Loss for Microbend Sensor ARL 1 (Tests 1 and 4)

The mean and standard deviation for this data are nearly identical. Table 4.5 shows the mean and standard deviation for all four runs. It was concluded that the continuous test track provided useful data; however, a separate study needed to be performed to determine if there were any inherent equipment problems that would have caused the large variations.

Table 4.5. Mean and Standard Deviation from Four Runs Using Track Testing of Microbend Sensor ARL 1

Test	Average Intensity Loss (%)	Standard Deviation (%)
1	44.3	7.9
2	44.9	8.0
3	43.5	7.9
4	42.9	8.0

4.3.3 Summary of Laboratory Evaluation

The intensity versus load testing with a microbend sensor is necessary to evaluate signal variations along the sensor. The variation in intensity loss from the discontinuous intensity versus load data appeared to be random. Many curves should be acquired along the length of the sensor to produce a better approximation of the intensity versus load for the sensor. From the continuous intensity versus length test, it was shown that repeatable intensity profiles could be obtained from a fiber-optic microbend sensor. The histogram created from the intensity versus load data provided useful insight into the mean and standard deviation of intensity variation. In the future, additional information could be obtained from this test if the loading rate and the applied load could be changed.

4.4 OPTO-ELECTRONICS INTERFACE

A key component in the fiber-optic sensor system is the opto-electronic driver. It generates the optical signal which is acted upon by the sensor. The thruput signal is proportional to the load on the sensor. For test purposes a three channel opto-electronic interface box was designed and constructed.

The 3-channel box used to drive the FOTS is shown below (Figure 4.7). It works from a 12V battery and consumes approximately 100mA (milliamperes). The front panel contains six ST-fiber-optic connectors, three LEDs, and three PIN diode receivers. The front also includes an analog voltmeter to adjust the receiver voltage in the field when the automatic gain control (AGC) is not in use. This ensures that calibrated measurements are taken at all times. The back panel contains the electronic connectors for data acquisition equipment and PEEK® classification boxes (Figure 4.8). Within the right side of the interface is a small cooling fan that can be used in case of high temperatures.

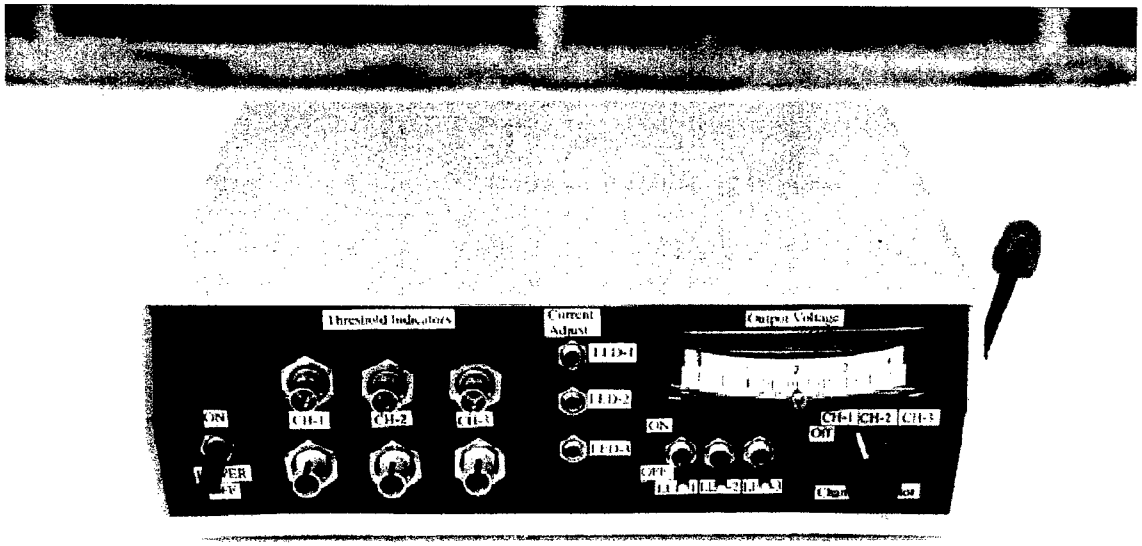

Figure 4.7. Opto-Electronics Interface (Front Panel)

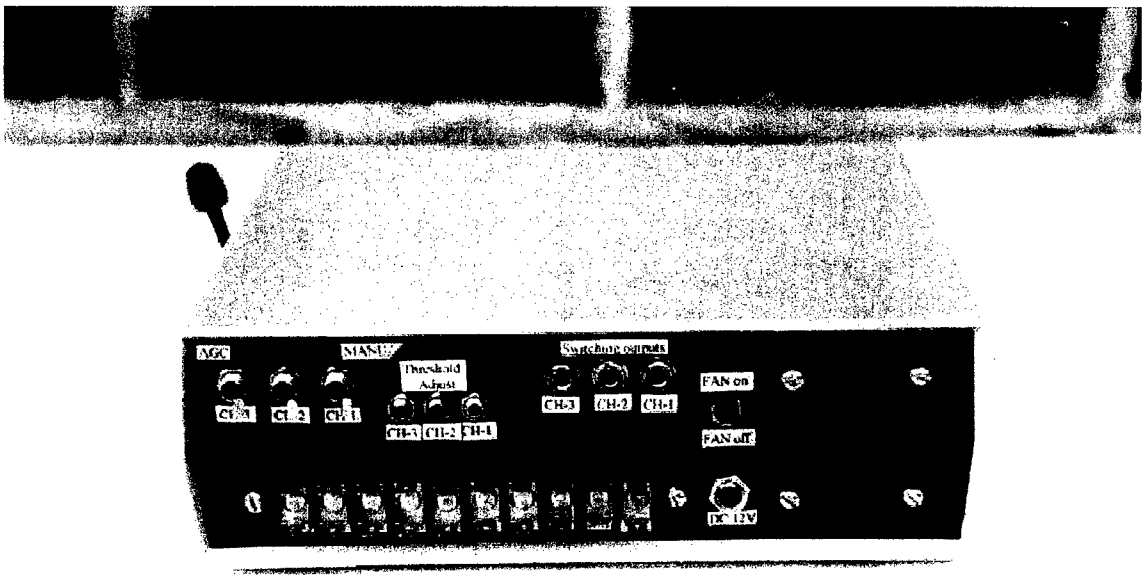

Figure 4.8. Opto-Electronics Interface (Back Panel)

The electronics of the 3-channel box consists of one common power supply and three identical opto-electronic driver units. The schematics of the power supply is shown in Figure 4.9. A voltage regulator was used to provide a constant five volts. The power supply gives two voltages; 12 volts (a reference voltage) and 5 volts. The three-pin voltage regulator is mounted on a heat sink. When the voltage level goes below a predefined limit it triggers two LEDs. The first is a regular red LED and the second is an encapsulated LED with a phototransistor to activate a digital input like the ones PEEK® classifiers have. The single analog voltmeter has a channel-selector switch to display one of the channels each time.

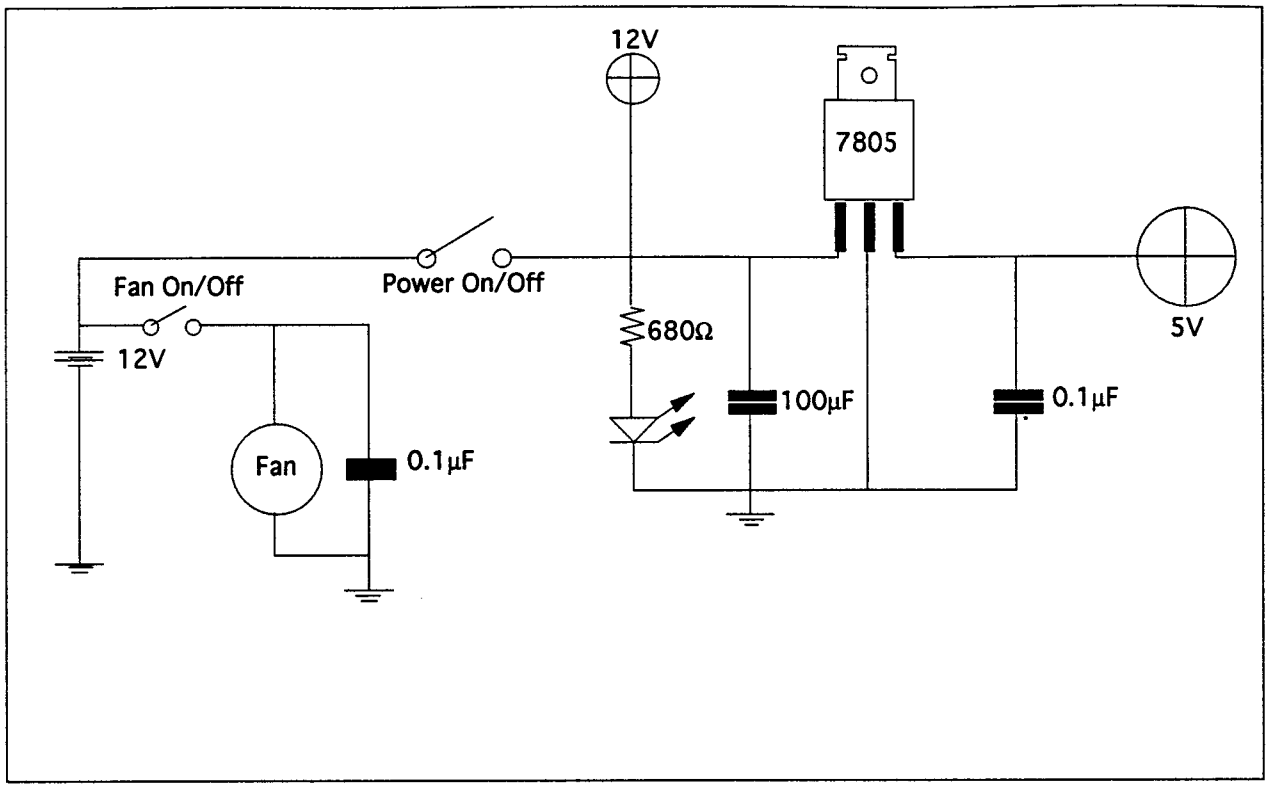

Figure 4.9. Schematics for Opto-electronic Interface Power Supply

The schematic is a one-channel driver. The LT1413 dual operational amplifier (op-amp) serves as the automatic gain control and as a unity gain amplifier for the receiver. When the 10K potentiometer is adjusted to a level voltage the first op-amp drives the infrared LED. If the receiver receives more or less light due to temperature differences, the voltage level at the negative input of the first op-amp will change and the amplifier will provide the LED with current to bring the set-level back. The 1 micro-Farant capacitor produces the delay. All references are temperature stable due to the use of an LM399 (National Semiconductor) precision voltage reference. This microchip is a zener diode and a resistor in a one-thermal insulated cup. The resistor serves as the heating element and keeps the temperature of the zener constant at 60° C. The analog output of the receiver was monitored for the data acquisition hardware and software which is also going to a comparator (LM392). This comparator checks to see if the voltage level goes below a predefined limit, and if so, it triggers two LEDs. The first is a regular red LED and the second is encapsulated with a phototransistor to activate a digital input like the ones PEEK® classifiers have. The single analog voltmeter has a channel-selector switch to display one of the channels.

CHAPTER 5

5.0 FIBER-OPTIC SENSOR SYSTEMS FOR TRAFFIC APPLICATIONS

5.1 INSTALLATION OF FIBER-OPTIC MICROBEND SENSORS IN PAVEMENTS

Installation procedures for placing fiber-optic sensors into the pavement were modeled after the process used for installing piezoelectric sensors due to the similarity in shape of both sensors. Both sensors are placed in grooves cut into the pavement with a street saw, which has depth control to make a consistent cut over a long length. However, the fiber-optic sensors are designed to be installed below the surface of the pavement, while the majority of piezoelectric sensors are installed with a portion exposed approximately 1/16-inch above the pavement surface. Figure 5.1 shows a cross-section of both a piezoelectric sensor and a fiber-optic sensor installed in a pavement. Roofing asphalt is one of several filler materials being evaluated for placement over the sensor.

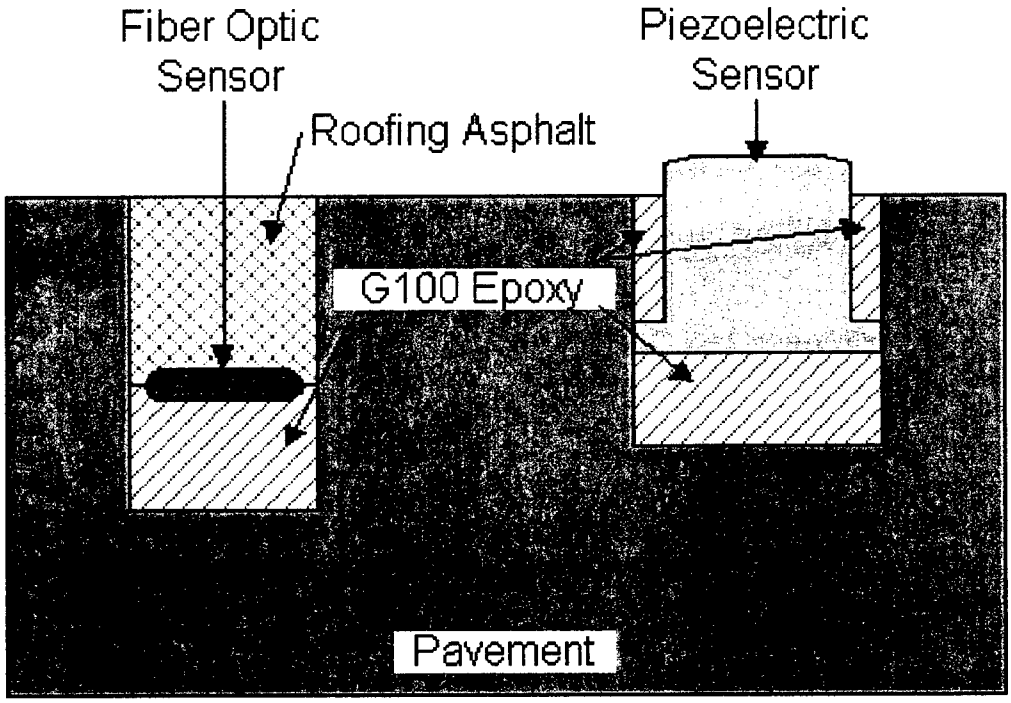

Figure 5.1. Cross-section of a Fiber-Optic Sensor and a Piezoelectric Sensor in the Pavement

5.1.1 Materials Used in the Field Installation

As with the piezoelectric sensor, the fiber-optic sensor is epoxied into a groove with G-100. This material is an epoxy/sand mixture with a one hour cure time. For the fiber-optic sensor, this epoxy forms a consistent, solid and level base. Type III Steep (ASTM D312-89) roofing asphalt is heated and poured into the groove to cover the sensor. This material was chosen because its elastic properties allow load to be transferred to the sensor and it can easily be cut level with the surface of the pavement after it solidifies. The roofing asphalt hardens quickly after placement allowing the reopening of the roadways.

The complete procedure followed for installation of fiber-optic sensor into a pavement is presented in Appendix E.

5.1.2 ARL Sensor Field Installation

Field installations of the fiber-optic microbend sensor were conducted at Florida Tech's Applied Research Laboratory, the access road to CSR Rinker's Palm Bay Ready-mix Plant, and the access road to Mac Asphalt's Melbourne Hot-mix Asphalt Plant. A total of six sensors were installed, with one placed in the flexible pavement at the ARL Building, three placed in Rinker's concrete pavement and two placed in Mac Asphalt's flexible pavement. All six sensors were 6-feet (1.8 m) in length.

Microbend sensor ARL 1 was installed at the Florida Tech's Applied Research Laboratory (Figure 5.2) in Melbourne, Florida, on October 22, 1996, using the procedure outline in Appendix F. The desired depth to the top of the sensor was 1/4 inch (0.64 cm).

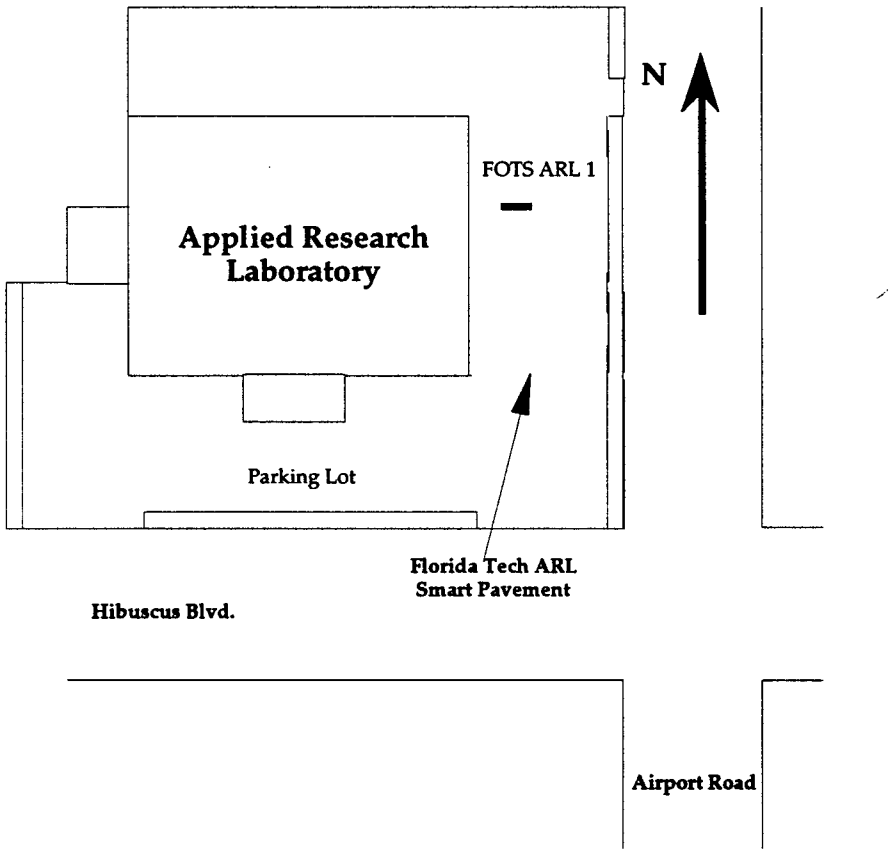

Figure 5.2. Location of Fiber-Optic Sensor in the ARL Parking Lot

Figure 5.3 shows the test site after installation of the fiber-optic sensor. The sensor was placed under the black strip of roofing asphalt and white cross marks (10 inches (25 cm) apart) along its path were used for field testing.

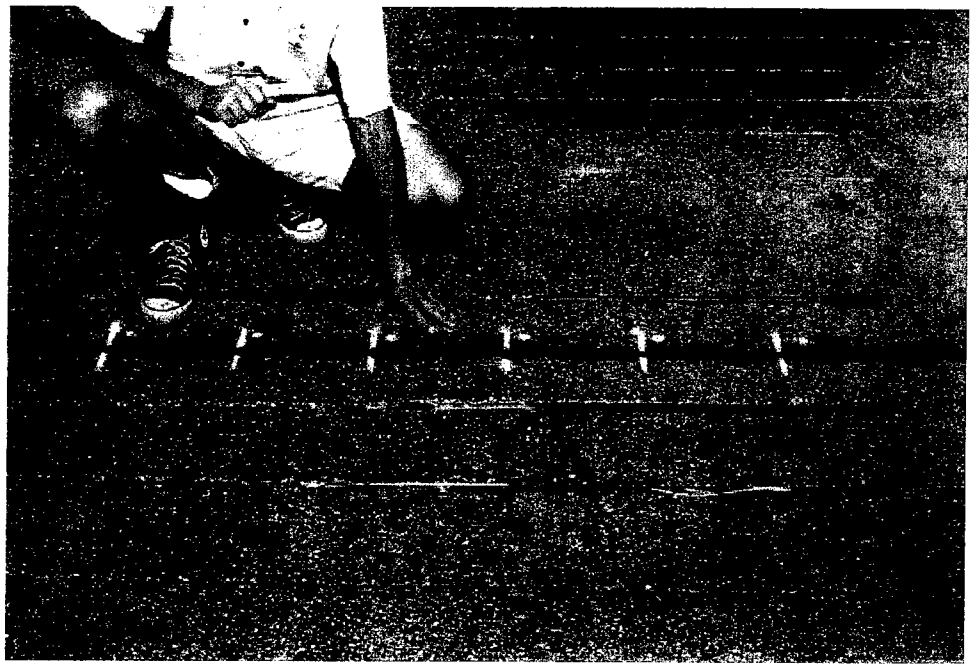

Figure 5.3. Photograph of the Pavement Surface After the Installation of Microbend Sensor ARL 1 at 1/4-Inch Depth

5.1.3 Field Characteristics of a Fiber-Optic Sensor in the Field

Several measurements were made during and after the installation of the microbend sensor ARL 1 to properly analyze the field data. The depth from the surface of the pavement to the top of the sensor, prior to placing the hot asphalt filler material was measured to $\pm$0.01 inch (0.25 mm). The profile change along the length of the asphalt filler after placement and curing was measured to the same accuracy and the profile of the pavement surface on both sides of the sensor was measured. Figure 5.4 presents the surface profile of the pavement and filler material.

The surface profile scale shows that there was less than 1/10-inch (2.5 mm) height variation along the sensor's length. The profile of the asphalt surface did not match the pavement profile exactly, but followed the trend in average height. The asphalt profile was also smoother than the pavement, showing how proper installation with an asphalt filler gives it the average of the surfaces it is between.

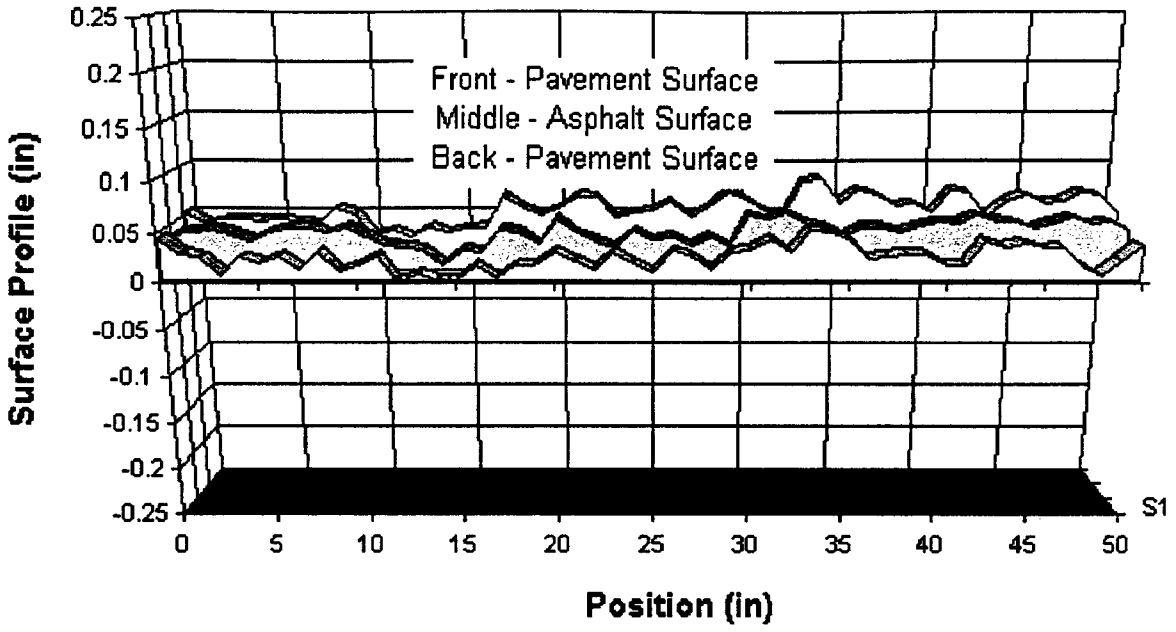

Figure 5.4. Surface Profile of the Pavement and Sensor Filler Material at the Field Site (1 inch = 2.54 cm)

5.1.3.1 Customized LabVIEW Field Data Acquisition Software

The information obtained from a fiber-optic sensor for traffic classification and WIM requires that the waveform resulting from passage of a tire be analyzed, after it was captured and stored. A portable data acquisition system was developed for use with the fiber-optic sensors. Using National Instruments LabVIEW software, several virtual instruments (VIs) were developed. One was designed to acquire waveforms and store them for future analysis (multiple waveform acquisition) while the other was designed to open the data file created by the multiple waveform acquisition and allow the user to selectively zoom in and out on sections of each waveform and write them to an output file. A brief description of both VIs are discussed in Appendix G.

5.1.3.2 Field Waveforms

On November 20, 1996, the multiple waveform acquisition VI was used to capture signals from a FHWA Class 2 Dodge Colt, Class 2 Mercedes Benz, Class 2 Jeep Cherokee, and Class 5 Mack garbage truck traveling over the microbend sensor ARL 1. Multiple passes at various speeds were made with each vehicle. Figures 5.5 through 5.8 show sample waveforms from each of these vehicles. Each figure depicts the change in light intensity, converted to volts, for one-half axle of the vehicle. As the

front axle contacted the sensor the light intensity decreased and the opto-electronic interface would convert this decrease to voltage. LabVIEW software stored the data and depicted the raw waveforms on the laptop computer screen. Comparing the magnitude and duration of the signals indicated the magnitude of the intensity changes was smallest for the lightest vehicle, the Colt and it increased with each increase in vehicle weight. The duration of the load was significantly longer for the Mack truck than for any of the automobiles. Although exact speeds were not recorded, vehicles averaged 15 mph (24 km/hr), therefore, the longer truck tire signal depicts a larger tire and contact length than auto tires.

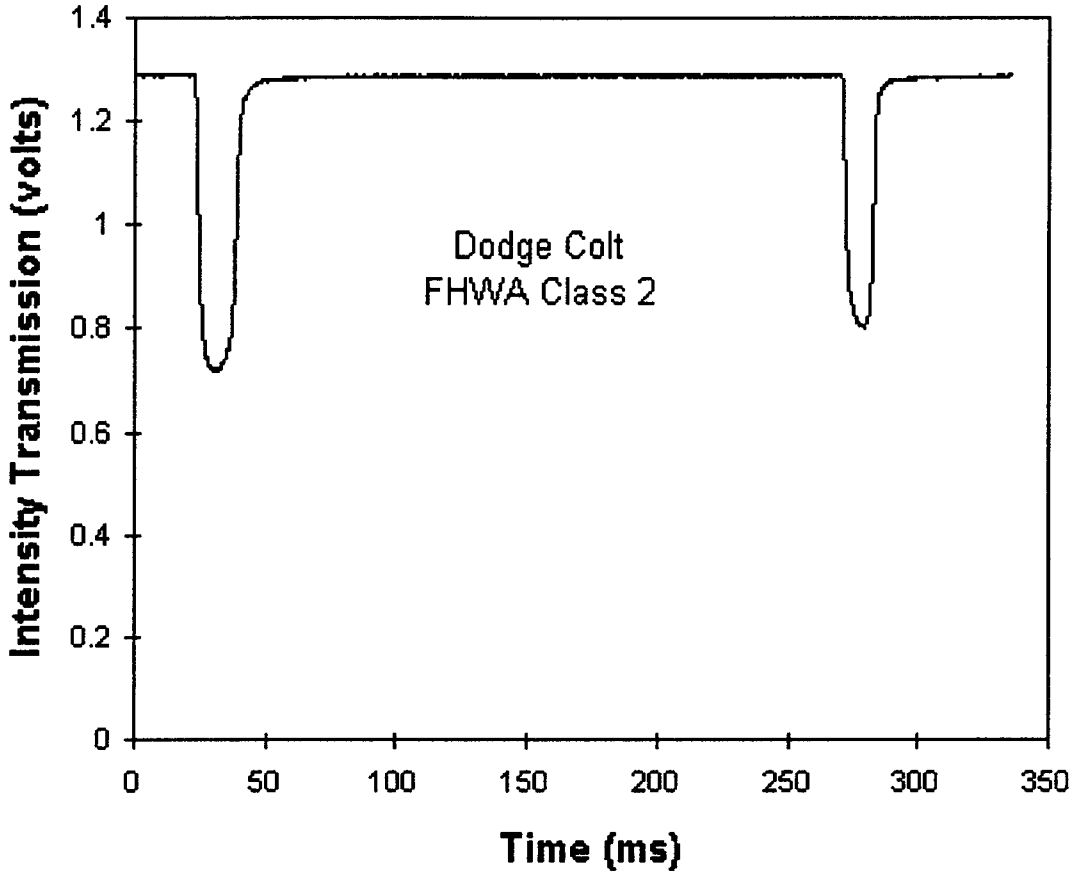

Figure 5.5. Waveforms from a Class 2 Dodge Colt at the ARL

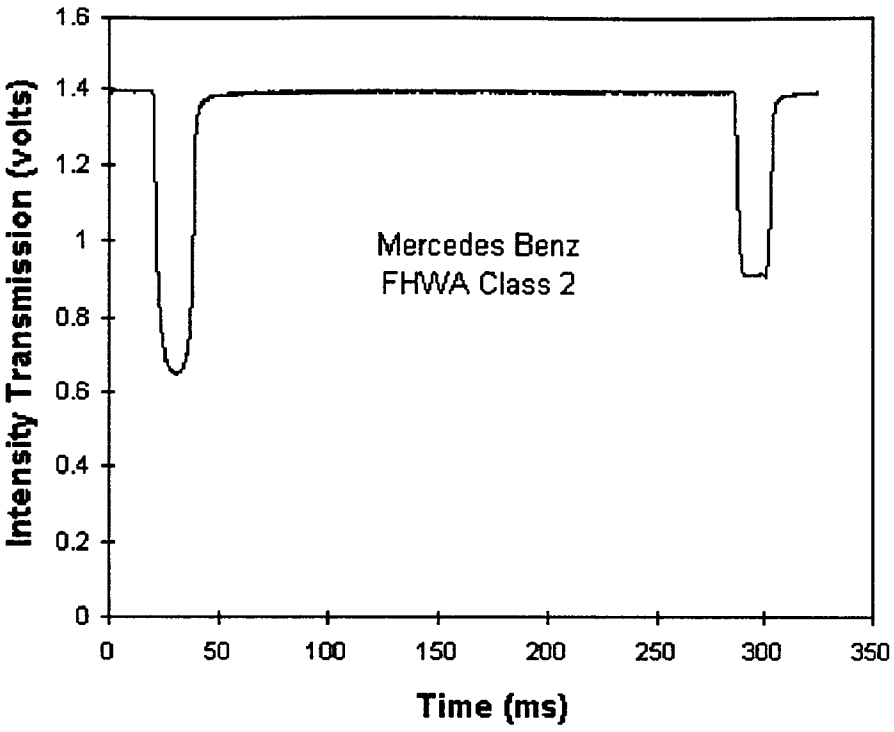

Figure 5.6. Waveforms from a Class 2 Mercedes Benz at the ARL

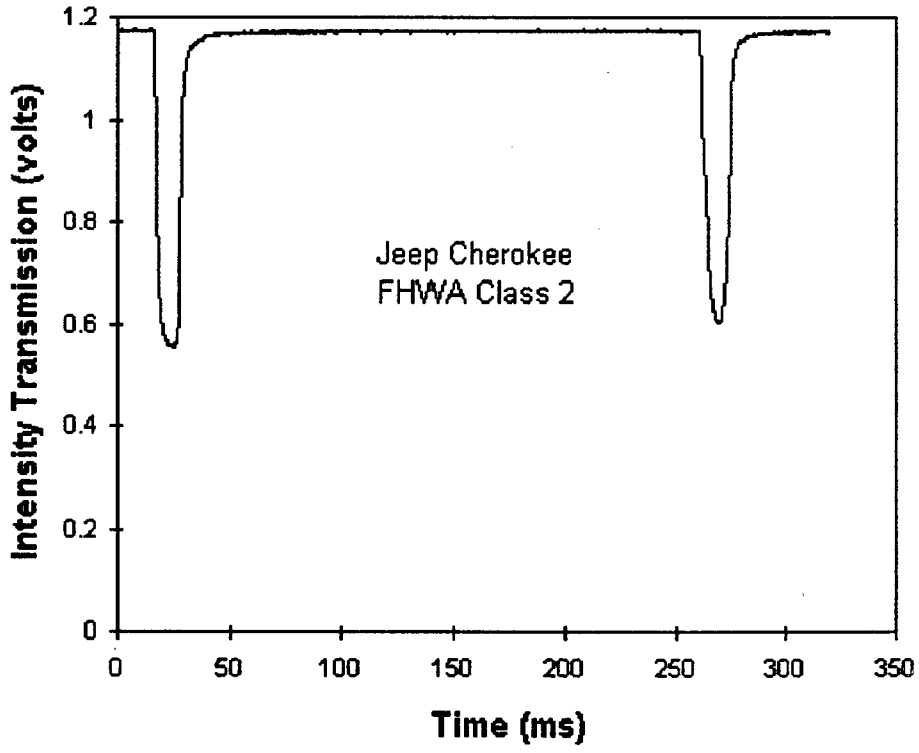

Figure 5.7. Waveforms from a Class 2 Jeep Cherokee at the ARL

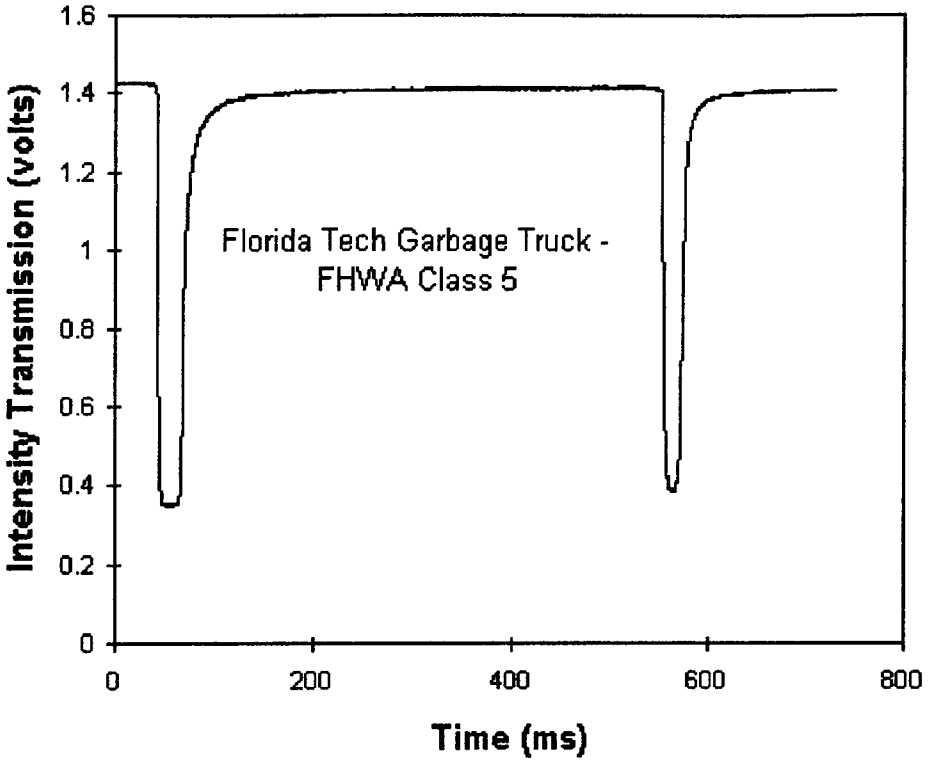

Figure 5.8. Waveforms from a Class 5 Garbage Truck at the ARL

5.2 USE OF FIBER-OPTIC SENSORS FOR TRAFFIC CLASSIFICATION

Traffic classification is performed by an off-the-shelf traffic computer that uses inputs from a series of sensors to place a vehicle into a particular FHWA category. A configuration often used by traffic computers includes a switched input with two on/off piezoelectric sensors placed a known distance (D) apart in the same lane to give the traffic computer waveforms for vehicle classification (Figure 5.9).

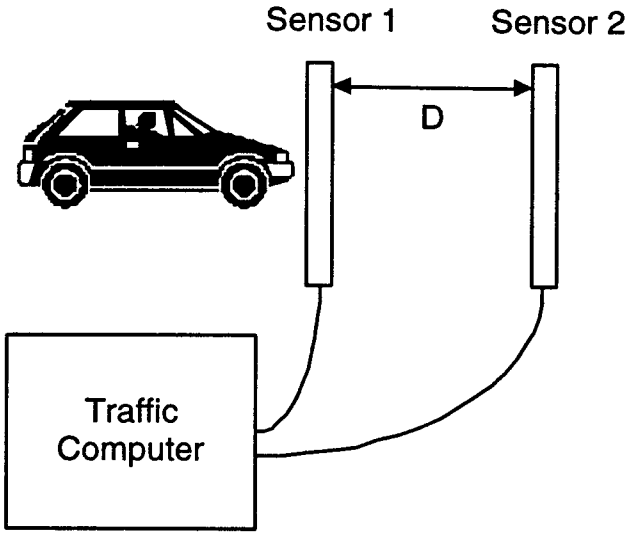

Figure 5.9. Switched On/Off Sensor Layout for Vehicle Classification

With an opto-electronics interface, the output of the fiber-optic traffic sensor used in this research triggers the switched input used by an off-the-shelf traffic computer to perform vehicle detection and classification. This interface serves several functions, it contains as LED light source that is focused into the fiber core and the proper electronics to convert light intensity to voltage. The opto-electronics interface recognizes a change in the received intensity from the fiber-optic sensor and then electronically triggers the traffic computer, allowing it to perform the data storage and classification.

To account for signal noise and fluctuation, a threshold change in intensity was incorporated into the opto-electronic box. Figure 5.10 shows that the unloaded sensor signal, Vn, is equivalent to about 1.3 volts. If 90% of this value is used to activate the on/off switch in the traffic classifying computers, then the waveform shown would start the classification process; however, if 50% is used no classification will occur.

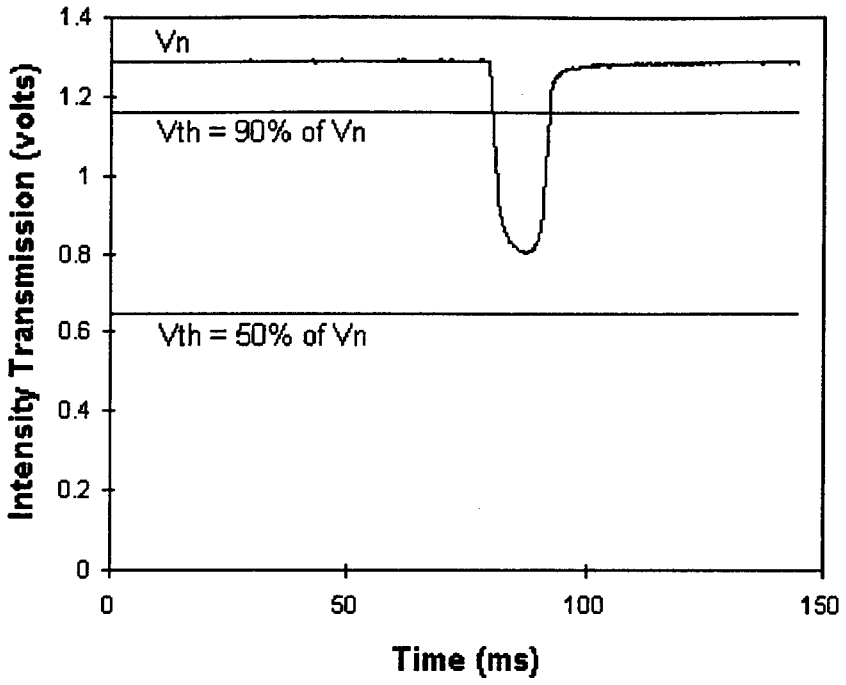

Figure 5.10. Waveform From a Single Axle of a Vehicle Passing Over an Installed Fiber-Optic Sensor

Table 5.1 lists 70 intensity losses for the four vehicles used in the field test of microbend sensor ARL 1. Only two of the waveforms from the rear axle of the Dodge Colt were undetectable for a threshold change of 95% of Vn (trials 2 and 8). This data indicates that sensor ARL 1 would classify over 97% of the vehicles. This classification rate is considered low for highway use, but acceptable for sensors on the pavement at the ARL parking lot. This pavement is fairly rough and there are numerous sensors embedded in various configurations in the 1 1/2-inch (3.8 cm) thick asphalt's concrete. There is a high probability that the two missing readings occurred as a tire bounced over the sensor due to the roughness of the surface.

Table 5.1. Intensity Loss from All Waveforms Acquired at ARL Field Site

	Colt		Benz		Jeep		Garbage Truck	
Trial	Front	Rear	Front	Rear	Front	Rear	Front	Rear
1	44%	38%	53%	49%	53%	35%	75%	73%
2	40%	0%	69%	68%	41%	46%	84%	84%
3	55%	46%	45%	42%	40%	41%	85%	84%
4	35%	37%	51%	61%	45%	58%	87%	87%
5	41%	47%	59%	54%	52%	40%	75%	75%
6	46%	45%	58%	54%	43%	59%		
7	49%	34%	50%	59%	59%	48%		
8	54%	0%			42%	41%		
9	60%	46%			51%	58%		
10	53%	40%			61%	46%		
11	53%	44%			57%	53%		
12					65%	58%		

5.3 USE OF FIBER-OPTIC SENSORS FOR WIM

Weigh-in-motion (WIM) is the measurement of the dynamic load of a vehicle from a sensor in the pathway of the vehicle. Common today is the use of piezoelectric sensors for WIM. These sensors consist of a thin ceramic that has an electrical charge. The dynamic force of a tire passing over the sensor produces a corresponding output voltage change from the piezoelectric material. To determine the load on the tire, the area under the voltage waveform is calculated and multiplied by a calibration factor. The calibration factor is determined by using vehicles with known tire or axle loads. The vehicles repeatedly pass over the WIM sensor(s) at different speeds so loads can be plotted versus their corresponding areas. With this plot, a curve fit can be applied to the data and the resulting relationship used as a calibration for the sensor to determine the weight of the vehicle. WIM calibrations must be performed on a routine basis due to the changing sensor and pavement properties.

Because of their similarity, the fiber-optic microbend sensor for WIM has been related to the piezoelectric sensor. Outputs from both systems are voltages and have distinct relationships to the tire(s) rolling over them. The derivation of preliminary equations for determining dynamic vehicle weight from the output of a fiber-optic microbend sensor will be presented, followed by an application of the derived methods to data taken at the field site (ARL).

5.3.1 Proposed Equations for Determining Vehicle Weight

Before the equations are presented for determining the vehicle weight, a brief description of the parts of a typical waveform produced from fiber-optic microbend sensor from a tire rolling over it will be included to aide in the discussion. Figure 5.11 shows a typical output waveform.

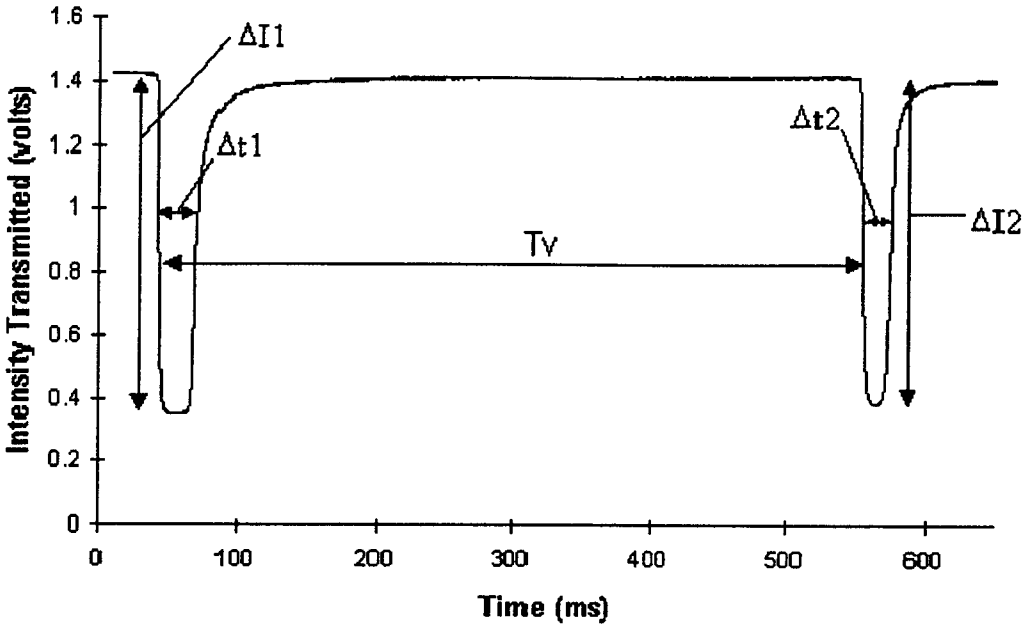

ΔI1 - Intensity Loss, Half Axle 1 Δt1 - Width, Half Axle 1

ΔI2- Intensity Loss, Half Axle 2 Δt2 - Width, Half Axle 2

Tv - Time between axles, which can be used to find the velocity if the wheelbase is known

Figure 5.11. Components of a Typical Output Signal From a Fiber-Optic Sensor

The two main components of the fiber-optic microbend sensor waveform are the intensity loss and the curve width. The intensity loss in the sensor is a function of such things as 1) the width of the tires on the sensor (wt); 2) tire pressure (Pt); 3) width of the groove or sensor (ws); and 4) response of the filler material to tire pressure. The filler material response is a function of thickness and temperature. The curve width is the time the tire contacts the sensor (Δt), which can be multiplied by the velocity of the vehicle to determine tire contact length (lt). Pavement type (i.e., asphalt or concrete), surface roughness, temperature and soil conditions also affect the output signal. These factors make WIM predictions very difficult. Field calibrations are often repeated to ensure that proper vehicle weights can be estimated. For this research, three procedures were developed for WIM estimates. However, only the most promising procedure will be presented. For details on the other two, see Taylor (1996). A significant research effort would have to be undertaken to give highly accurate WIM predictions. This effort is beyond the scope of this research.

5.3.2 Basic Method ARL Predictions

For the most promising method, the Basic Method, an algorithm to calculate the half axle loads was applied using constants based on the particular class of vehicle and the contact length of the tire(s) measured from the sensor output. This method was assumed ideal for research and calibration purposes, because the same vehicles were continually being used during field testing and calibration. The total load on the tire was assumed equal to the tire pressure (P_t) multiplied by the tire contact area.

$$Ft = Pt \cdot wt \cdot lt \qquad (5\text{-}1)$$

Where: (wt • lt) is the tire contact width (wt) times the tire contact length (lt).

For each axle in a particular class of vehicle, the tire pressure and the width of the tire was assumed to be constant. Each of these values were measured for all vehicles used. The contact length of the tire was determined from the waveform pulse width (Figure 5.11) to yield the total load (Ft). With this method, there was no need for calibration for depth because the intensity loss was not used in the equation. The values for tire pressure and tire width for the two classifications of vehicles used in this research are listed in Table 5.2. These values were chosen based on average values of measurements from the vehicles used for testing.

Table 5.2. Average Tire Width and Tire Pressure for Class 2 and Class 5 Vehicles

Vehicle Classification	Tire Pressure (Pt) [lbs/in^2]	Tire Width (wt) [in]
Class 2 Front and Rear Axles	30	6
Class 5 Front Axle	110	12
Class 5 Rear Axle	100	16

Note: 1 psi = 7 kPa, 1 in = 2.54 cm

5.3.3 WIM from ARL Field Site

At noon on November 20, 1996, at Florida Tech's Applied Research Laboratory in Melbourne, FL, data was acquired with the LabVIEW Multiple Waveform Acquisition VI from microbend sensor ARL 1. The four vehicles used for the test were a Class 2 Dodge Colt, Class 2 Mercedes Benz, Class 2 Jeep Cherokee, and Class 5 Mack Garbage Truck, each traveling at speeds between 5 and 25 mph (40 km/hr). Following the field acquisition, the data was taken into the laboratory where a software program written in C++ was used to extract the variables needed by the three methods for computing the dynamic weight.

5.3.4 Basic Method ARL Predictions

Both the Intensity Loss and Current Method algorithms are functions of the intensity loss in the sensor. These methods require complicated field calibrations and analytical modeling. The Basic Method of calculating half axle loads is a function only of the contact length of the tire. The contact length does

vary significantly depending on the axle weight. This fact was documented by the results shown in Figure 5.12.

To calculate the contact length of the tire, the method outlined in Figure 5.12 was applied to each wave-form. At location 1, the tire has not contacted the sensor, so the output voltage is unchanged. As the tire just begins to roll onto the sensor (location 2), the intensity begins to change and the beginning of the tire contact length is measured. At location 3, the sensor is under the center portion of the tire. During this, the intensity falls a maximum value. At location 4, the back edge of the tire begins to leave the sensor, and the intensity begins to return to its no-load level. This is the other end of the contact length. Therefore, the total contact length is the time it takes to go from locations 2 to 4, multiplied by the velocity in in/sec to get the length in inches.

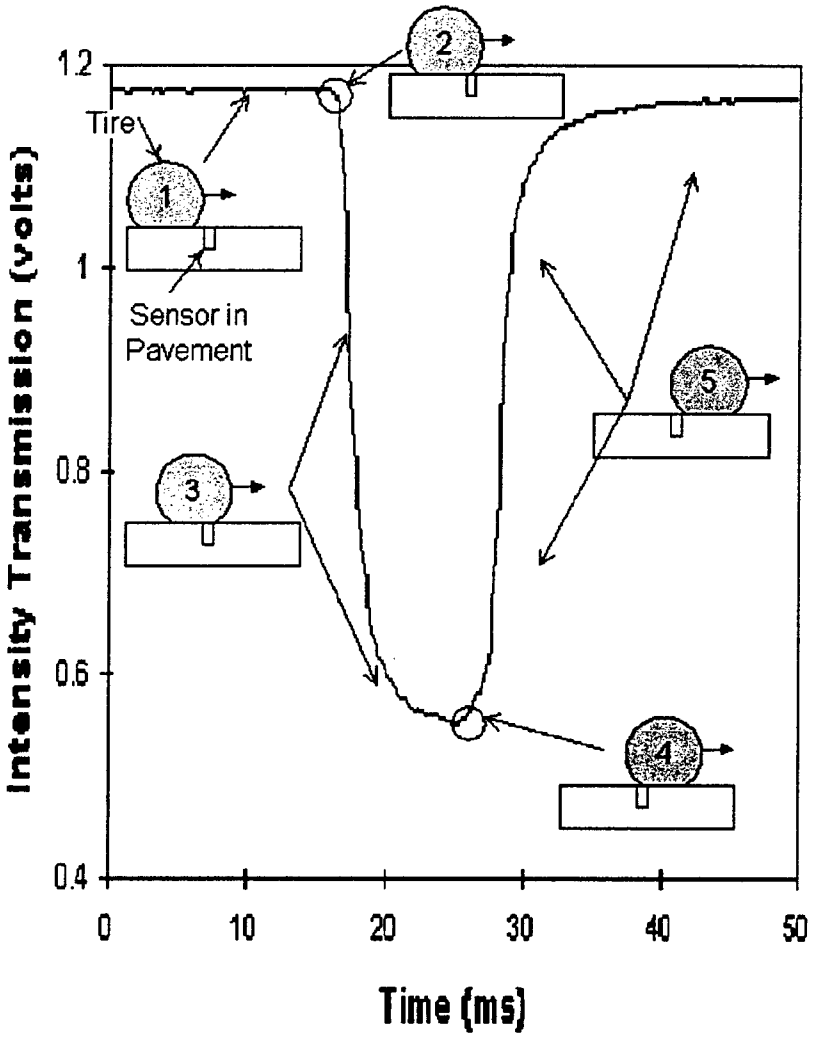

Figure 5.12. Determining the Contact Length of a Tire from the Microbend Sensor Output

The calculated contact length for each half axle tire(s) is presented in Table 5.3. The variation among the lengths for each vehicle averages about 5% with a maximum of 15% for the rear axle of the Dodge Colt and a minimum of 4% for the front axles of the Mercedes Benz and Mack Truck.

Table 5.3. Contact Lengths From Field Data

	Colt		Benz		Jeep		Garbage Truck	
Trial	Front	Rear	Front	Rear	Front	Rear	Front	Rear
1	4.86	3.98	4.23	4.23	5.76	5.83	7.70	5.36
2	3.89	2.24	4.34	3.99	5.83	5.83	8.25	6.10
3	5.10	4.04	4.39	4.86	6.29	5.01	7.52	5.80
4	5.36	4.17	3.94	4.48	6.36	5.15	7.80	4.90
5	4.73	3.52	4.01	4.53	6.36	5.47	8.01	5.44
6	4.77	4.34	4.10	4.17	6.69	6.11		
7	4.46	3.75	4.03	4.16	6.07	5.31		
8	4.76	4.05			4.82	3.44		
9	4.37	3.96			5.80	5.01		
10	4.91	4.25			5.43	5.98		
11					6.38	5.79		
12					6.35	6.00		

Use of these lengths in Equation (5-1) along with the tire pressure and tire widths specified in Table 5.2, yields the dynamic half axle loads in Figure 5.13. The predictions obtained from this method are the best of the three methods. Calculation of the half axle loads included no correction factors.

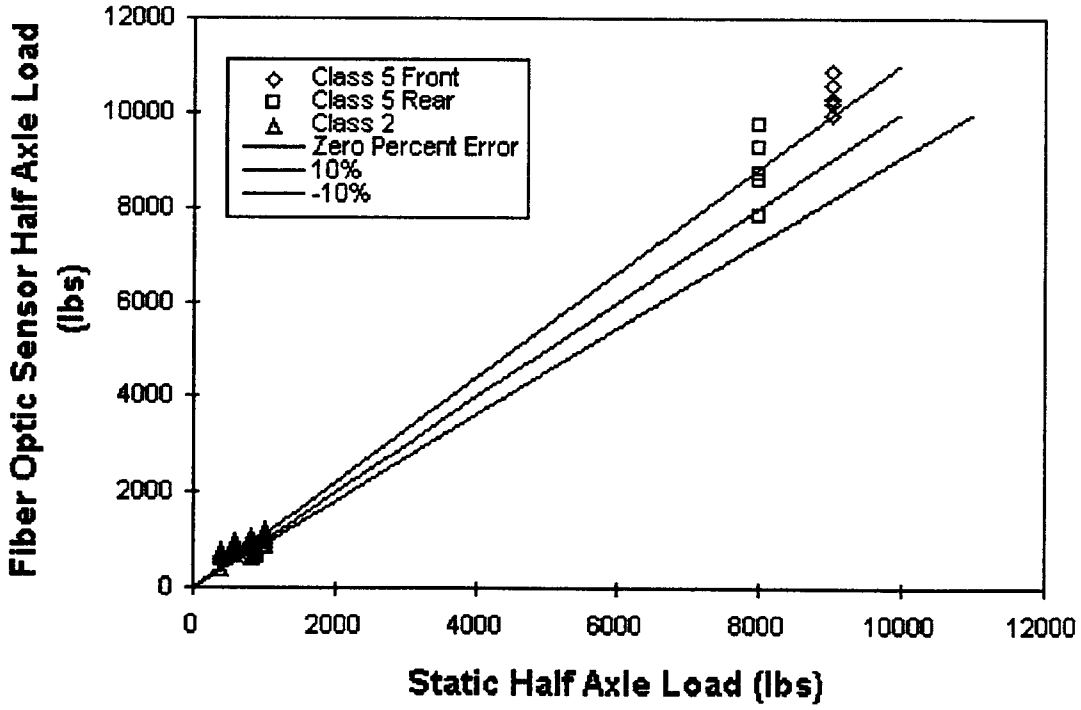

Figure 5.13. WIM Predictions for Basic Method of Calculating Dynamic Weights

5.4 INSTALLATION AND DATA ANALYSIS FROM SENSORS IN RIGID PAVEMENT

5.4.1 Introduction

Three fiber-optic traffic sensors were installed at depths of 0.85, 0.5 and 0.3 inches (2.2, 1.3, 0.8 cm) below the surface in the concrete pavement access road to the Rinker Corporation concrete mix plant in Palm Bay, Florida (Figures 5.14 and 5.15). This 6-inch (15 cm) thick pavement is subjected primarily to loaded and unloaded Class 6 concrete truck traffic. The site is located two miles south of Melbourne, Florida, on the west side of U.S. Route 1. This summary presents the site layout and the data. The purpose of the field testing was to subject the sensors to high axle loads and monitor the sensor performance with respect to the number of cycles.

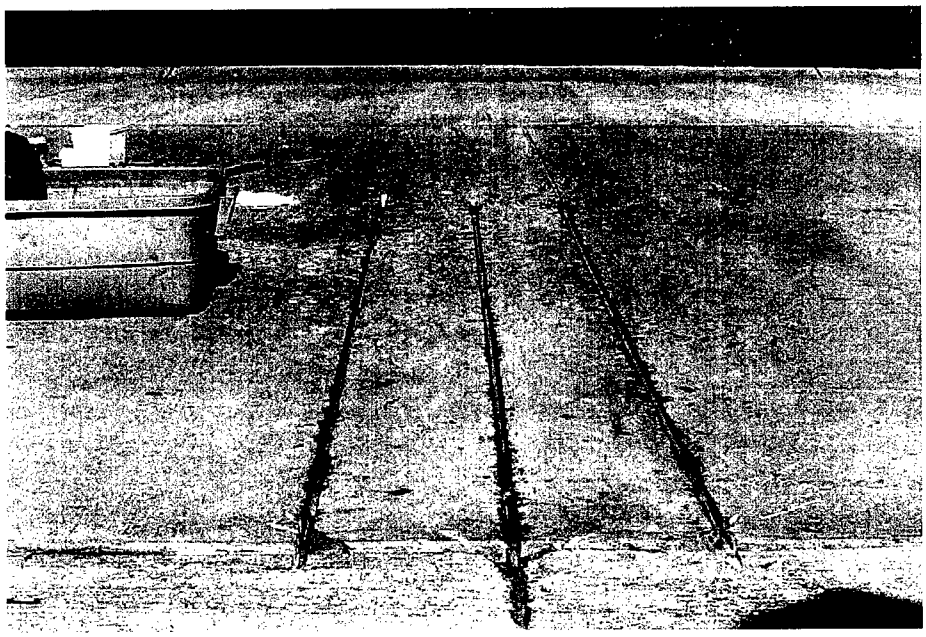

Figure 5.14. Photograph of Sensors During Placement into Rigid Pavement Grooves . Sensors Placed at 0.30, 0.50 and 0.85 inches (2.2, 1.3, 0.8 cm) from Surface from Right to Left

Figure 5.15. Photograph Depicting Sensors being Covered with Hot Roofing Asphalt

5.4.2 Background

In November/December 1996, a batch of 10 sensors was fabricated in the Florida Tech Smart Sensor laboratories at the Applied Research Laboratory (ARL). Three of these sensors, Nos. 7, 8, and 10, were installed in the access road. Sensor number 10 was installed in the western most groove at a depth of 0.85-inch (2.2 cm), sensor number 7 was installed in the eastern most groove at a depth of 0.3-inch (0.8 cm) and sensor number 8 was installed in central groove at a depth of 0.5-inch (1.3 cm) (Figure 5.16).

Prior to installation, a series of laboratory calibration tests were performed. Static load versus intensity tests yielded curves typical to those previously observed from these types of microbend sensors. Figure 5.17 shows the static loading response for sensors 7, 8 and 10. The average load at 50% light loss, based on tests at four locations along the length of the sensors, are 8.1, 7.0 and 5.4 pounds (3.7, 3.2, and 2.4 kgs) of compression on a two inch platen. These values indicate a decrease in transmitted light intensity of 50%. The load at the 50% light loss level was chosen for comparison purposes to allow quantification of relative sensitivities of various microbend sensors. Also included are the results from a dynamic compression testing procedure that was developed by pulling a cart over the entire length of a 6-foot (1.8 m) long sensor. The weight of the cart loaded with four pounds (1.8 kgs) was transferred to the sensor through a plastic wheel (Figure 4.4). This test provided continuous intensity loss data along the length of the sensor. The raw intensity signals were averaged over an 8-inch (20 cm) length to simulate the signal that a standard truck tire would yield. Figures 5.18, 5.19, and 5.20 show the results for the averaged signals from the dynamic cart testing for sensors 7, 8 and 10. Table 5.4 shows the average intensity lass and range of intensities. The normalized intensity losses ranged from 10 to 30 percent and averaged about 20 percent. Taylor (1997) conducted a series of these tests on sensors six feet in length to determine the tests repeatability. This data, summarized in Table 5.5, indicates that there is very little variation from test to test. The mean loss in light intensity was 44% with a standard deviation of 8%. For the three sensors placed in the concrete pavement there is relatively good sensor-to-sensor correlation. The largest variation is about 20% over the length of the sensors.

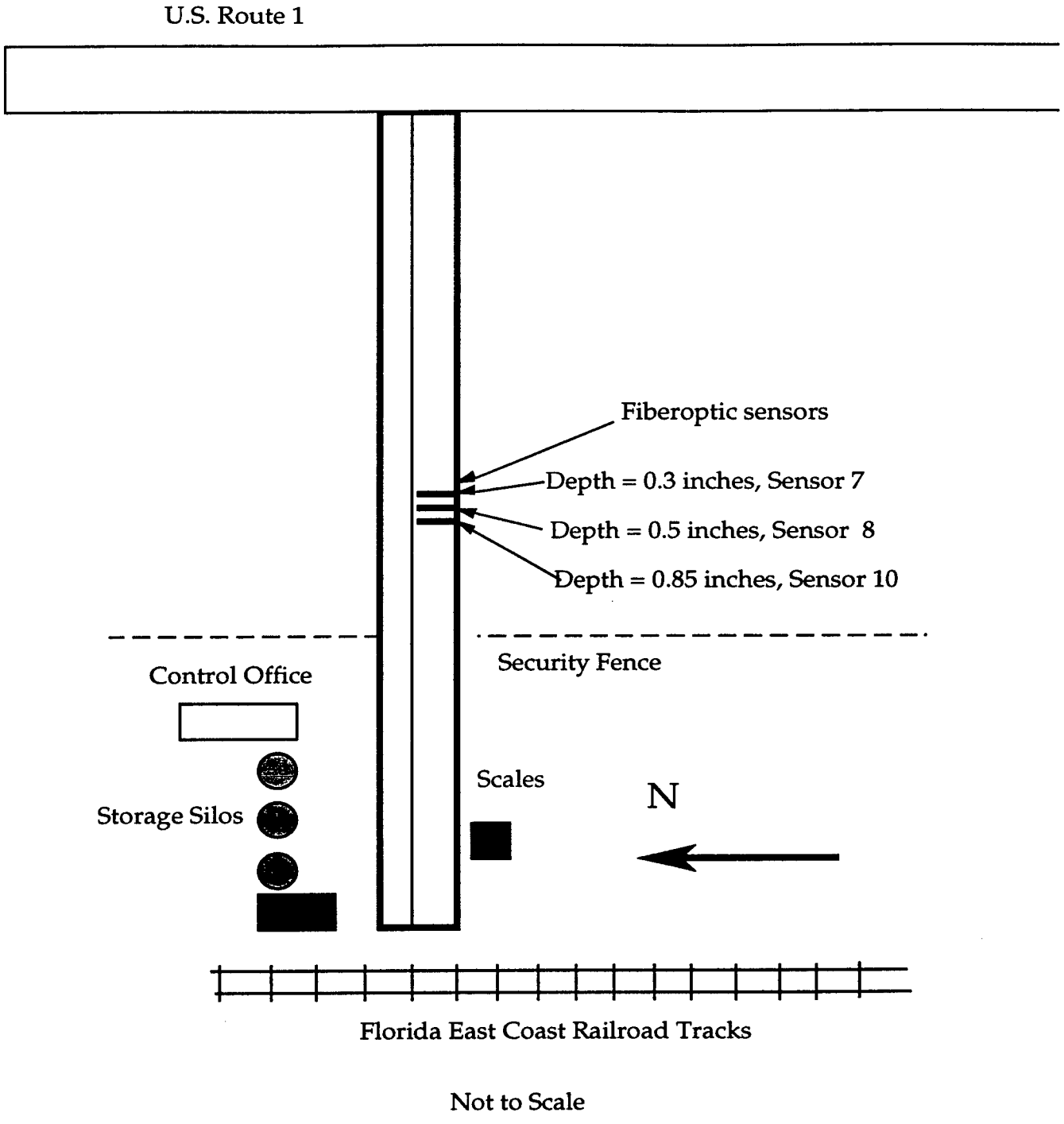

Figure 5.16. Location of Three Fiber-Optic Sensors within CSR Rinker Corporation's Ready Mix Concrete Plant, Palm Bay, Florida

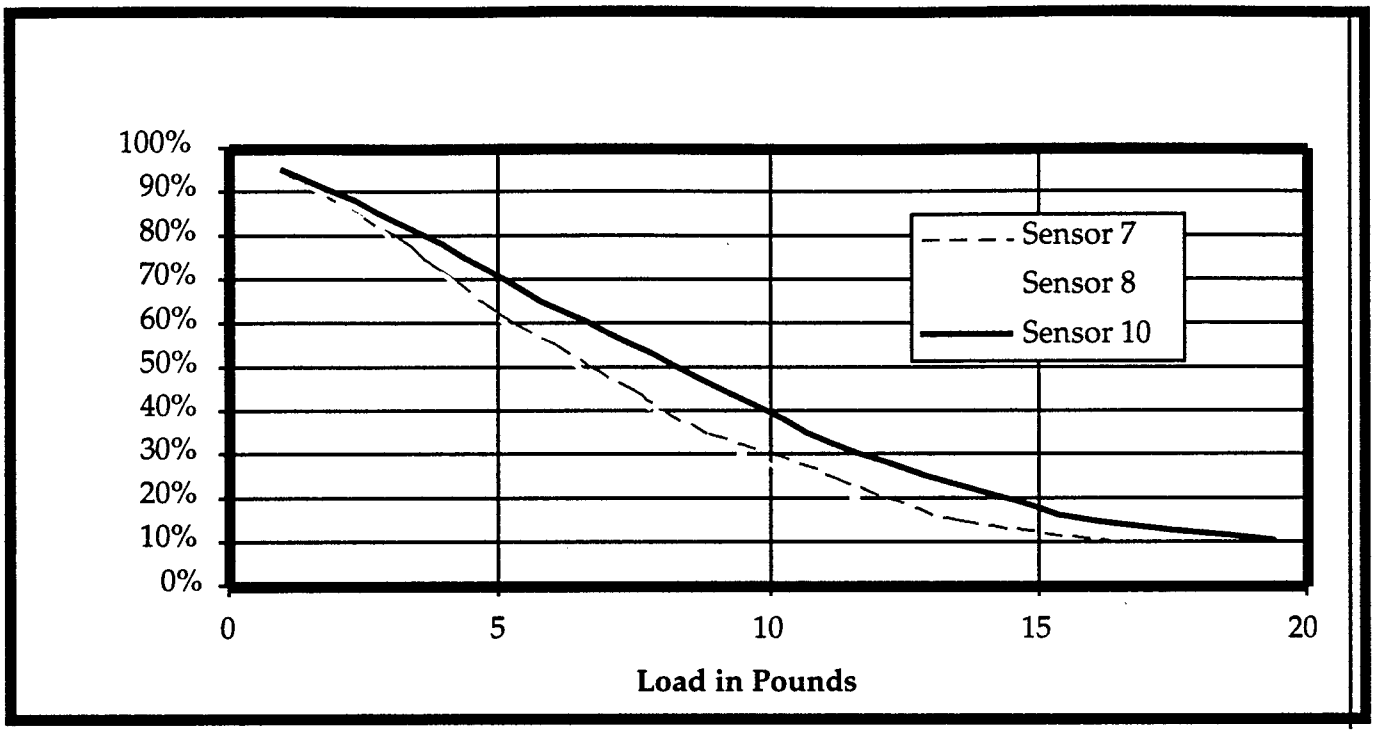

Figure 5.17. Static Calibration Response for Sensors 7, 8, and 10

Table 5.4. Variation for an 8-inch Truck Tire Width for Sensors 7, 8, and 10 from Dynamic Cart Testing

Sensor Number	Average Intensity Loss (%)	Range of Intensities (%)
7	26	20 -- 32
8	20	10 -- 30
10	18	12 -- 23

Table 5.5. Test to Test Variation for a Single Sensor from the Dynamic Cart Testing (From Taylor, 1997)

Test Number	Average Intensity Loss (%)	Standard Deviation (%)
1	44.3	7.9
2	44.9	8
3	43.5	7.9
4	42.9	8

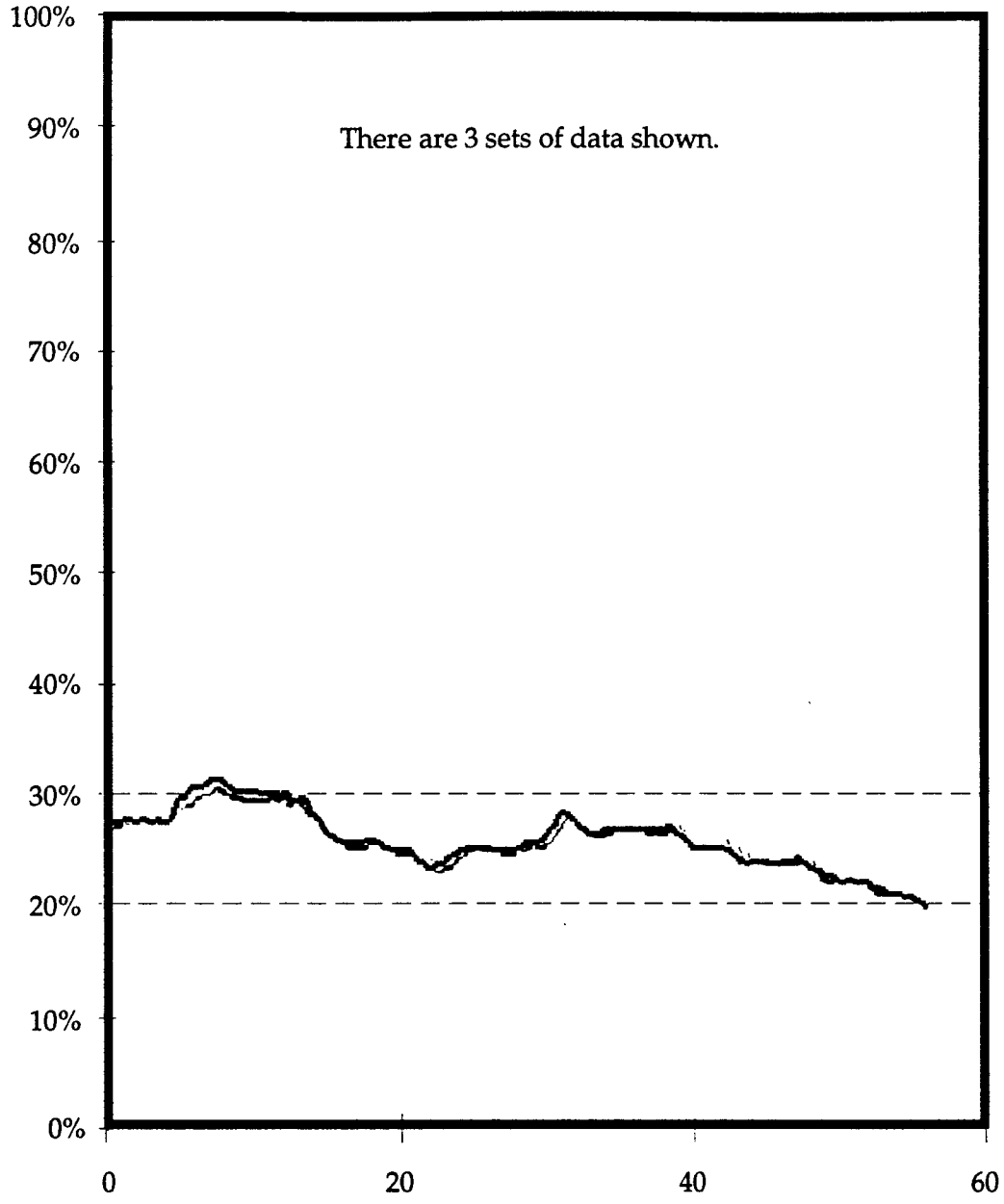

Figure 5.18. Continuous Intensity Data From Moving Averages Over 8-inch Lengths for Sensor 7 (1 inch = 2.54 cm)

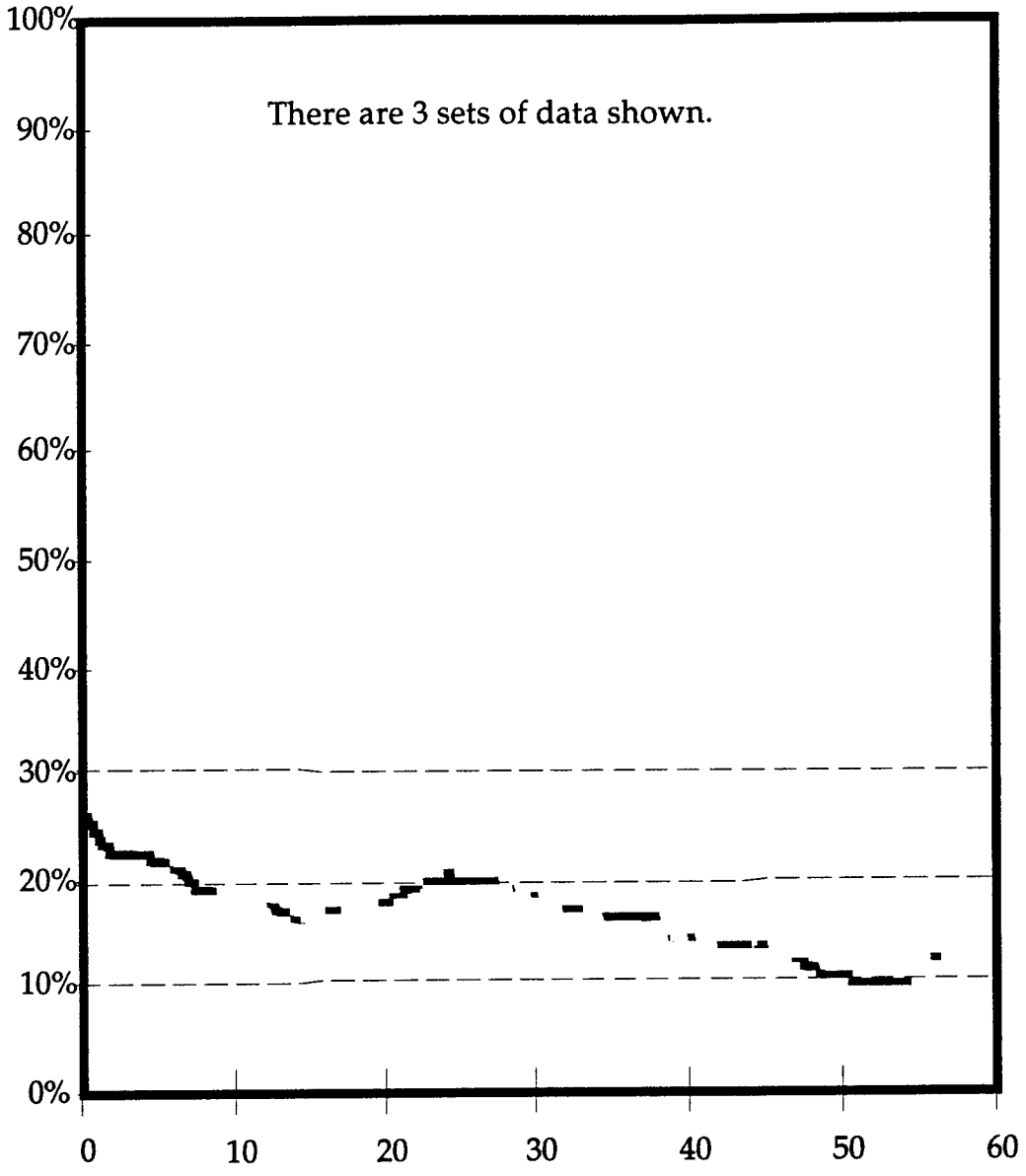

Figure 5.19. Continuous Intensity Data From Moving Averages Over 8-inch Lengths for Sensor 8 (1 inch = 2.54 cm)

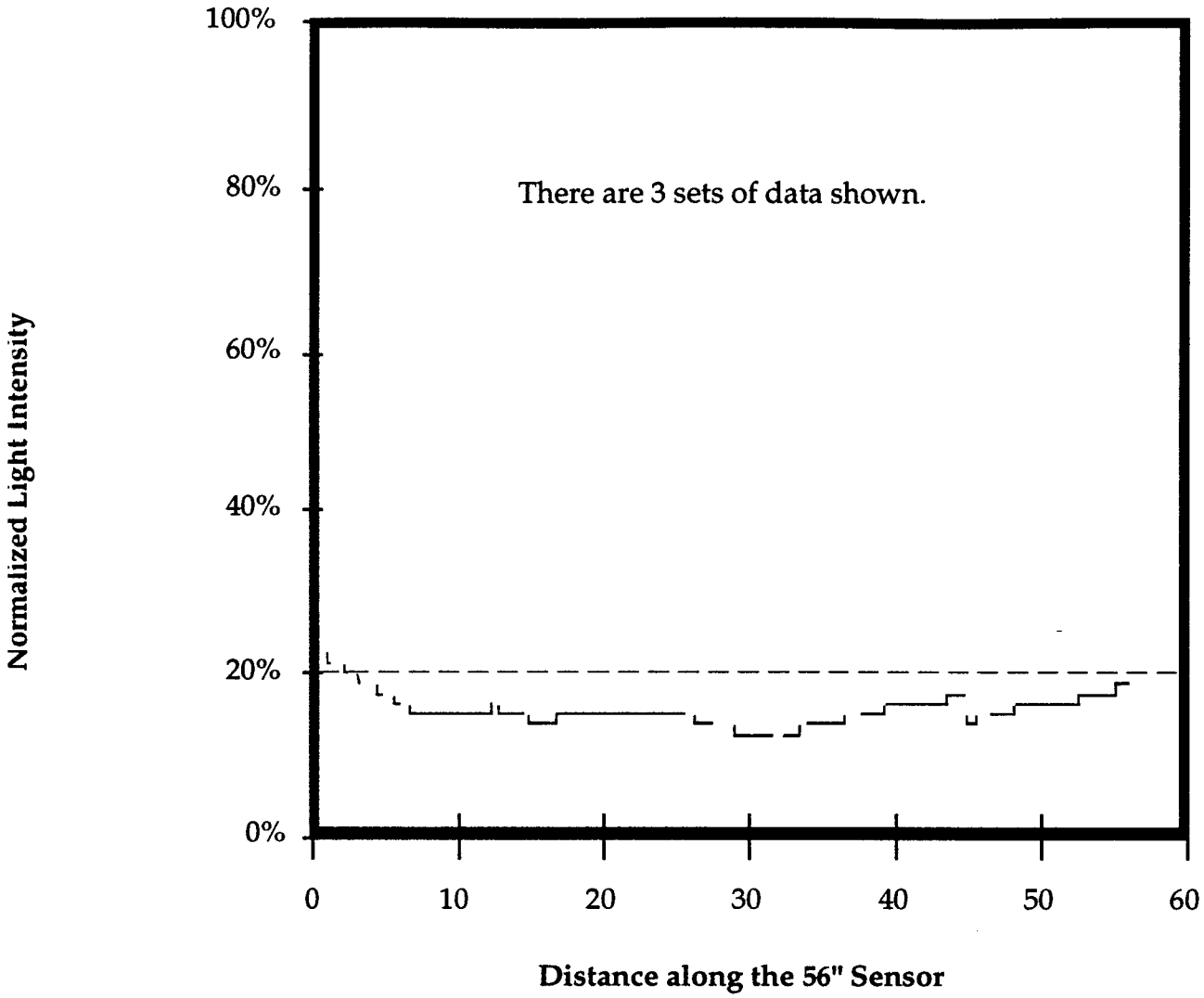

Figure 5.20. Continuous Intensity Data from Moving Average Over 8-inch Lengths, Sensor 10

5.4.3 Field Installation

Field installation techniques were studied for placing sensors in concrete pavements. In late December 1996, three grooves were cut into the rigid pavement by using a street saw with two 0.25-inch (0.6 cm) thick abrasive blades stacked together to obtain a 0.5-inch (1.3 cm) wide groove. The distance between each of the three grooves was 9 inches (23 cm). The approximate depths of cut for the shallow (0.3-inches, 0.8 cm)), medium (0.50-inches, 1.3 cm), and deep (0.85-inches, 2.2 cm) sensors were 0.55, 0.9–1.2 and 1.3– 1.6-inches (1.4, 2.3-3.0, and 3.3-4.1 cm). These depths varied because the saw blade wears during the cutting process. On January 19, 1997 the flexible sensors were installed by placing G-100 epoxy below the sensors and hot Type III asphalt above the sensors. This practice has been used successfully in previous installations of fiberoptic traffic sensors. The installation resulted in three working sensors as shown in Figure 5.14.

5.4.4 Summary

Three sensors were successfully installed into rigid pavement. The test site and equipment yield classification and load data. Approximately 30 fully loaded Class 6 concrete mix trucks passed over the sensors each day.

5.4.5 Relevant Data for Data Reduction

Two types of 10 cubic yard trucks are operated from the concrete plant, International and Peterbilt. Pertinent data for each are summarized below (Table 5.6). This data was obtained by measuring and weighing the specific vehicles described.

Table 5.6. Class 6 Ready Mix Truck Data

Truck Type	Empty Weight	Axle Spacing		Tire Pressure	Tire Widths	
	(lbs)	Front to Rear (in)	1st Rear to 2nd Rear (in)	(psi)	Front (in)	Rear (in)
International Ready Mix Truck	27000	168	53	100	14	8.25 to 8.75
Peterbilt Ready Mix Truck	26500	179.5	52.5	100	14.5 to 15	8.25 to 8.75

5.5 WEIGH-IN-MOTION DATA

A computer program was written in C++ to record the field waveforms from three fiber-optic sensors. The program takes the voltage signals from the opto-electronic interface and displays the signals as shown in Figures 5.21a through 5.21d. The sensor thresholds are input for the minimum and maximum voltage changes. The minimum threshold ensures that no calculations were performed with the software until at least this change in voltage was recorded (e.g., 10% change required before weights are determined). The maximum threshold was used to ensure that the calculations performed at the peak voltage change were not being affected by a saturated signal. In other words that the voltage change was less than 100%.

There are three sensors embedded in the rigid pavement and the half-axle weights are shown for the front and rear dual tandem axle assemblies on 5.21a through 5.21d. A negative sign in front of the weight signifies that the truck was entering the plant while a positive number signifies that the truck was leaving the plant. This notation is helpful in distinguishing between empty and loaded ready-mix trucks, because typically empty trucks are entering the plant while full trucks are leaving the plant.

Three different methods were proposed for determining weights from the fiber-optic signals. They were termed the basic method, the current method and the intensity method (Taylor, 1997). The current and intensity methods required a calibration to be performed in the field. The values associated with these two methods are uncalibrated and were not used. The basic method values were calibrated in the field by measuring tire pressures and widths and using the vehicle speed and tire/sensor contact time to calculate the contact length. Figure 5.22 shows a typical tire footprint on the pavement, with a control length (l_t) and contact width (w_t)

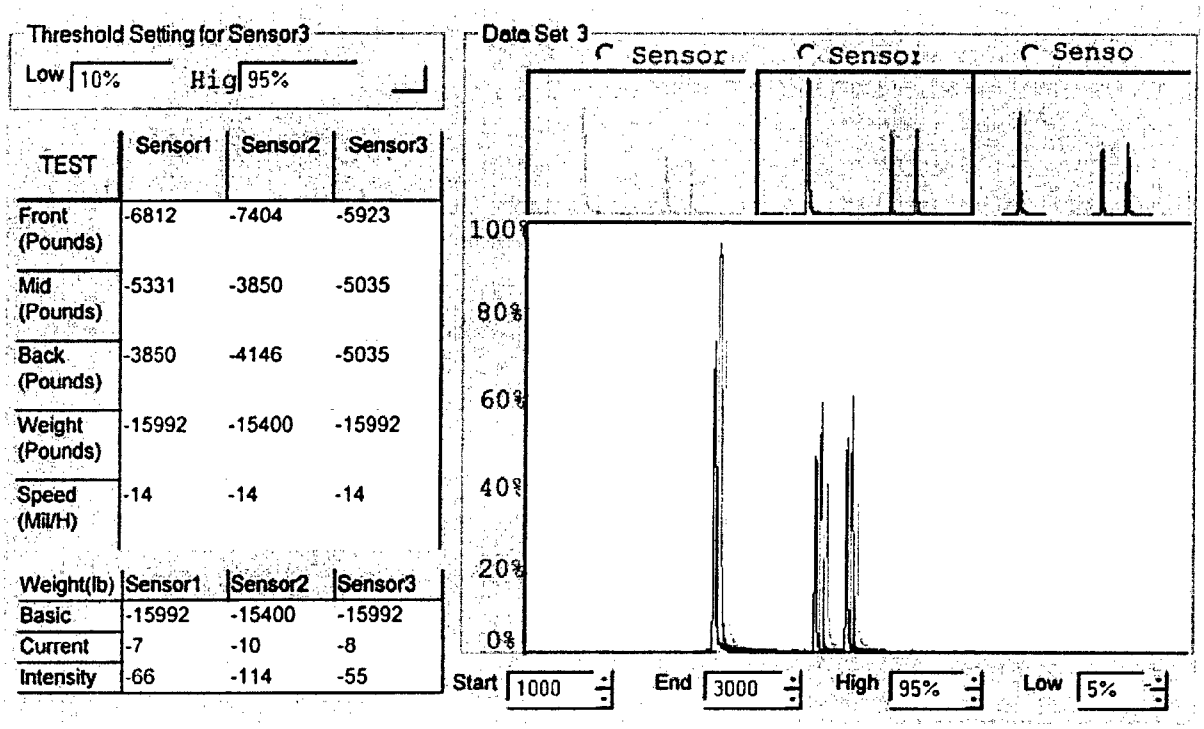

Figure 5.21a. Data Acquisition Software Screen # 1 Displaying Half-Axle Weights from Class 6 Ready-Mix Truck from Sensors 7, 8, and 10 in Rigid Pavement. Note Truck Assumed Loaded

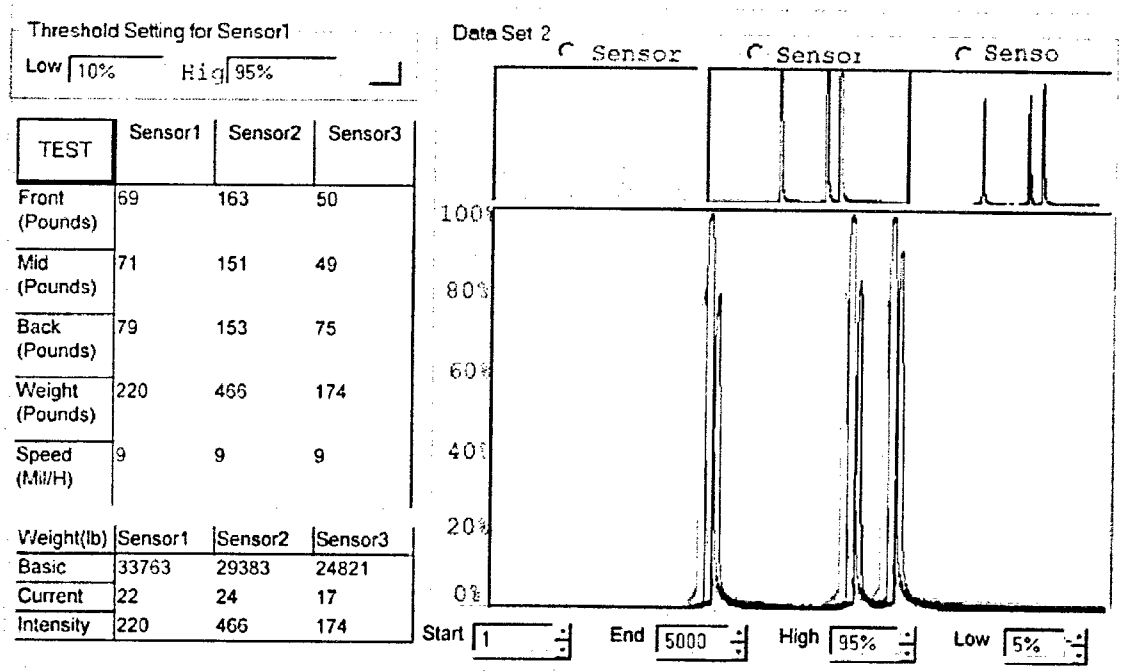

TEST	Sensor1	Sensor2	Sensor3
Front (Pounds)	69	163	50
Mid (Pounds)	71	151	49
Back (Pounds)	79	153	75
Weight (Pounds)	220	466	174
Speed (Mil/H)	9	9	9

Weight(lb)	Sensor1	Sensor2	Sensor3
Basic	33763	29383	24821
Current	22	24	17
Intensity	220	466	174

Figure 5.21b. Data Acquisition Software Screen # 2 Displaying Half-Axle Weights from Class 6 Ready-Mix Truck from Sensors 7, 8, and 10 in Rigid Pavement. Note Truck Assumed Loaded

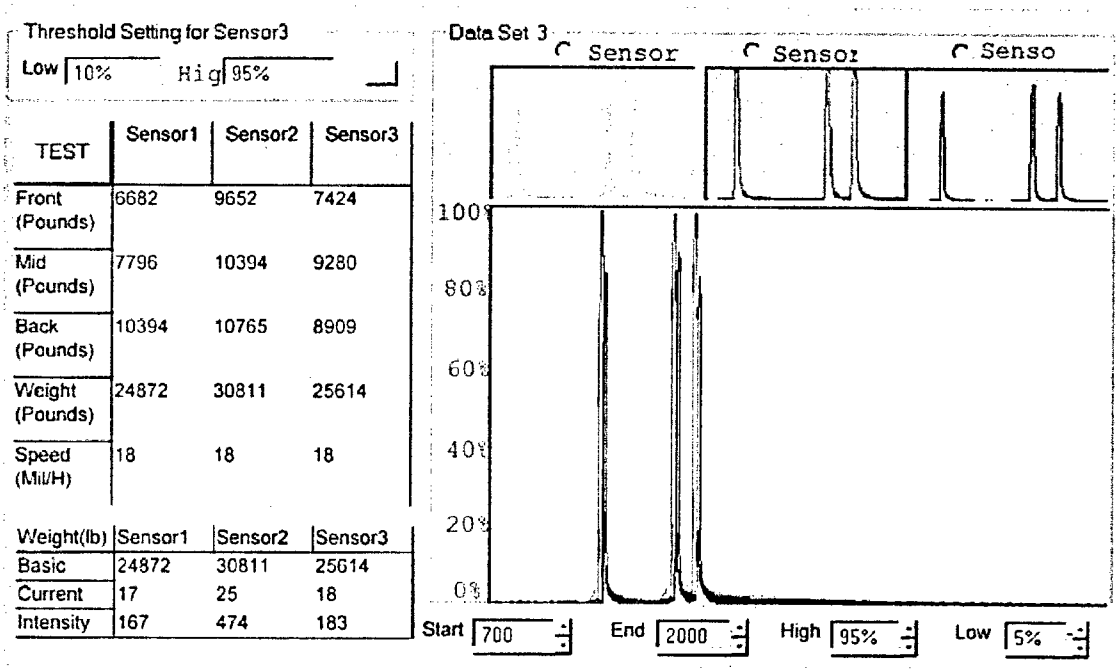

TEST	Sensor1	Sensor2	Sensor3
Front (Pounds)	6682	9652	7424
Mid (Pounds)	7796	10394	9280
Back (Pounds)	10394	10765	8909
Weight (Pounds)	24872	30811	25614
Speed (Mil/H)	18	18	18

Weight(lb)	Sensor1	Sensor2	Sensor3
Basic	24872	30811	25614
Current	17	25	18
Intensity	167	474	183

Figure 5.21c. Data Acquisition Software Screen # 3 Displaying Half-Axle Weights from Class 6 Ready-Mix Truck from Sensors 7, 8, and 10 in Rigid Pavement. Note Truck Assumed Loaded

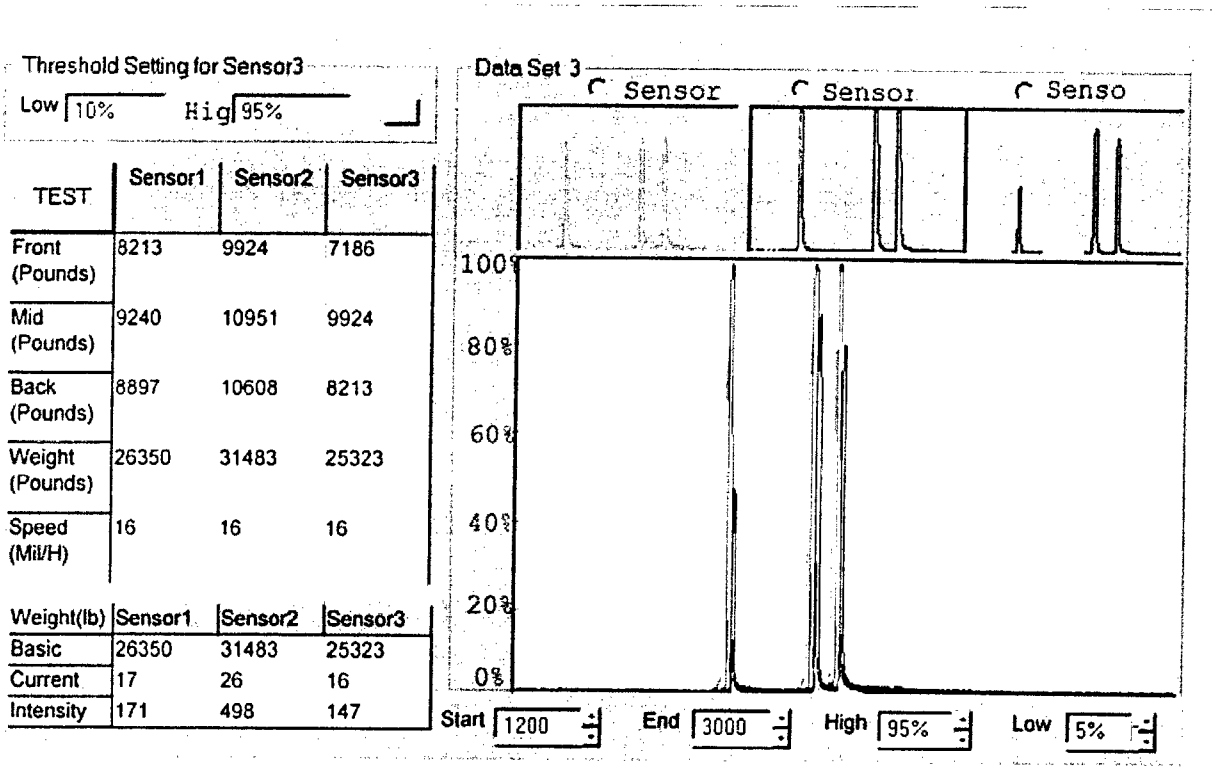

Figure 5.21d. Data Acquisition Software Screen # 4 Displaying Half-Axle Weights from Class 6 Ready-Mix Truck from Sensors 7, 8, and 10 in Rigid Pavement. Note Truck Assumed Loaded

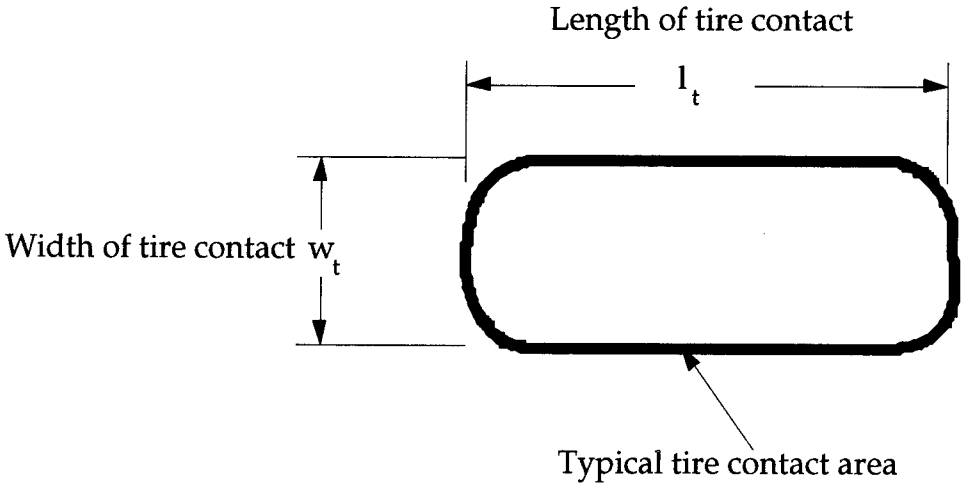

Figure 5.22. Typical Footprint from Tire Contacting Pavement

5.5.1 Rinker WIM Data

Figure 5.21a through 5.21d shows data from four Class 6 ready mix trucks entering and leaving the plant. Table 5.7 summarizes the axle and total weights for the four trucks. Sensors 1, 2 and 3 correspond to sensors 7, 8, and 10 from the batch of 10 sensors that were built in November 1996. Each figure depicts estimated half-axle weights, speed, and the raw waveforms from each of the three sensors. Trucks were assumed empty if they were re-entering the plant and loaded if they were leaving the plant. These assumptions were necessary because actual weights were not available. A full load would have been 10 cubic yards (7.6 m^3), with each cubic yard weighing 3,800 lbs ($1.7x10^3$ kgs). In general, the estimated weights seem reasonable for the trucks. The surface of the rigid pavement is very rough, especially at the joints of the slabs. Field observations of the empty trucks revealed that the rear dual-tandem axle vibrated much more than desired for the data to be considered accurate for WIM.

Table 5.7. Class 6 Ready Mix Truck Fiber-Optic Sensor Weight Estimates

	Sensor 1 Half Axle Weights (lbs)				Sensor 2 Half Axle Weights (lbs)				Sensor 3 Half Axle Weights (lbs)			
Description	Front	Rear 1	Rear 2	Total	Front	Rear 1	Rear 2	Total	Front	Rear 1	Rear 2	Total
Loaded	6682	7796	10394	49744	9652	10394	10765	61622	7424	9280	8909	51226
Loaded	8213	9240	8897	5270	9924	10951	10608	92966	7186	9924	8213	50646
Empty	6812	5331	3850	31986	7404	3850	4146	30800	5923	5035	5035	31986
Empty	5071	5071	2766	25816	8068	5071	4610	35498	5532	4610	5302	30888

Loaded truck weights are assumed to be 57,000 lbs. However, actual plant ticket weights were not obtained.
Unloaded truck weights are assumed to be 29,000 lbs.
Note: 1 lb = 0.4541 kgs

5.5.2 Summary of MacAsphalt WIM Predictions

Two 6 foot long sensors were installed in the flexible pavement driveway leading into MacAsphalt and Florida Mining and Materials Melbourne, Florida. The first sensor was installed May 31 and the second on June 29th 1997. The pavement surface, less than a year old, was constructed using a Superpave mix. Trucks which deliver for these companies are typically Class 6 concrete and asphalt trucks. About 2,000 trucks use this road each month. Weights of both empty and loaded trucks were obtained on numerous occasions over a two month period.

There were differences in the groove width and backfill materials between the Rinker rigid pavement and the MacAsphalt flexible pavement. The Rinker site was comprised of 0.5" grooves backfilled with roofing asphalt. The MacAsphalt site grooves were cut by stacking two 3/16" thick abrasive blades onto the street saw arbor to produce a groove of width 0.375-inch; optimum for a sensor of width 0.3". Type III roofing asphalt was not used in the MacAsphalt installations because of difficulties it caused in obtaining consistent geometric dimensions. Both sensors at MacAsphalt were installed at a depth of 0.3" with a backfill material of Slygard 170. Laboratory studies on this backfill material show it has a compressive elastic modulus of 312 psi which was constant with respect to temperature. This backfill material was bonded to the sensor prior to installation. Once the grooves were cut the sensor/backfill assembly was placed into the groove as one piece.

Weigh-in-Motion data for the concrete ready mix trucks using are presented in Figure 5.23. These trucks were used to allow comparisons to the Rinker data. The linear regression indicates an excellent correlation between measured and predicted weights. The measured weights were obtained by statically weighing an empty class 6 concrete truck and then using the assumption that each cubic yard of concrete weighs 3,800 pounds. Therefore, measured weights of 27500, 35100, 42700 and 65500 pounds, represent ready mix trucks that are empty, carrying 2, 4 and 10 cubic yards. Table 5.8 shows that accurate weights were obtained with this configuration of sensor/backfill groove geometrys for a Type 6 concrete truck, note that the full truck weight was determined within 1%.

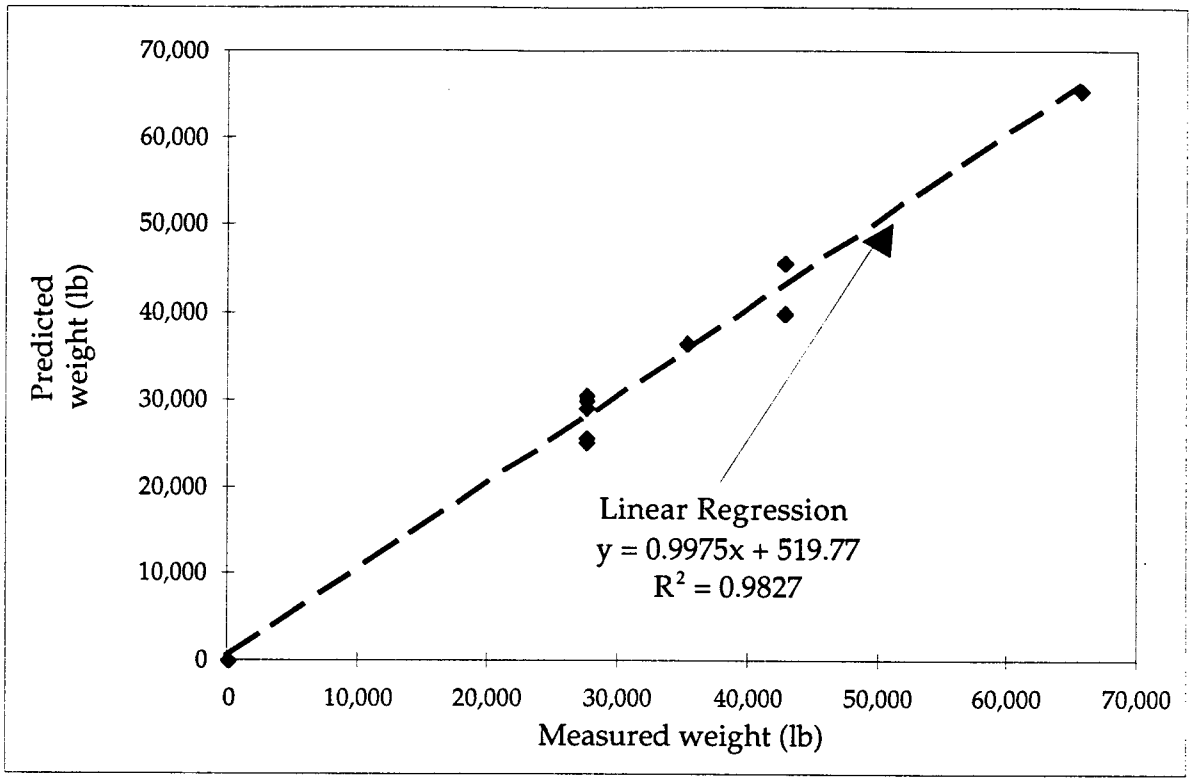

Figure 5.23. Correlation Between Measured and Predicted Weights from a Fiber-Optic Traffic Sensor at MacAsphalt Plant, Melbourne, Florida

Table 5.8. Deviation from Measured Truck Weight

Measured Weight (lbs)	Deviation from Measured Weight (%)
27500	11.8
35100	3
42700	7.6
65500	1

Note: 1 lb = 0.4541 kg

5.6 TESTS ON CANDIDATE FIBER-OPTIC SENSOR BACKFILL MATERIALS

Fiber-optic sensors were installed into a rectangular groove cut into flexible or rigid pavements. Once the sensor was epoxied into the groove with E-Bond's G-100, the groove must be backfilled with a flexible material (Figure 5.24). The installation was designed so that some portion of the wheel loads deform the flexible backfill material and place pressure on the sensor. This pressure caused a change in light intensity that was converted to a wheel load.

Selection of the flexible backfill material was critical because temperature affects its elastic modulus and therefore the amount of load propagated into the sensor. The sensors currently installed in the pavements have a roofing asphalt overlay. Because of its temperature dependency, a repeatable waveform has not been obtained from the sensor at different temperatures. In the hopes of correcting this installation problem, test specimens were cast of candidate backfill materials to replace the currently used Type III Steep roofing asphalt as the backfill material. The G-100 was also tested.

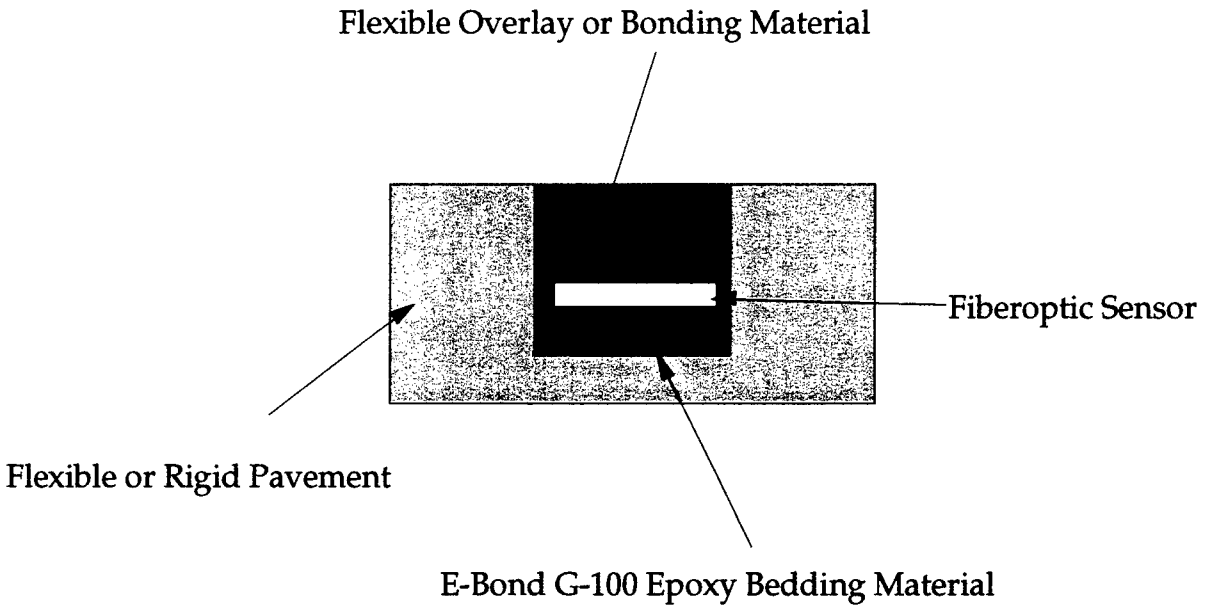

Figure 5.24. Current Field Cross-Section of Fiber-Optic Traffic Sensor

5.6.1 Testing Procedure

Test specimens were cast in cardboard rolls 1.6-inches (4.1 cm) diameter by 3.5-inches (8.9 cm) in length. Manila envelope mold bottoms were attached by using 5-minute epoxy. Care was taken not to get epoxy on the bottom of mold because it chemically degraded the cast material in those areas and made for a rough bottom during compression testing. Mixing proportions are indicated in Table 5.9 along with the ease of mixing and de-airing. The specimens were de-aired in a desiccating jar fitted with an aluminum top plate and hose barb for attaching the vacuum pump and gage. De-airing was accomplished under a vacuum of 28 inches (71 cm) of Mercury for 5 minutes.

Table 5.9. Study of Candidate Materials for use as Fiber-Optic Sensor Backfill

Product	Source	Reported Strength	Elastic Modulus (measured)	Poisson's Ratio (measured)	Comments
Slygard 170 (DC-170-2) Silicone Elastomer	Dow Corning (Engineering 517-496-4462) Purchase through Essex Brunnel (Frank Marillo) Orlando 1-800-805-4636	500 psi in Tension	400 psi	0.51	Carefully mix so as not to entrain air. Used 75 g of A to 75 g of B
Silastic M RTV Silicone Rubber	See above	650 psi in Tension	500 psi	0.55	10:1 by weight
Flexane 80 Two-Part Urethane	Devcon (Tech Assistance 1-800-933-8266) Danvers, MA Granger Co Wickham Road	2100 Psi in Tension	1200 psi	0.45	77(A):23(B) Used 77 gr A to 23 g B Very difficult to De-air as the product out gases.
Flexane 94 Two-Part Urethane	See above	2800 psi in Tension	n/m	n/m	69:31 Used 90 g A:40 g B Easy to work with
G-100	E-Bond Epoxies Ft Lauderdale 954-566-6555 Sikadur 22	8000 psi Compressive Sika 3778	60 to 310 ksi 1100 psi	n/m n/m	Use 25:1 mix by weight 200 g A:8 g B No De-airing Mix 1:1 by Volume
Lo-Modulus A two-part epoxy that can be mixed with sand to develop a mortar	La Vista Road Suite 100 Tucker, GA 30084 1-800-933-7452	Tensile 6000 psi Comp both at 14 days			Very difficult to De-air Very exothermic
Sikadur 35 Hi-Modulus epoxy adhesive	See above	11,800 psi Comp 7,200 psi Tension both at 7 days	n/m	n/m	Mix 2:1 by Volume 82(A) grams to 42 (B) grams by weight. No De-airing-was
Flexane 80 w/ Flex-Add	Devcon (Tech Assistance 1-800-933-8266) Danvers, MA Granger Co Wickham Road	not reported	450 psi	n/m	Used 77 g (A) to 23 g (B) 14 oz per 1 lb kit to obtain Shore 50A Used 2.4 oz or 72 ml (30 mls per oz)

n/m = not measured
Note: 1 psi = 7 kPa

Three temperatures were selected for thermally soaking the specimens (32° F, 72° F, and 140° F) because they represent the typical ranges of pavement temperatures occurring in Florida. Internal specimen temperatures were not measured at the time of testing but are considered to be close to the soaking values because the materials tested have low thermal conductivity. The coldest temperature was obtained with a freezer in an overnight soak with the hottest temperature obtained in a laboratory oven also overnight. The specimens were placed into an S-610 Brainard Kilman CBR/UCC testing machine instrumented with an LVDT for measuring total deflection and a load cell for measuring total load. The rate of deformation (travel of the head) was 0.025 in/min (0.06 cm/min) for all materials except the stiff G-100, which was tested at 0.005 in/min (0.01 cm/min).

The effects temperature had on the stress-strain response of the following specimens were analyzed:

Slygard 170
Silastic-M RTV
Flexane 80
G-100
Flexane 80 with Flex-add to decrease the hardness to Shore A 48

5.6.2 Slygard 170

The elastic modulus of the Slygard 170 (a silicone elastomer) remained curvilinear but constant with respect to temperature and had a value of 400 psi (2800 kPa) (Figure 5.25). This material was easy to use and was cast onto the top of a sensor when packaged in an aluminum channel mold. The special 1200 prime coat was not used in this initial test.

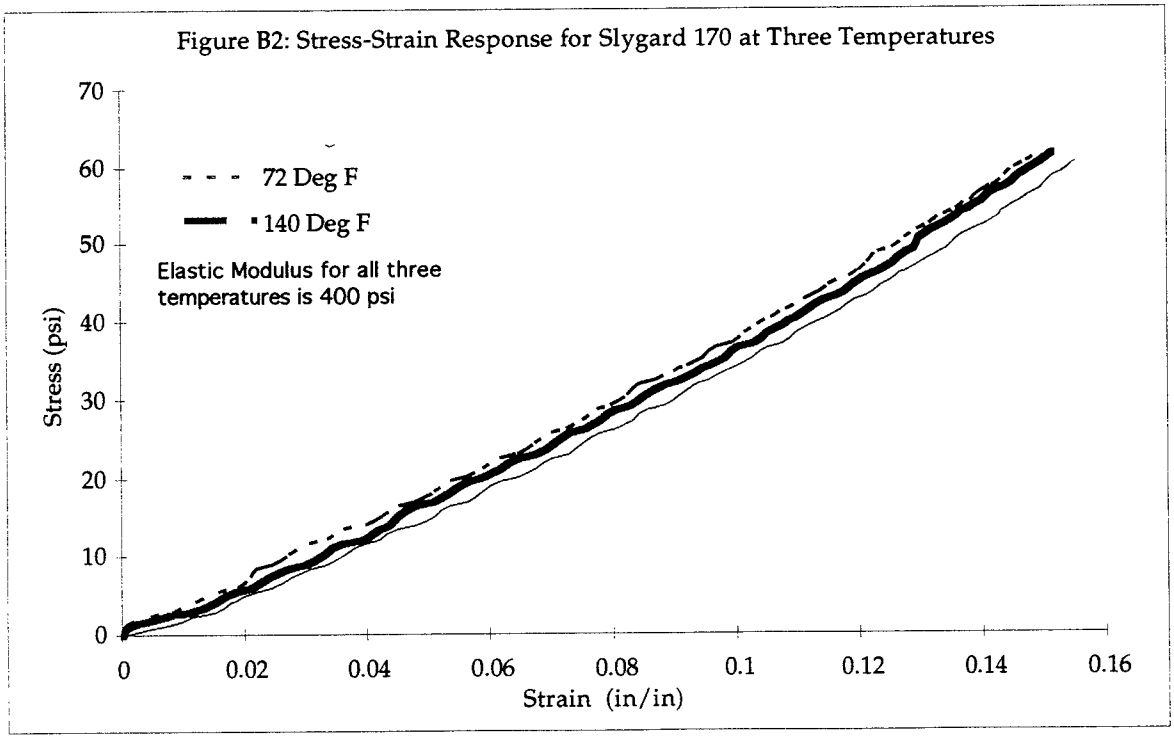

Figure 5.25. Stress-Strain Response for Slygard 170 at Three Temperatures

5.6.3 Silastic-M RTV

Silastic-M, a room temperature vulcanized (RTV) rubber, stress-strain response with respect to temperature is presented in Figure 5.26. The initial room temperature and cold temperature tests show that the stress-strain behavior is curvilinear, and the elastic modulus was 400 psi (2800 kPa). When heated and tested at 140° F the material rigidity increased to an elastic modulus of 630 psi (4410 kPa). This rigidity seemed to continue after the sample cooled to room temperature; therefore, the room temperature test was repeated showing that heating caused the elastic modulus to increase from 400 to 630 psi (2800 to 4410 kPa). The implications of these initial tests show that the material properties are affected by temperature and that the material may be unsatisfactory for use in sensor installation.

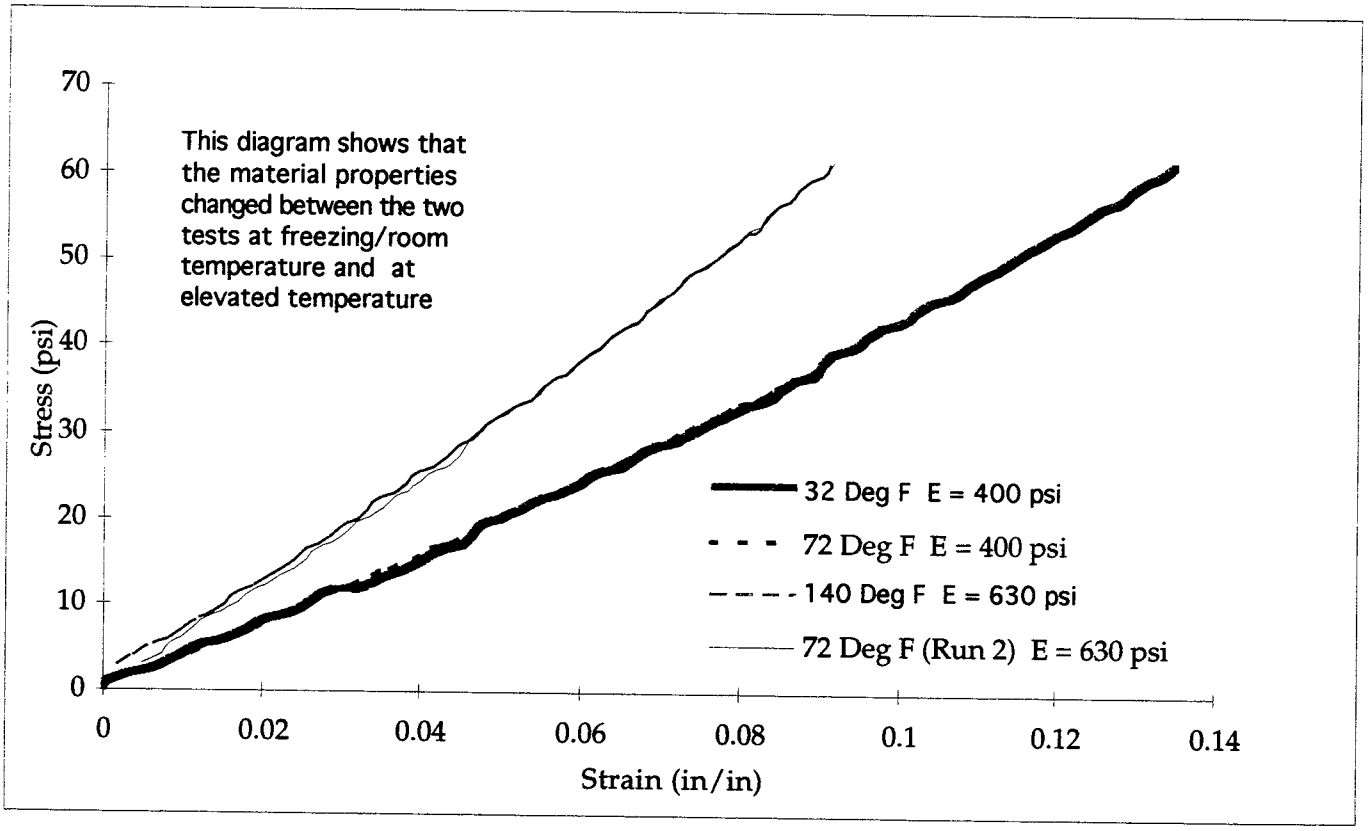

Figure 5.26. Stress-Strain Response for Sylastic M at Three Temperatures

5.6.4 Flexane 80

Flexane 80 is a urethane rubber successfully used by personnel working for the state of Arkansas for pavement/sensor applications. Figure 5.27 shows that at small strains it has elastic behavior at all temperatures, with the elastic modulus of 1200 psi (8400 kPa). At strains greater than 0.005 in/in the material appears to become stiffer. The elastic modulus decreases, however, at elevated temperatures. Analysis of sensor deflections at 50% transmissivity shows the sensor deflects approximately 0.004 inches (0.01 cm). If the thickness of the Flexane 80 was 0.375 inches (0.95 cm) over the top of the sensor, then strain becomes 0.01 in/in. This is outside the linear range of the material. Finite element modeling of the sensor may have accounted for this nonlinear behavior.

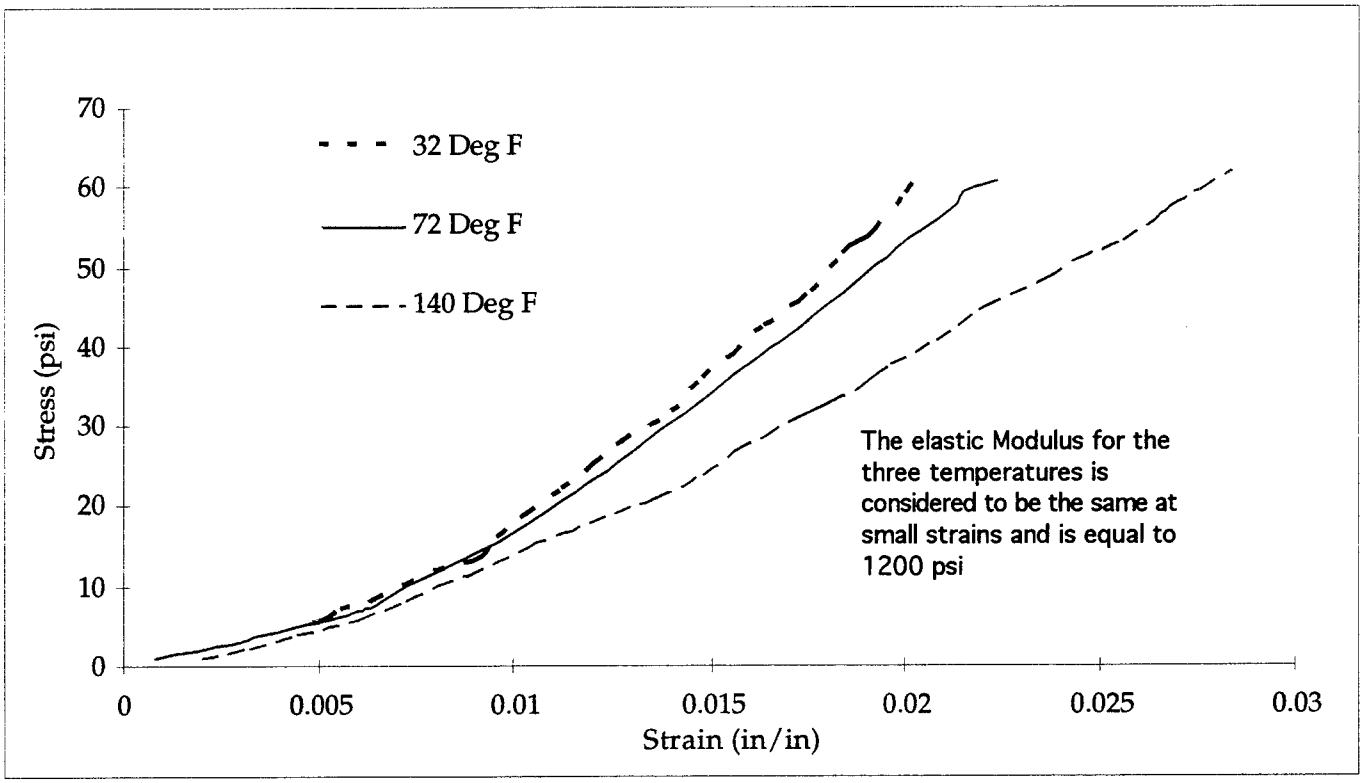

Figure 5.27. Stress-Strain Response for Flexane 80 at Three Temperatures

5.6.5 E-bond Epoxy G-100

E-bond Epoxy produces the compound G-100 specifically developed for bedding piezoelectric sensors into pavement. This material displays stress-strain behavior similar to the "SuperPave" asphalt concrete now being used to construct flexible highways. Figure 5.28 shows this material being dramatically affected by temperature with the elastic modulus varying from 310 ksi (2.2×10^6 kPa) at 32° F to 60 ksi (4.2×10^5 kPa) at 140° F. The stress-strain curve obtained at 32° F is linear. The curves obtained at room temperature and elevated temperatures are curvilinear. Figure 5.29 shows that G-100 is a linear elastic material at temperatures typically associated with pavements. This linear property may be useful when performing WIM because the sensor response can be more easily corrected.

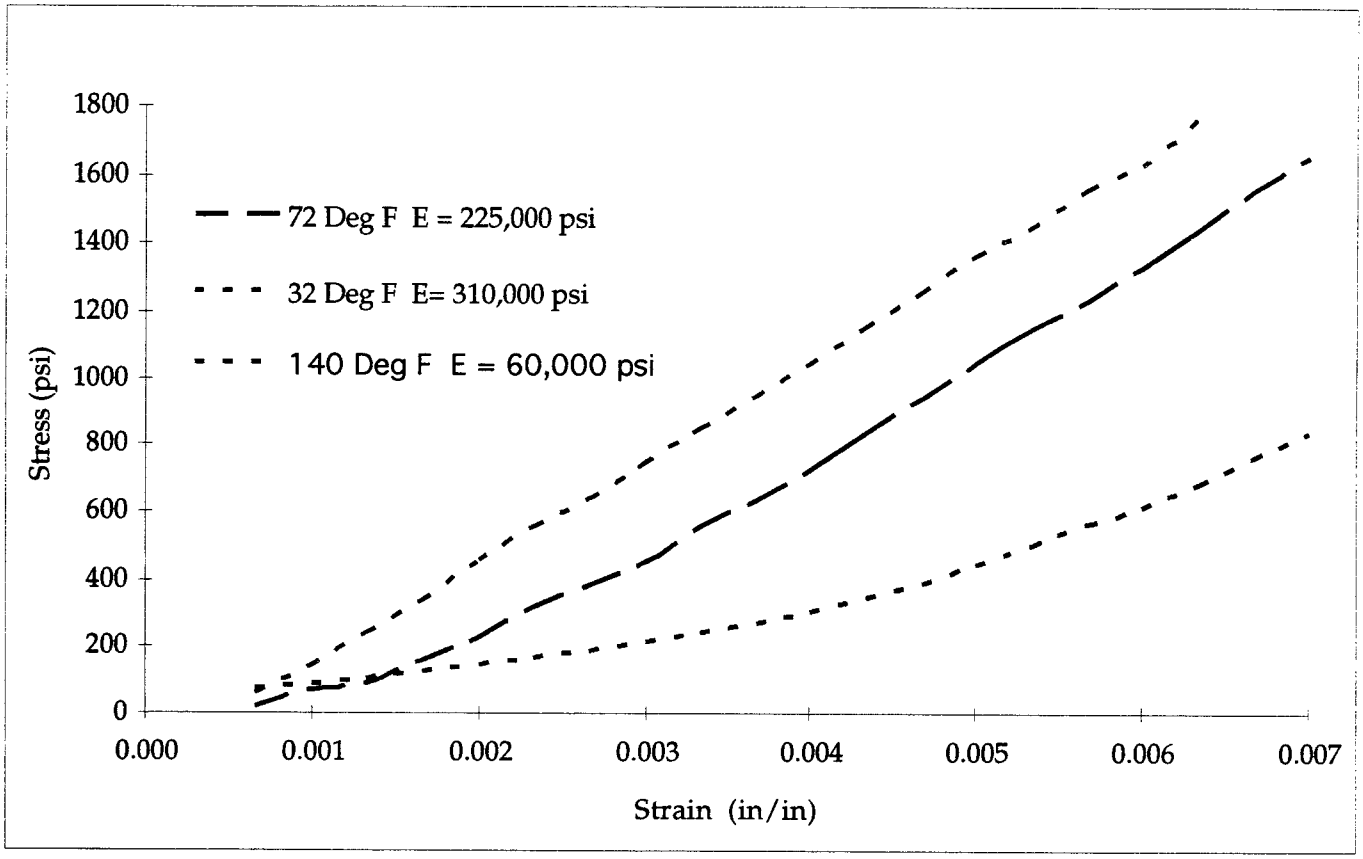

Figure 5.28. Stress-Strain Response for G-100 at Three Temperatures

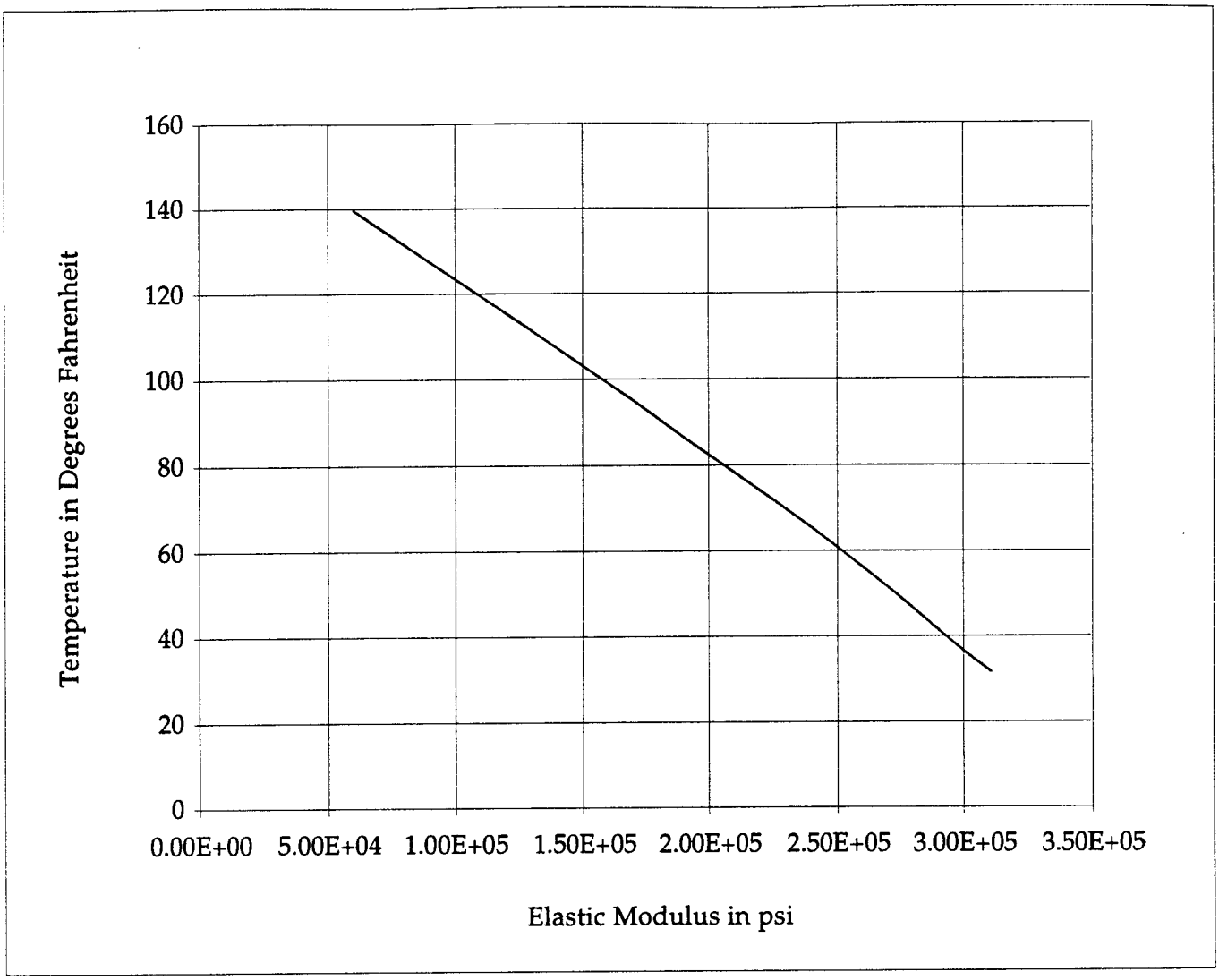

Figure 5.29. Change in Elastic Modulus of G-100 with Respect to Temperature

5.6.6 Flexane 80 with Flex-add

The fifth material tested was Flexane 80. It was softened with Flex-add to achieve a hardness of Shore 48A. The elastic modulus of the softened material changes from 340 psi (2380 kPa) at 140° F to 550 psi (3850 kPa) at 32° F when calculated at a strain of 0.05 in/in. The material specifications for the modified Flexane 80 are not available from the manufacturer due to the large number of mix combinations possible. The stress-strain curves presented in Figure 5.30 show that the response of the material is linear above 0.03 in/in strain and curvilinear below that value.

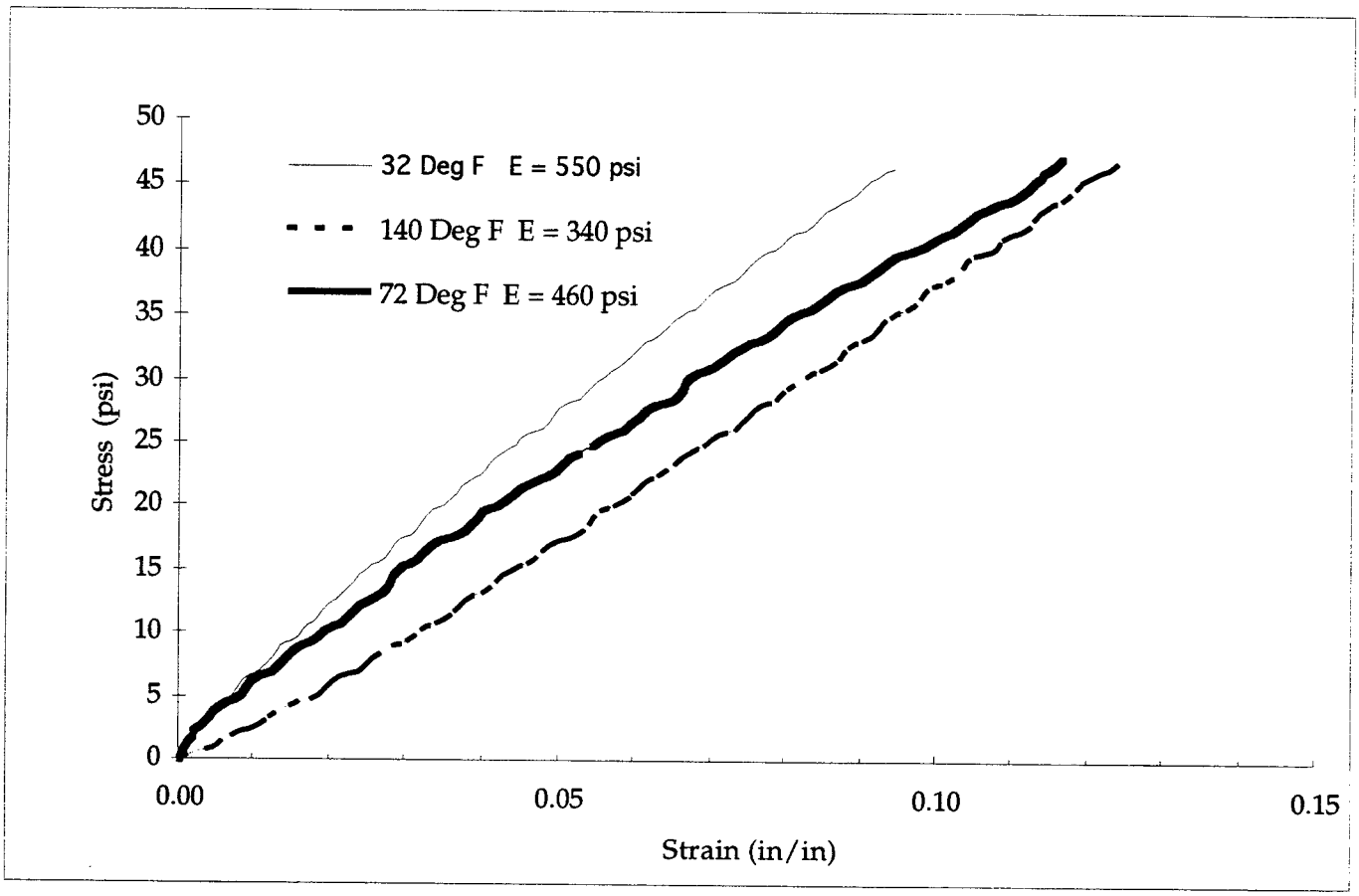

Figure 5.30. Stress-Strain Response for Flexane 80 with Flexadd at Three Temperatures

Two additional materials need to be tested before final comparisons can be made: Type III Steep roofing asphalt and a core of flexible pavement (preferably SuperPave). They should be tested under similar temperature and strain conditions. Once these materials are tested and analyzed, better choices can be made for future field installations.

5.7 FINITE ELEMENT MODEL OF AN INSTALLED FOTS

Selection of geometry and materials for installing the Fiber-Optic Traffic Sensor (FOTS) in pavements requires the knowledge of the stress distributions surrounding the sensor. A finite element analysis is being performed to achieve this goal. A 3,000 node MacNeal Schwendler FEA program based on NASA's Nastran (MSC/Nastran for Windows 95©) was selected as the analytical tool for this research. Because many of the materials used in the installation, as well as the sensor, exhibit nonlinear stress-strain behavior, both nonlinear and linear analyses were performed for comparisons. The stresses on the sensor at three depths and the deformations internal to the sensor were analyzed. The groove geometry modeled is representative of sensors installed in the flexible pavement at the Mac Asphalt plant driveway.

Two sensors were installed in seven foot (2.13 m) long grooves cut 0.5-inch (1.3 cm) deep by 0.41-inch (1.04 cm) wide, using two 3/16-inch (0.48 cm) thick abrasive blades stacked on a street saw. The bottom of the groove and 0.060-inch (0.15 cm) on each side of the sensor/Slygard assembly was filled with G-100 epoxy. A rectangular casting of Sylgard 170 (0.3-inch by 0.3-inch, 0.76 by 0.76 cm) was epoxied over the sensor in the laboratory prior to installation in the field. The compressive properties of the sensor, Sylgard and G-100 materials were used in the FEA model. Cylindrical tests specimens 3" (7.62 cm) long by 1.7-inch (4.3 cm) diameter were cast under vacuum and tested in compression at three temperatures typical of Florida pavements to determine their stress-strain behaviors. The sensor was compression tested at room temperature and its stress-strain curve is presented in Figure 5.31. Note the sensor's highly nonlinear strain response over increasing stress. The stress-strain response of the Sylgard 170, a very compressible rubber, does not vary with respect to temperature and is only slightly nonlinear (Figure 5.25). The G-100, a hard epoxy-sand mixture, displays a linear stress-strain response at 32° F, but as temperature increases the response grows more nonlinear (Figure 5.28). These data are entered into the library of the MSC/Nastran FEA program as functions and used in the analyses.

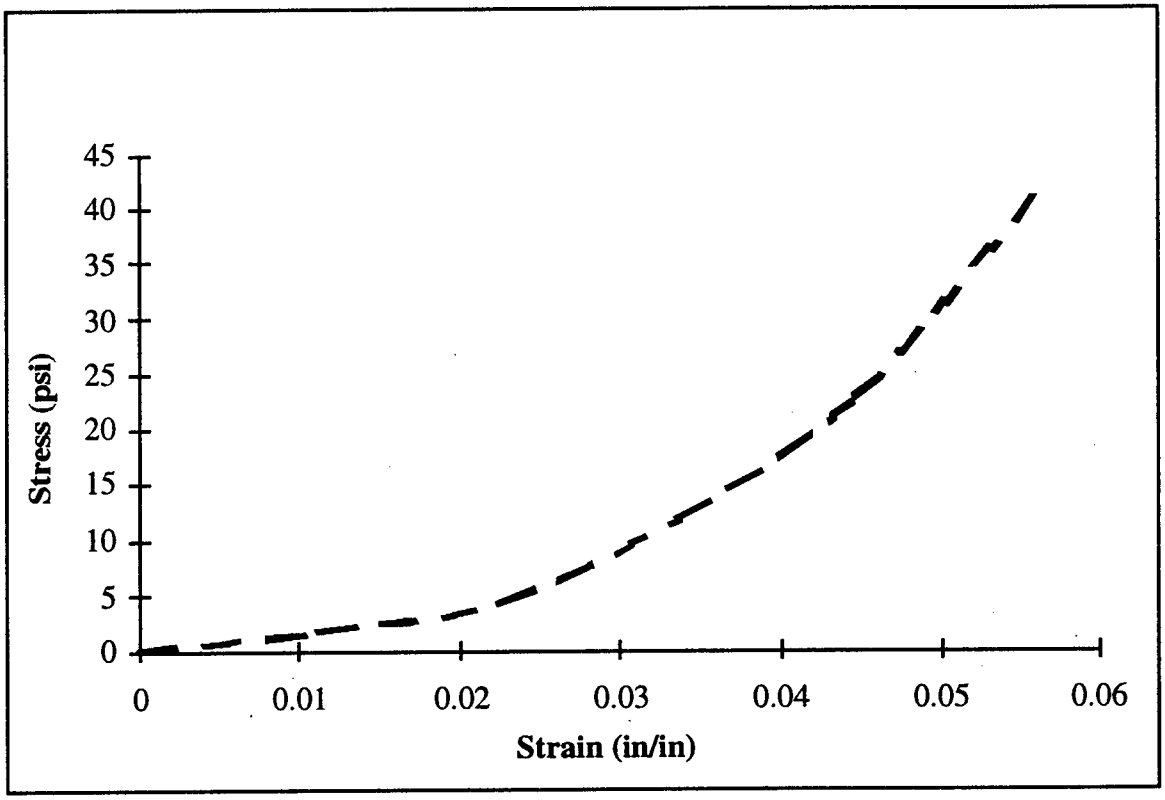

Figure 5.31. Stress-Strain Diagram for the Polyolefin Packaged Microbend Sensor

One of the three model geometry's was based on the field installation of two sensors placed 0.3-inch (0.8 cm) deep in MacAsphalt's flexible pavement. This model is shown as Figure 5.32. Note the boundary nodes of G-100 were fixed; no rotation or translation was allowed. Each 0.030-inch (0.08 cm) square quad element provided a convergent solution without the need for a finer mesh. The load was divided and applied to 13 top nodes reflecting either 30 psi (210 kPa) or 110 psi (770 kPa) tire pressures. Two additional geometry's were modeled with the sensor being raised to depths of 0.21-inch (0.5 cm) and 0.12-inch (0.3 cm) while the overall model dimensions of 0.51-inch (0.3 cm) by 0.42-inch (1.1 cm) were held constant. This allows the stresses with respect to depth of placement of sensor in the groove to be studied. The stress contours with respect to depth are shown in Figure 5.33 for a load of 110 psi (770 kPa) in a nonlinear static analysis. The Y-axis normal stress at the top of the sensor varies from 79 psi (553 kPa) (dark blue) at the center to less than 20 psi (140 kPa) (yellow) near the outside edges. Because the optical fiber lies in the center two-thirds of the sensor, stresses at the center node were averaged with the nodal stresses calculated three nodes to either side. This average value for all three depths and both stress conditions were plotted in Figure 5.34. Both linear and nonlinear analyses are plotted in this figure. These data show that a linear analysis is appropriate for small pressures (30 psi, 210 kPa) but at the higher pressures typical of truck tires a nonlinear analysis differs from the linear analysis by about 10%.

Deformation contours for 110 psi (770 kPa) static pressures modeled with nonlinear material properties are presented for a sensor located at depth 0.3-inch (0.8 cm) in Figure 5.35. The bottom nodes of the sensor rest upon the G-100 and display practically no deformation (50 to 60 millionths of an inch, 1.27-1.52 mm). The middle top node of the sensor deforms 0.0056-inch (14.2 mm) with respect to the bottom plate of the sensor. When the deformation in the center node was averaged with the deformation calculated three nodes to either side, a value of 0.0046-inch (11.7 mm) results and was plotted in Figure 5.36 for this 110 psi (770 kPa) nonlinear analysis. Calculated values for deformation for depths of 0.21-inch (0.5 cm) and 0.12-inch (0.3 cm) (linear and nonlinear) are all plotted in this figure. It was concluded that when either of these two methods of interpreting the model output was used, similar results are obtained. Before a definitive conclusion is presented with respect to the stress states surrounding the sensor, further modeling, laboratory and field tests are required.

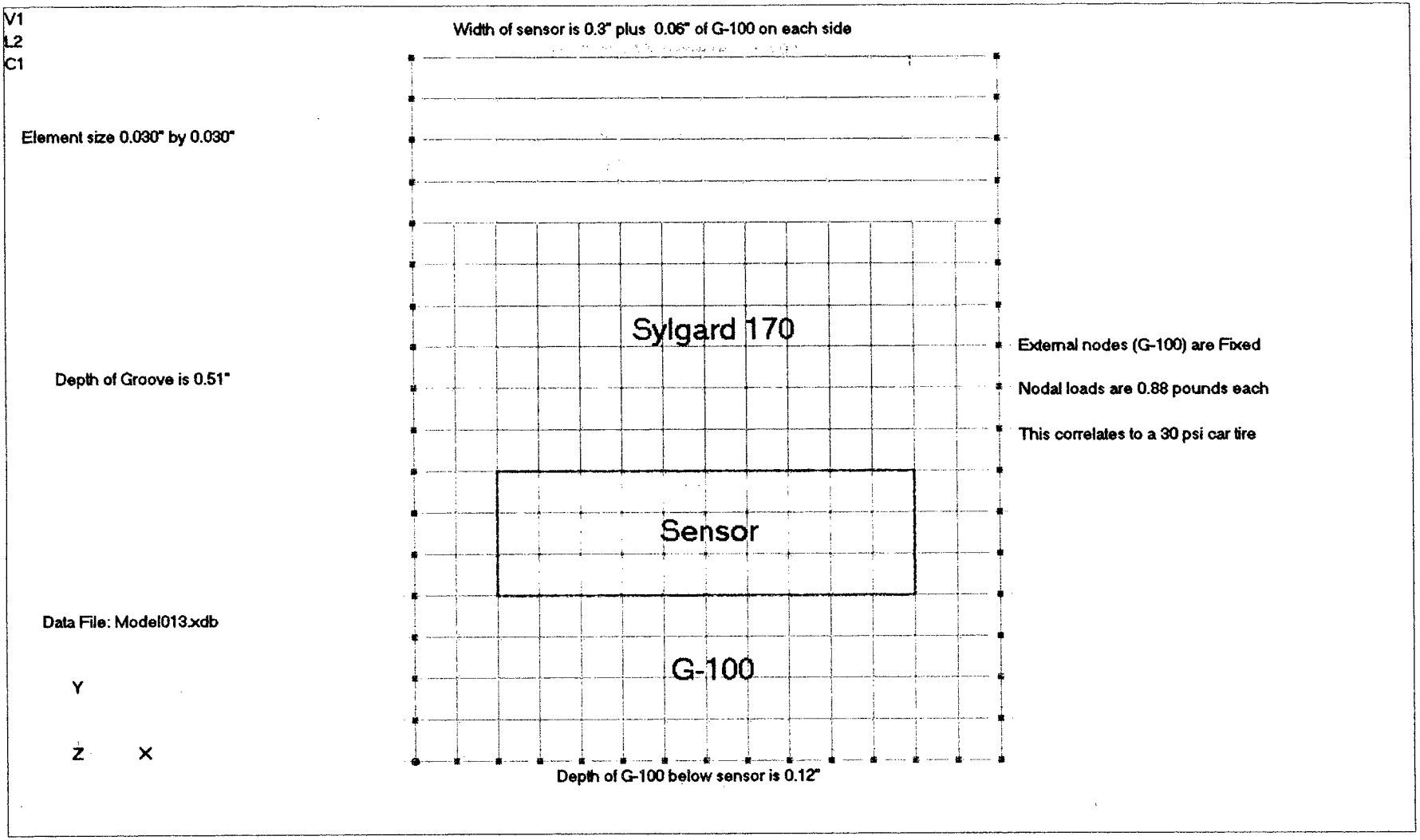

Figure 5.32. Model of FOTS Embedded at 0.3" (0.8 cm) in a Rectangular Groove (1 inch = 2.54 cm, 1 psi = 7 kPa)

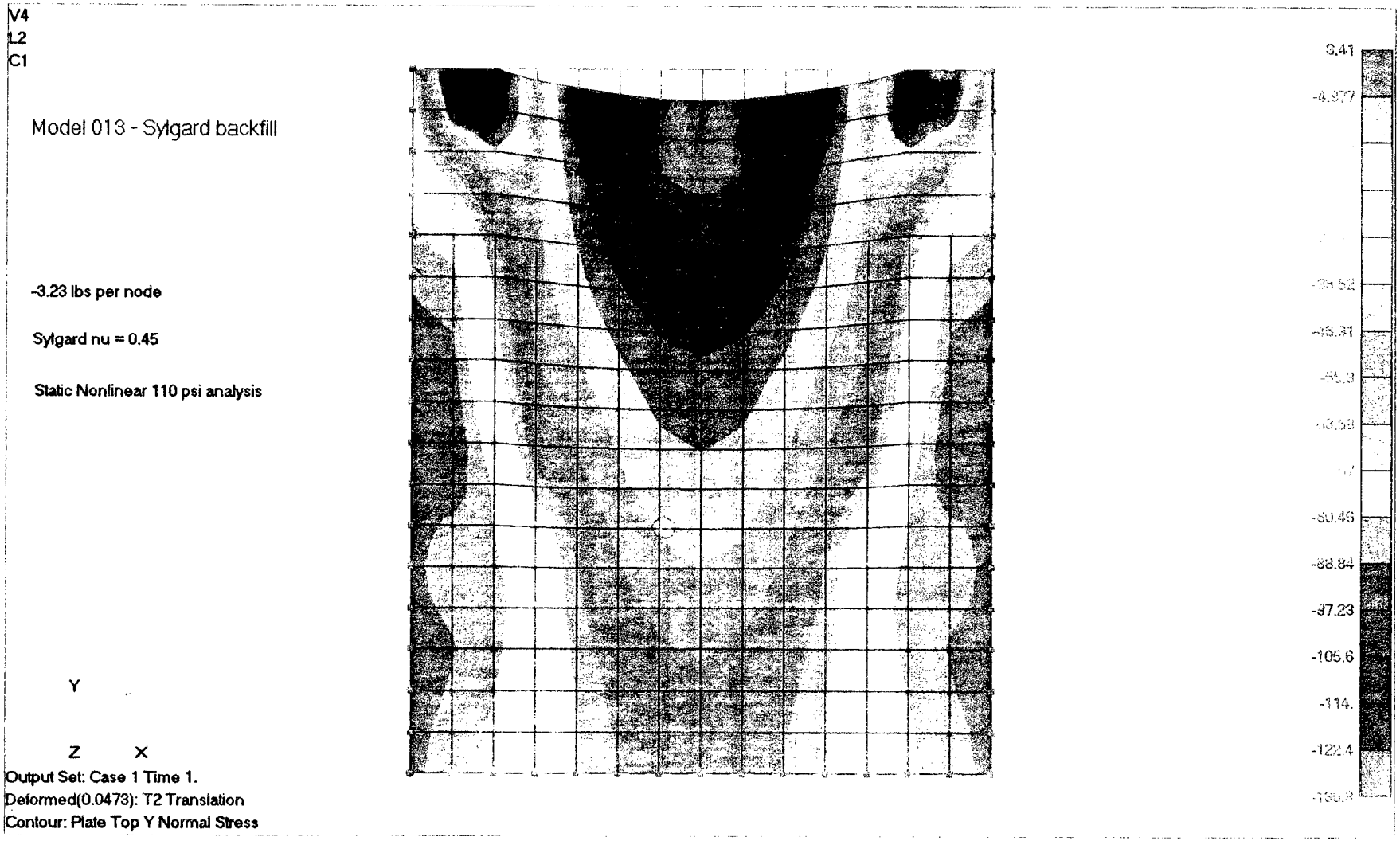

Figure 5.33. Model 013-Micorbend Fiber-Optic Traffic Sensor (1 psi = 7 kPa)

Figure E-6: Stresses Modeled at FOTS Top Plate while Embedded in Pavement

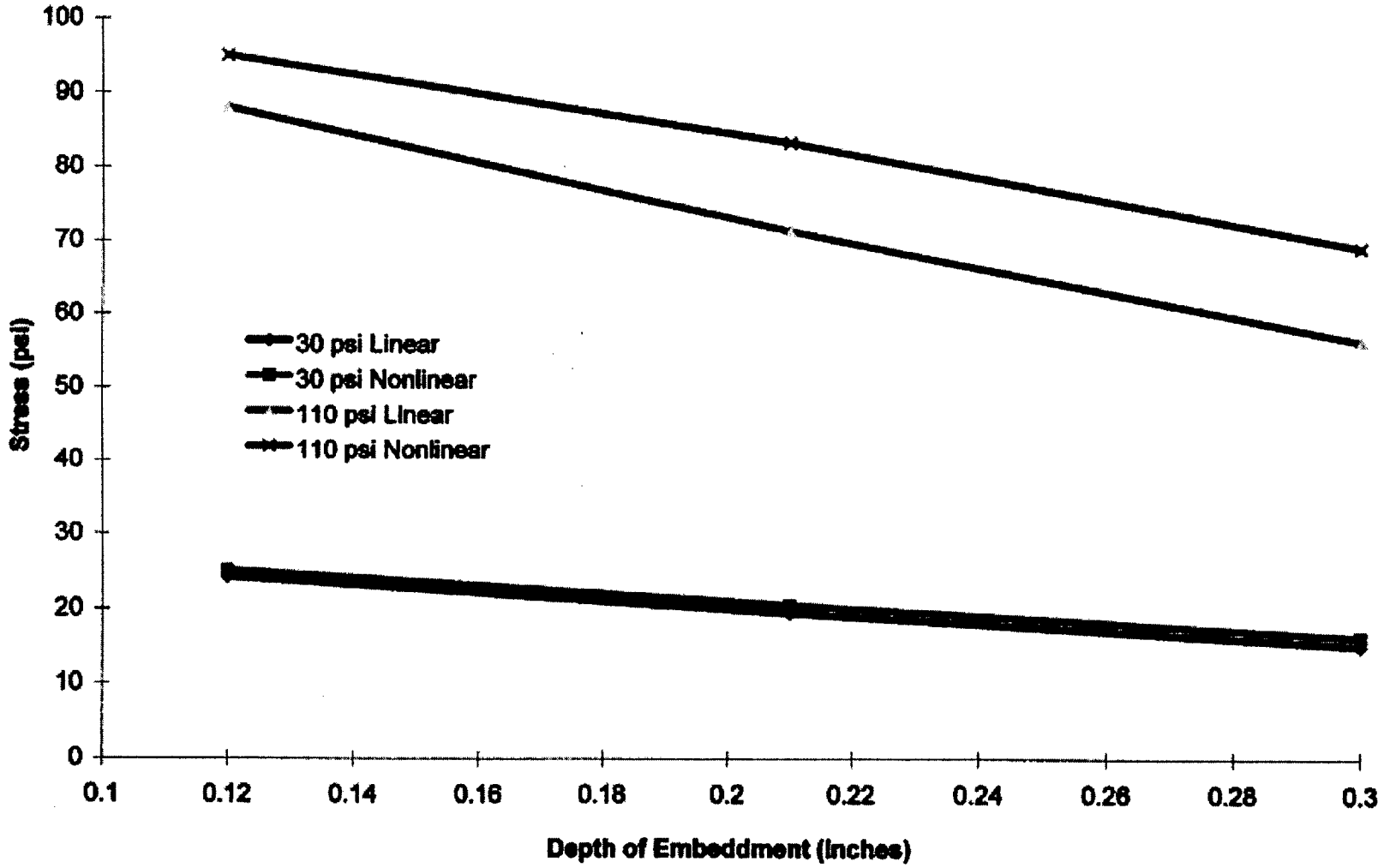

Figure 5.34. Stresses Modeled at FOTS Top Plate while Embedded in Pavement
(1 inch = 2.54 cm, 1 psi = 7 kPa)

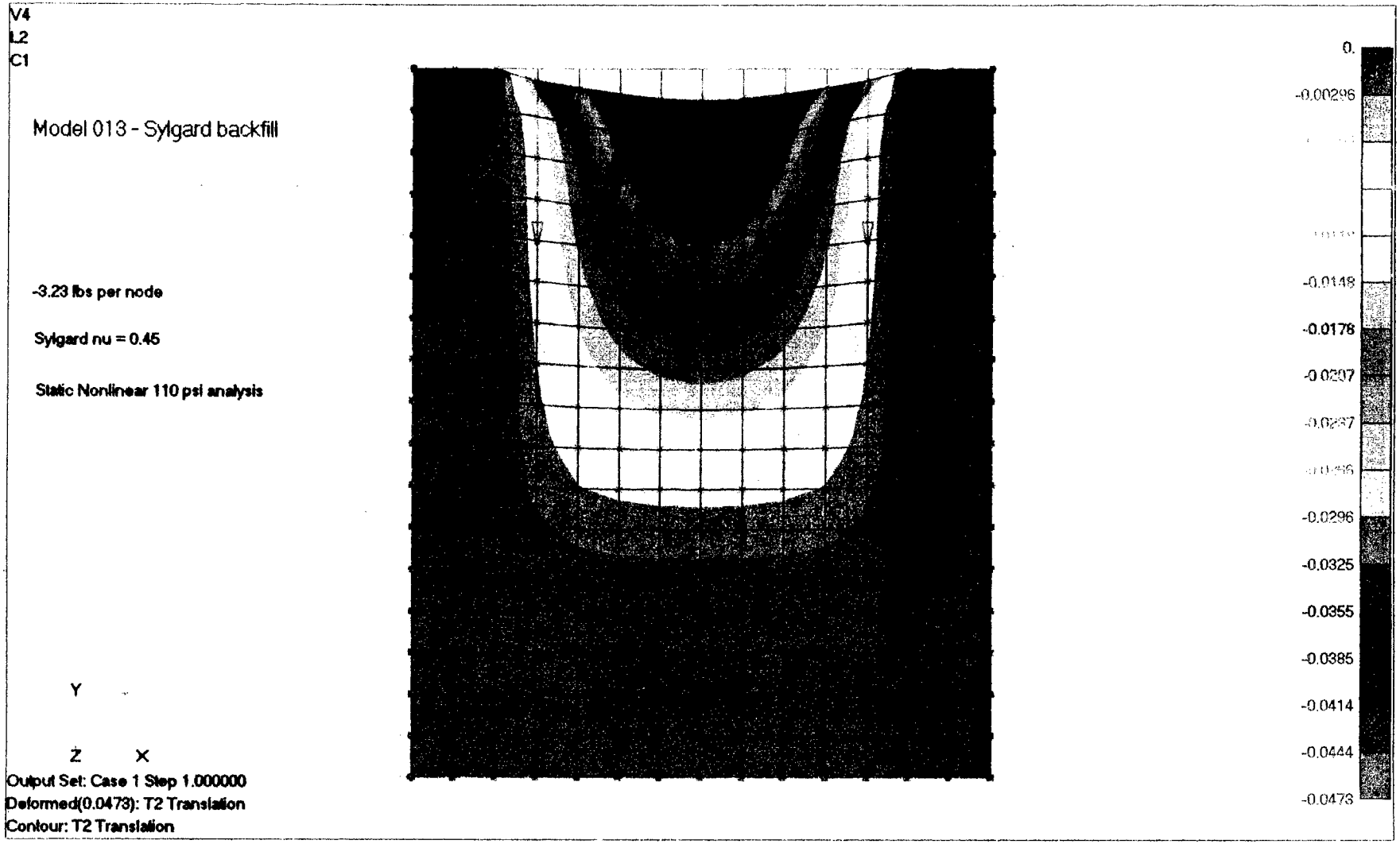

Figure 5.35. Model 013- Microbend Fiber-Optic Traffic Sensor
(1 psi = 7 kPa)

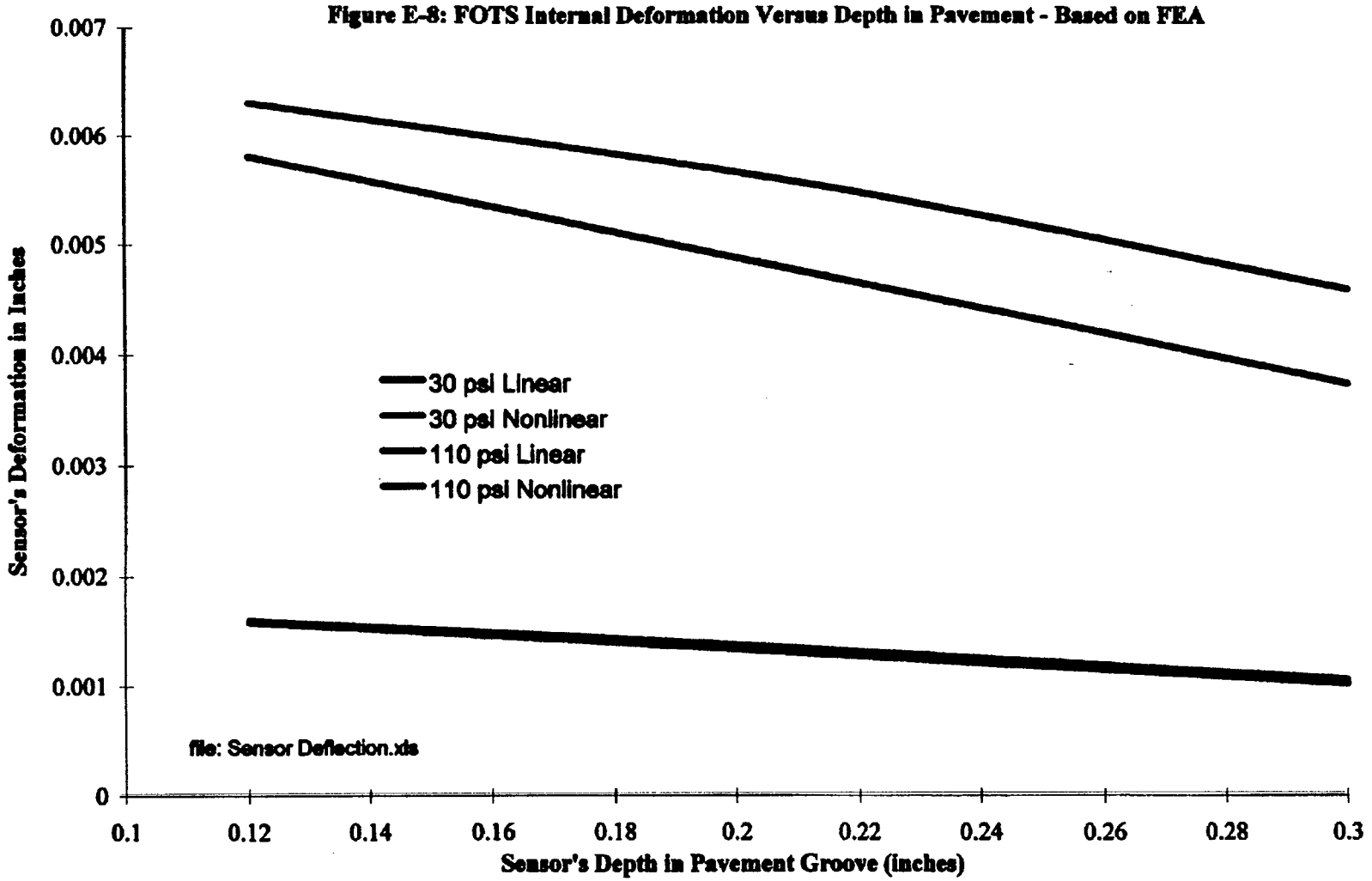

Figure 5.36. FOTS Internal Deformation versus Depth in Pavement-Based on FEA
(1 inch = 2.54 cm, 1 psi = 7 kPa)

CHAPTER 6

6.0 CONCLUSIONS AND RECOMMENDATIONS

6.1 CONCLUSIONS

A field ready fiber-optic traffic classifying and weigh-in-motion sensor was successfully developed and used in both flexible and rigid pavements outside the Florida Tech campus. Five, 6-foot (1.8 m) long sensors have been embedded into these pavements and subjected to heavy vehicle loading. The sensors in the rigid pavement have been subjected to approximately 10,000 loaded concrete ready mix trucks weighing about 60,000 lbs (27246 kgs) each and the sensors in the flexible pavement have been subjected to about 3,000 loaded ready mix and hot mix asphalt trucks.

Corning 50/125/250μm and Corning 62.5/125/250μm fibers were used in the construction of a set of eight microbend sensors with single-sided deformers made of polymer mesh. Mesh spacing was chosen from the experimentally measured optimum spatial wavelengths for the two fibers. By measuring the intensity versus load curves for each of these combinations, a sensitive microbend sensor was developed. The chosen combination was the Corning 50/125/250μm fiber on a Tefzel® 23.5×23.5 openings per inch mesh. The sensor was packaged in heat-shrink tubing and tested in the laboratory.

- In 1895, Hertz developed a method of estimating the maximum contact stresses between two perpen dicular cylinders (Roark, 1943). With this model, general predictions for the contact stresses between the fiber and mesh in a FOTS were made. To develop conservative predictions, perform calculations assuming that all the stress is taken by the glass core in the fiber.

- The OTDR static failure test provided quick, real time monitoring of fiber failure loads.

- From the analysis performed using five assumed fiber and mesh stress contact cases, fiber failure did not occur due to bending.

- Based on experimental values, the failure load for various fiber/mesh combinations is a function of the elastic modulus of the mesh. From the OTDR failure test on four mesh strands: polyester, polypropylene, nylon, and Tefzel®, a nylon fishing line and a steel wire, the lower the elastic modulus of the strands the higher the failure load (Figure 3.9).

- The shape of the mesh may be a major factor in evaluating the variability of the fiber failure load. Woven mesh strands from four different materials (polyester, polypropylene, nylon and Tefzel®) produced large variations in failure loads while perfectly straight mesh strands produced failure loads with very little variability.

- After experimentally measuring the optimum spatial wavelength for several unique optical fiber specimens, the optical fiber with the greatest intensity loss at the lowest load was found to be the Corning acrylate coated 50/125/250μm fiber at a spatial wavelength of 1.06 mm.

- The graded-index fibers tested were more sensitive than the step-index fibers in the microbend sensors.

- An experiment was designed to compare the intensity, load, and displacement measurements from single-sided and double-sided microbend deformers using two fiber specimens with the same core/cladding sizes and numerical aperture, but different coating types and thickness. Both fibers were more sensitive in the double-sided microbend deformers than in the single sided deformers; however, much larger deflections were required to achieve these sensitivities. Traffic sensors will not experience these deflections; therefore, the double sided deformers should not be used. The single-sided microbend deformers gave results that indicated that the thick coated acrylate fiber was significantly more sensitive than the thin coated polyimide fiber. From this, it was determined that single-sided microbend deformers worked best with fibers thick, soft coatings, such as the acrylate-coated fiber.

- The intensity variations along the sensor length measured with the LEGO® sled were repeatable. The intensity profile showed a 30% variation in the intensity loss of the sensor along the length.

- The microbend sensor ARL 1, 6-foot (1.8 m) long by 5/16-inch (0.8 cm) wide, was installed into Florida Tech's ARL parking area pavement. The microbend sensor was installed 1/4-inch (0.6 cm) deep in a 1/2-inch (1.3 cm) wide groove. The groove was filled with Type III roofing asphalt that was screeded level with the surface of the pavement. After installation, the intensity along the length of the sensor was measured using numerous passes of a Class 2 automobile. Plots showed more than 40% intensity variation along the length. An attempt to correlate this data with the intensity along the length measured in the lab showed very few similarities. The surface profile of the asphalt seemed to correlate better to the variation in intensity along the length. The thickness of the asphalt filler along the sensor also seemed to correlate with the magnitude in intensity loss. The thinner the filler, the greater the intensity loss.

- The development of virtual interfaces in LabVIEW® for field data acquisition was developed, along with a complementary virtual interface to selectively view captured waveforms. On November 20, 1996, the virtual interface was used to capture waveforms from a Class 2 Dodge Colt, Class 2 Mercedes Benz, Class 2 Jeep Cherokee, and Class 5 garbage truck. The waveforms from these vehicles were used to demonstrate the capabilities of the fiber-optic microbend sensor for use in traffic classification and WIM. For traffic classification, it was demonstrated how an electronic system could use the signals from these vehicles and generate the inputs used by a traffic computer to perform classification.

- A method of using the contact length measured from the output waveform along with constant values of tire pressure and tire width for each class of vehicle resulted in the successful prediction of half-axle loads within 20% of the static half-axle loads. This algorithm to predict the half-axle loads had no calibration factors applied to it, showing that the calibration procedure currently used for WIM sites may be minimized or eliminated with the use of the fiber-optic microbend sensor.

6.2 RECOMMENDATIONS

- From the results of the OTDR failure test on four mesh strands (polyester, polypropylene, nylon, Tefzel®), the mesh that resisted the highest failure load was a Teflon mesh named Tefzel® at 500 lbs (227 kgs). It is recommended for use in the FOTS.

- Additional OTDR failure tests should be performed using woven and perfect mesh strands. The results of testing woven strands can be used to make conclusions about the level of quality control during manufacturing. The results of the perfect strands can be used in the sensor design process to obtain good fiber/mesh combinations and correlations.

- Construct a microbend sensor with precisely machined deformers to study the effects of loading length and variation in sensitivity along the length by eliminating the effects of mesh variation and spray adhesive in the sensor.

- Study various filler materials and installation procedures to understand sensor response and performance.

- Study the effects of vehicle speed on the output waveform.

REFERENCES

Ansari, F., *Applications of Fiber-Optic Sensors in Engineering Mechanics*, ASCE.

Askeland, D.R., *The Science and Engineering of Materials*, 3rd Edition, PWS Publishing Co., Boston, 1994.

ASTM, "*Standard Specification for Asphalt Used in Roofing*," Designation: D 312-89, 1990, pp. 54-55

ASTM, "*Standard Specification for Highway Weigh-In-Motion (WIM) Systems with User Requirements and Test Method*," Designation: E 1318-92, 1993, pp. 695-706.

Beer, F.P. and Johnston Jr., E.R., *Mechanics of Materials*, 2nd Edition, McGraw Hill, Inc., New York, 1992.

Biswas, D.R., "Characterization of polymide-coated optical fibers", Optical Engineering, Vol. 30, No. 6, June 1991, pp. 772-775.

Corning Glass Works Telecommunications Products Division, *at the core*, Corning, NY, 1988.

Cosentino, P.J. and Grossman, B.G., 1996, "Development and Implementation of a Fiber Optic Vehicle Detection and Counter System," Report FDOT, Agency Contract No. B—9213.

Cosentino, P., Grossman, B., Shieh, C.S., Doi, S., Xi, H., and Erbland, P., 1994, "*Fiber Optic Chloride Sensor Development*," In Press ASCE Journal of Geotechnical Engineering.

Diemeer, M.B.J. and Trommel, E. S., "*Fiber-Optic Microbend Sensors: Sensitivity As a Function of Distortion Wavelength*," *Opt. Soc. America*, 1984.

Gere, J.M., and Timoshenko, S.P., *Mechanics of Materials*, 3rd Edition, PWS-KENT, Boston, 1990.

Grossman, B., Cosentino, P., Kalajian, E., Kumar, G., Doi, S., and Verghese, J., 1994, "*Fiber Optic Pore Pressure Sensors Development*," In Press Transportation Research Record. Presented at the 73rd Annual Transportation Research Board Meeting Washington D.C., January 1994.

Kerbein, Shawn A., 1997, "*Personal Communications*," Corning Information Service.

Kim, B. Y. and Shaw, H. J., November, 1989, "*Multiplexing of Fiber-Optic Sensors*," Optic News, 35-42.

Lagakos, N., et al., "*Microbend Fiber Optic Sensor*," *Appl. Opt.*, 1987.

Laser Precision Corporation, *TD-9960 Operating Instructions*, Revision D - 16098, Utica, New York, May 1991

Lumite® Division of Synthetic Industries, *Product Sample Booklet*, Gainsville, Georgia, 1996.

Roark, R.J., *Formulas for Stress and Strain*, 2nd Edition, McGraw-Hill Book Company, Inc., New York, 1943.

Taylor, C.L., *Investigation of Fiber-Optic Microbend Sensors for Use in Traffic Applications,* Florida Institute of Technology, Melbourne, Florida, 1996

Tooley, F.V., *Handbook of Glass Manufacture*, Ogden Publishing Co., New York, 1953.

U.S. Department of Transportation, Traffic Monitoring Guide, Office of Highway Information Managment, October 1992.

Wolfbeis, O. S., 1989, *"Novel Techniques and Materials for Fiber Optic Chemical Sensing*," Optic Fiber Sensors, Springer-Verlag Berlin, 416-424.

Yoder, E.J. and Witczak, M.W., *Principles of Pavement Design*, 2nd Edition, Wiley-Interscience, New York, 1975.

Appendix A
OTDR Failure Test Procedure

One fiber, the Corning® 50/125/250 acrylate coating and five mesh types (1 polyester, nylon and Tefzel®, and 2 polypropylenes) were selected for testing. Twenty trials of each combination of fiber and mesh were conducted to obtain an average fracture load and to determine if repeatable results could be obtained.

An optical fiber was attached to an aluminum plate and placed over a single strand of mesh 2-inches long (Figure A1). The mesh strands were obtained by removing a single strand from the manufactured mesh. One fiber end was connected to an OTDR with a bare fiber adapter and the other fiber end was not connected to allow light to reflect back to the OTDR (Figure A2). The fiber, placed on a spool, was several meters in length to allow multiple tests to be performed (Figure A2). The fiber and mesh were then centered on the bottom platen of the compression machine. The OTDR was programmed to display a real-time image of the reflection within the fiber. Peaks A and B, depicted in Figure A2 and Figure A3 on the OTDR monitor, represent the connection between the fiber and OTDR and at a small distance, less than a foot, before the looped end of the fiber attached to the aluminum plate, respectively. An aluminum top plate, 2-inches long and ½-inch wide, was placed over the fiber/mesh section. The fiber/mesh test section was loaded gradually, using one rotation of the compression machine load lever every five seconds, until fracture within the fiber was detected by the OTDR. During loading, the second peak displayed on the OTDR monitor (peak B), gradually decreased; however, a sharp jump in that peak indicated failure within the fiber (refer to Figure A3 through Figure A6). The corresponding load on the compression machine was recorded at the instant the sharp jump occurred.

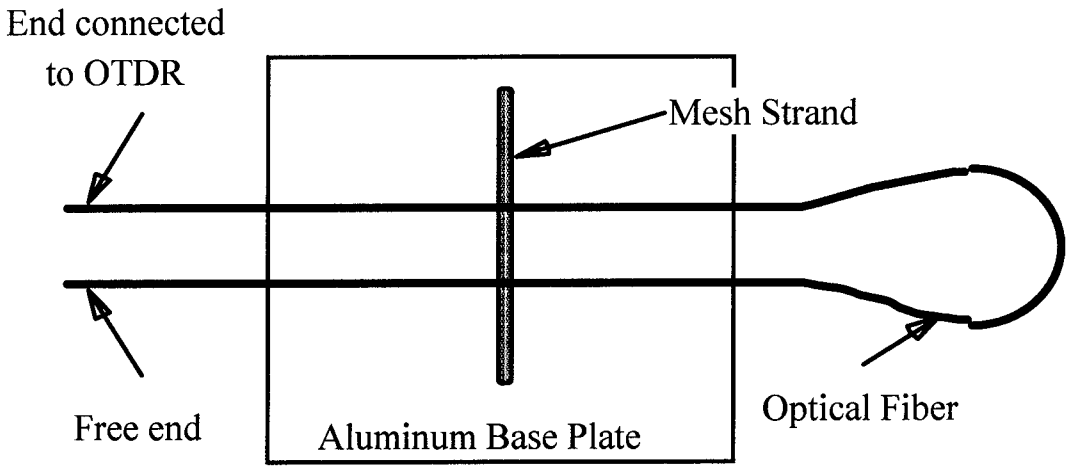

Figure A1. Fiber and mesh attached to aluminum plate for OTDR failure test

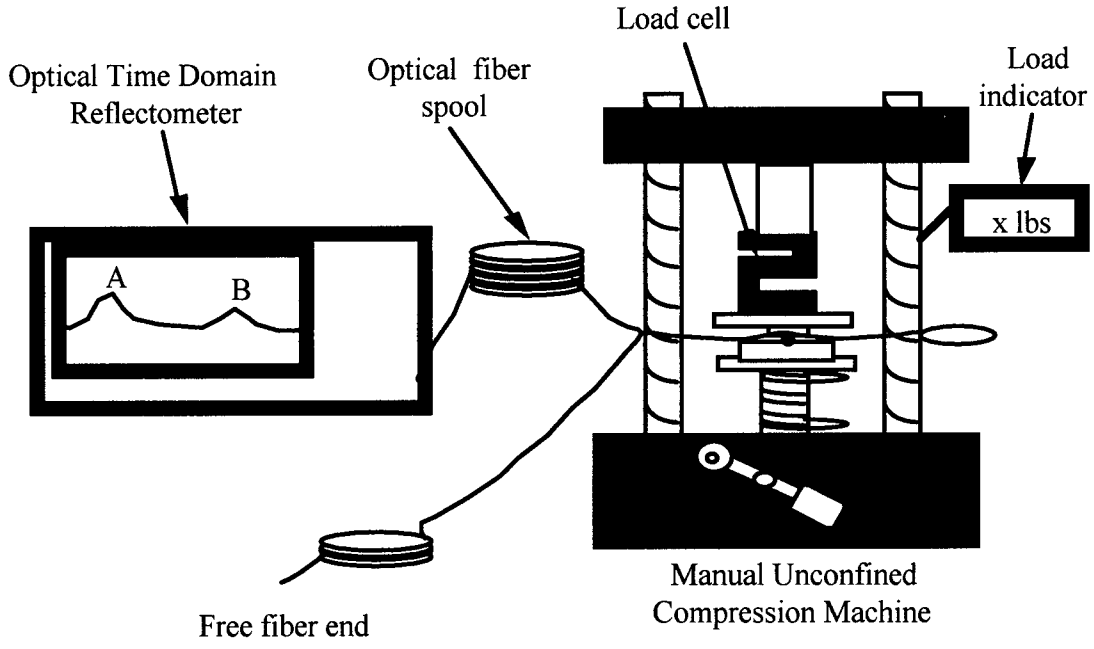

Figure A2. Schematic of OTDR failure test

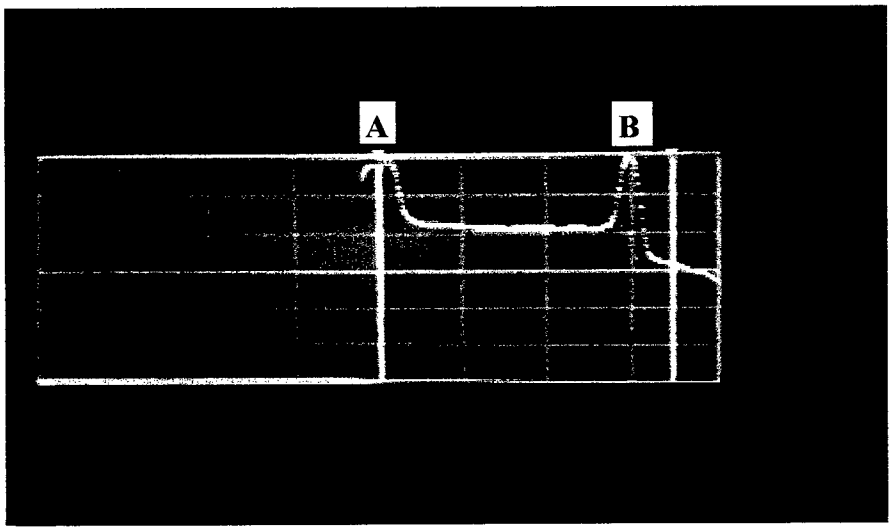

Figure A.3. OTDR monitor depicting peaks A and B before loading

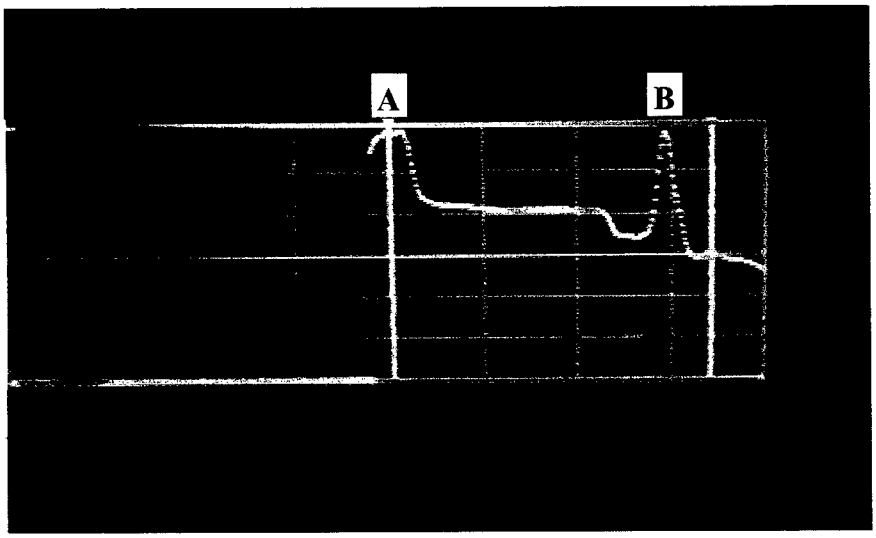

Figure A.4. Decreasing peak B during beginning of loading

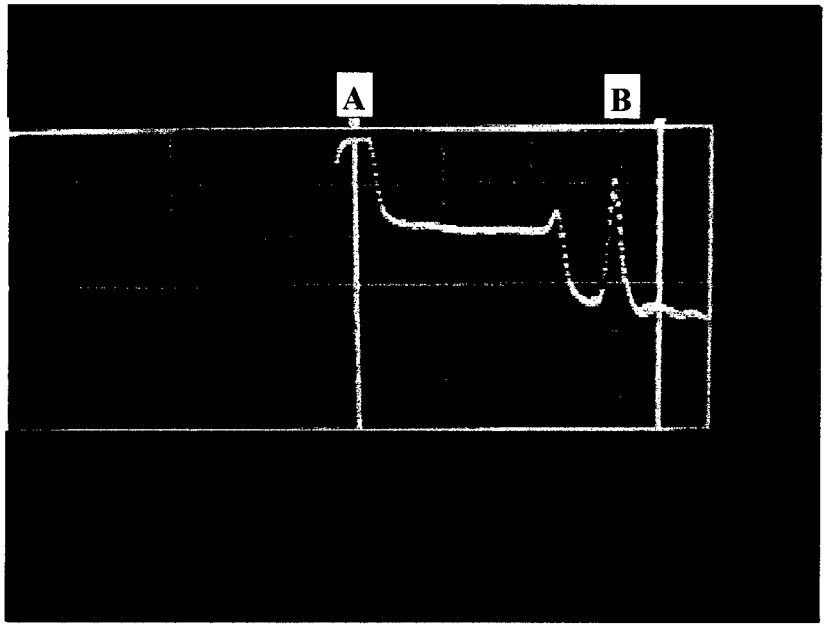

Figure A.5. Continued decrease in peak B before fiber failure

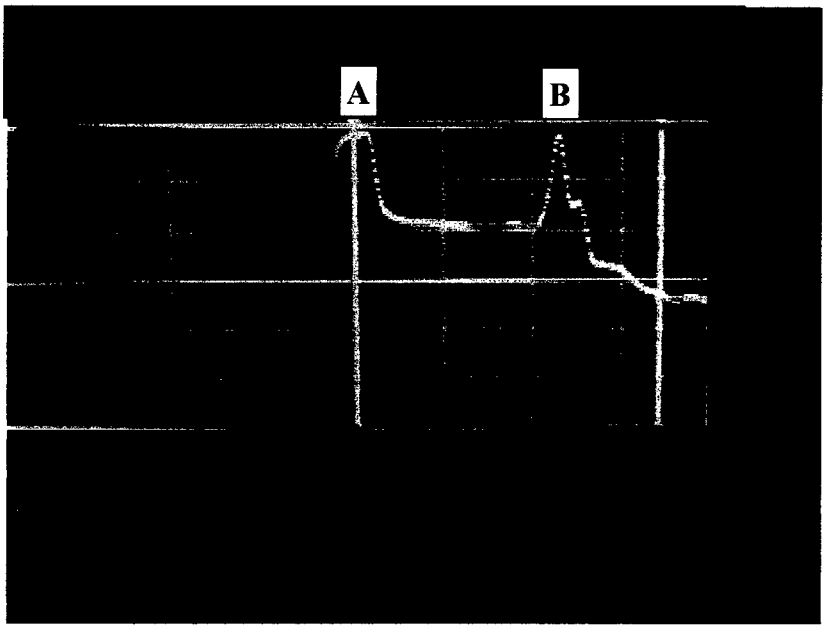

Figure A.6. Peak B after fiber has failed

It should be noted that the mode in which the OTDR pulse scan was monitored has three options; real time, fast scan, and slow scan. Depending on which mode was used, the shape in the peaks vary. The real time scan was chosen for each test because it couples a laser through the fiber for five minutes and displays the scan continuously on the OTDR monitor. This real-time mode acquires data several times a second. Fast scan collects data over five seconds and averages it out before displaying a pulse scan, then the laser shuts off. This monitoring method can present problems if during a test the fast scan button is not repressed and the sample is still being loaded, the fiber may have broken before the scan was taken. The same scenario can happen with the slow scan, only there is a 90-second time limit for each scan. The pulse shape for both the fast and slow scans, was much clearer and it may have been easier to recognize a jump in the peak. Trial tests were run at each mode. Recognizing the failure load during any of the three modes was the same. No distinct difference in loads was noticed from test to test, only a change in peak shape. Also, because each fiber/mesh combination fails at various loads, the time frame of the loading cycle may outlast the five second or 90-second time frame of the fast and slow scan mode. Therefore, it was recommended to use the real-time scan. In general, it was easier to use the real-time mode due to the continuous laser supply over the five minute length.

Appendix B
OTDR Failure Test Histograms

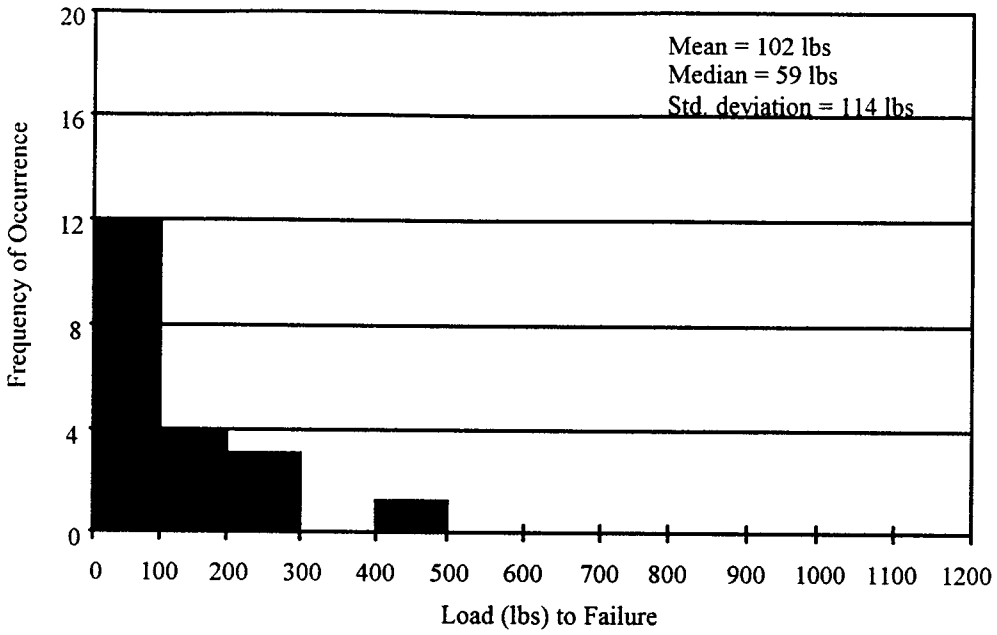

Figure B.1. Histogram from 20 Fracture Tests on 50/125/250 Fiber and 20 mil Diameter Polyester Mesh

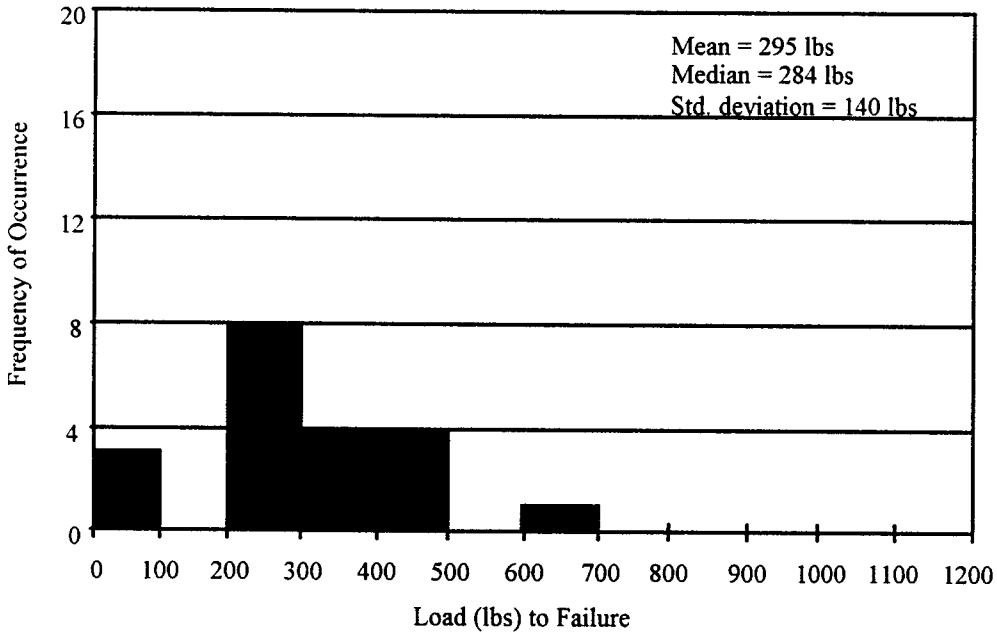

Figure B.2. Histogram from 20 Fracture Tests on 50/125/250 Fiber and 20 mil Diameter Polypropylene Mesh

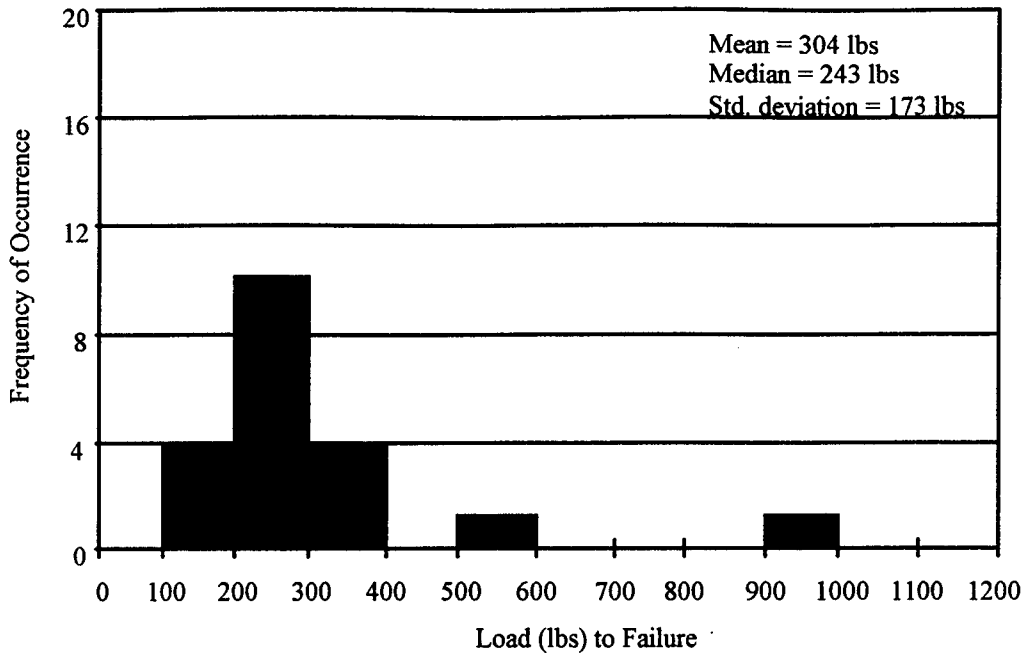

Figure B.3. Histogram from 20 Fracture Tests on 50/125/250 Fiber and 10 mil Diameter Polypropylene Mesh

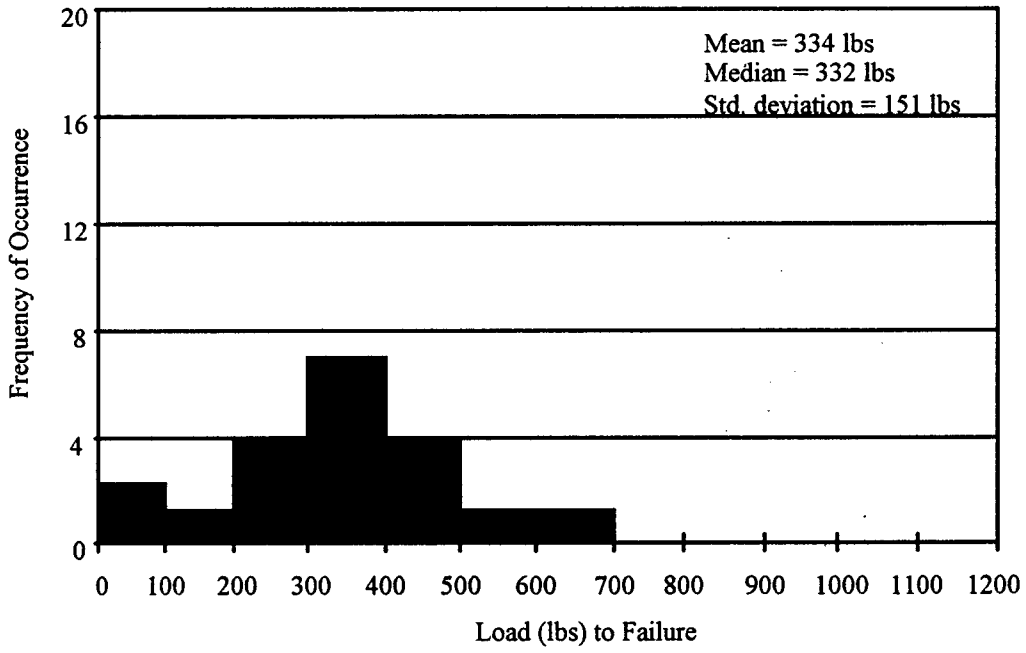

Figure B.4. Histogram from 20 Fracture Tests on 50/125/250 Fiber and 10 mil Diameter Nylon Mesh

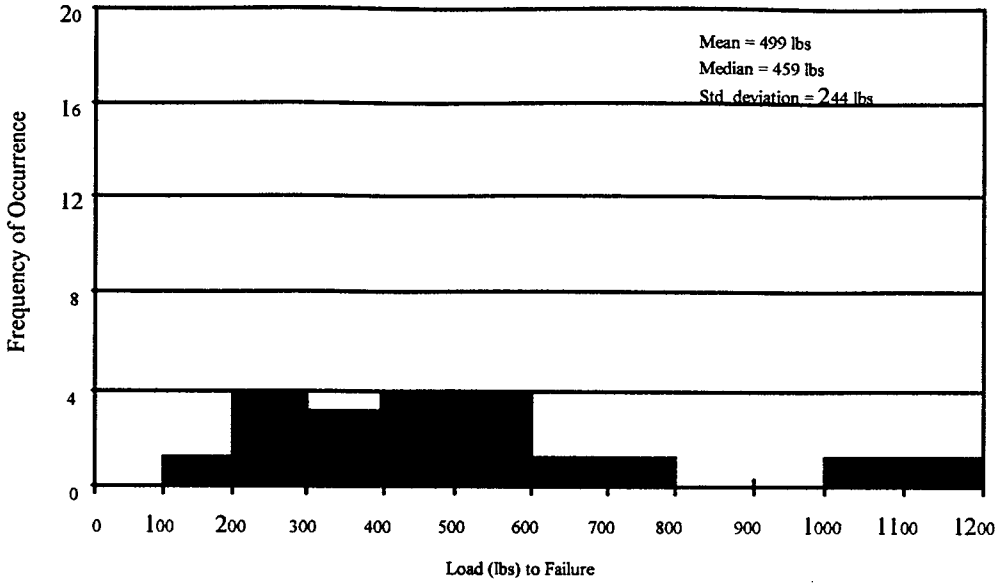

Figure B.5. Histogram from 20 Fracture Tests on 50/125/250 Fiber and 10 mil Diameter Tefzel Mesh

Appendix C
Periodicity Test Procedures

Test Procedure

The procedure for measuring the periodicity and corresponding load value for an optical fiber was as follows. For the initial setup, the center segment of a 1.5 m length of optical fiber was pulled taught across the 0° angle positions on the base plate and epoxied in place (Label [A] in Figure C.1). After the epoxy cured, additional lengths of the same fiber were epoxied approximately one inch on either side of and parallel to the measurement fiber (Label [B] in Figure C.1). These additional fibers allowed the deformer plate to sit flat on the surface of the fiber during testing.

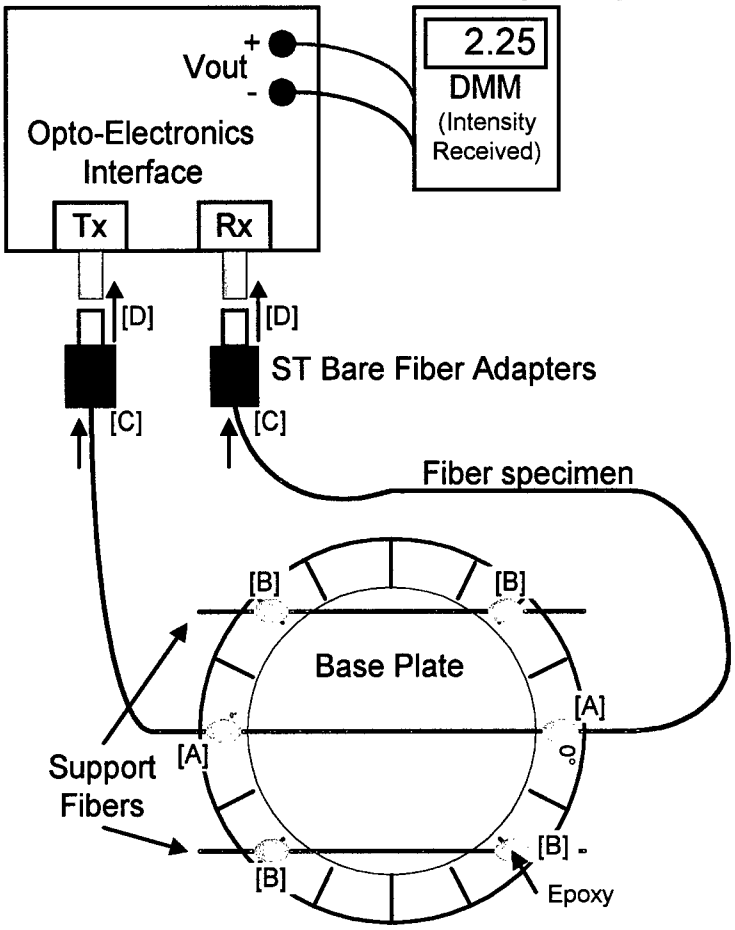

Figure C.1. Setup for Periodicity Testing

After the optical fiber was mounted, the ends of the measurement fiber were stripped, cleaved, and inserted into the ends of the ST bare fiber adapters (Label [C] in Figure C.1). Depending on the fiber cladding size, either the 125 μm or the 240 μm bare fiber adapter was used. Next, the adapters were connected to the opto-electronics interface (Label [D] in Figure C.1). Finally, the base plate was placed on the CBR loading piston, where deformer plate A (or deformer plate B) was then placed on top of the fiber array (as shown in Figure C.1).

The measurement procedure is described in the steps below:

- *Step 1.* Deformer plate A was selected and placed on top of the base plate. It was placed so that the rotation notches on opposite sides of the deformer plate were located such that they matched with the 0° marks on opposite sides of the base plate. At this position, the fiber was orthogonal to the direction of the teeth on the deformer plates (or the minimum periodicity possible for that deformer plate).
- *Step 2.* The initial unloaded light intensity was recorded (in volts read from the DMM).
- *Step 3.* The low speed handle of the CBR machine was slowly rotated until either half of the initial intensity (3dB light loss) or 20 lbs was reached. Measuring the intensity at 20 lbs was designated as the modified procedure. A maximum load of 20 lbs was used to prevent fiber damage.
- *Step 4.* Either the load at half the initial intensity or the intensity if 20 lbs was reached was recorded.
- *Step 5.* The handle was rotated in the opposite direction to release the load from the fiber.
- *Step 6.* The deformer plate was lifted off the fiber and rotated to the next degree increment (0° to 1°, 1° to 2°, etc.)
- *Step 7.* Steps 3 through 6 were repeated until 60° was reached.
- *Step 8.* Steps 1 through 7 were repeated with deformer plate B in place of deformer plate A.
- *Step 9.* The fundamental period for the fiber was determined from the measurement data by finding the angle at which the first minimum load (or minimum intensity if all data was taken at a 20 lb load) was reached.
- *Step 10.* The proper deformer plate at the fundamental angle was placed back on top of the fiber on the base plate.
- *Step 11.* Channel 1 of a digital storage oscilloscope was connected to the voltage output of the load cell indicator, while channel 2 was connected to the voltage output of the opto-electronics interface.
- *Step 12.* The low speed handle of the CBR machine was slowly rotated to increase the load on the fiber while the digital storage oscilloscope recorded the intensity and load in volts. This data was then downloaded to a PC computer where the intensity versus load curve could be graphed for the fundamental period of the particular fiber specimen.
- *Step 13.* The initial setup procedure and steps 1 through 12 were repeated for each of the 11 fiber specimens.

This measurement procedure worked well with the Corning graded index, acrylate coated fibers. However, for the gold and polyimide coated fibers, half of the initial light intensity could not be reached at less than 20 lbs (Step 3 above) so the modified procedure was used for the whole test. Twenty pounds was designated after as the "do not exceed" load for the optical fibers under test. With only the intensity data at 20 lbs a plot of intensity loss versus period would still show the peaks of sensitivity.

An additional problem was encountered with the step index fiber. Due to the variable spatial dependence of mode coupling in step index fibers the intensity changes were very small. Therefore, the modified procedure was used with the step index fibers.

Appendix D
Single and Double-Sided Microbend Deformer Test Procedures

Single and Double-Sided Microbend Deformer Experimental Procedure

The procedure for the double-sided deformer test was as follows:

- *Step 1.* The top deformer was glued to the bottom of a flat round plate attached to the underside of the load cell in a CBR (California Bearing Ratio) unconfined compression machine.
- *Step 2.* A single length of fiber 2 meters long was taken and pulled taught across the bottom deformers. On either side of the deformers, the fiber was held in place with a piece of clear tape. The fiber was not under tension.
- *Step 3.* The bottom plate was placed on top of the load plate of the CBR machine, and aligned so that the top deformers interleaved the bottom deformers.
- *Step 4.* The ends of the fiber were stripped, cleaved, and inserted into adapters that connected to the opto-electronics interface.
- *Step 5.* A DMM (digital multimeter) was connected to the opto-electronics interface to monitor the light intensity.
- *Step 6.* A dial indicator with 0.0001-inch resolution was placed to touch the loading plate of the CBR machine close to the bottom deformer base.
- *Step 7.* The slow handle of the CBR was rotated just until the fiber contacted both sides of deformers but was not under strain.
- *Step 8.* The dial indicator was zeroed. Initial light intensity was recorded.
- *Step 9.* The slow handle was rotated in increments of 1 mil on the dial indicator. At each mark, a voice recorder was used to record the load, light intensity, and displacement.
- *Step 10.* Step 9 was repeated until the light intensity stopped decreasing with displacement.
- *Step 11.* Steps 2 through 10 were repeated for each fiber under test.

For the single-sided deformer test, the above procedure was slightly modified. Listed below are the steps for this test.

- *Step 1.* A polished aluminum bar with the same approximate dimensions as the top deformer without deformers was glued to the bottom of the round plate.
- *Step 2.* Unchanged
- *Step 3.* The top plate was aligned with the center of the polished aluminum bar.
- *Steps 4-6.* Unchanged
- *Step 7.* The slow handle of the CBR was rotated until the fiber just contacted the flat plate but was under no measurable strain.
- *Steps 8-11.* Unchanged.

Results of the Single and Double-Sided Microbend Deformer Experiment

The intensity versus load curves for the acrylate and polyimide of fibers in the two type of microbend deformers are presented in Figure D.1.

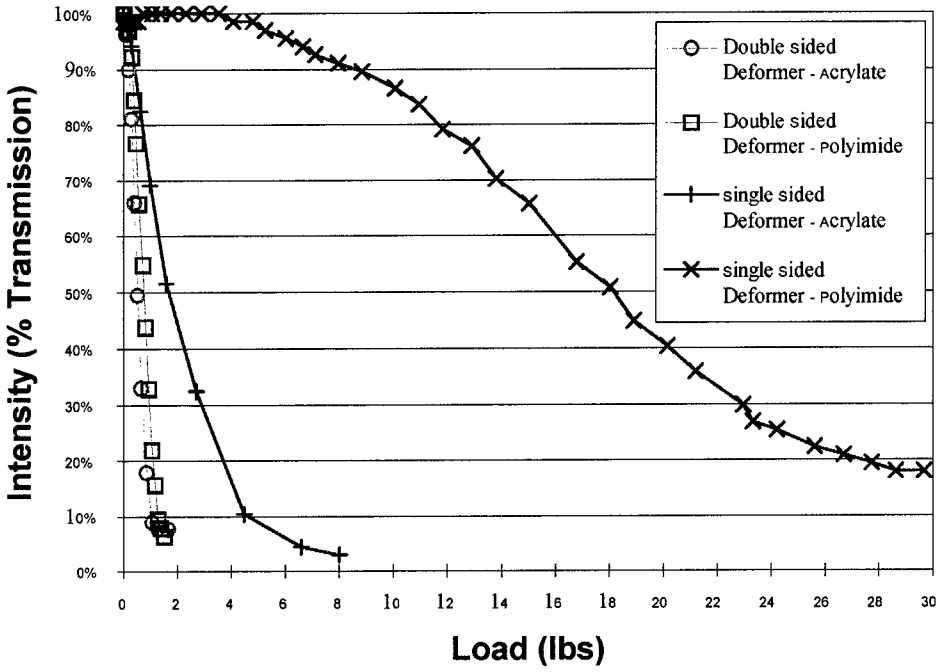

Figure D.1. Intensity versus Load for the Polyimide and Acrylate Coated Fibers in the Single and Double-Sided Microbend Deformers

For both fibers in the double-sided deformers, the intensity loss curve was nearly the same and was at a very small load (just under 1 lb at 50% intensity). Both curves exhibited quick intensity loss as soon as a load was applied, decreasing in a linear fashion to about 20% intensity transmission. The intensity loss curves for the single-sided deformers, however, were different from the double-sided deformers. For the acrylate coated fiber, the curve decreased in an exponential manner as soon as the load was applied to nearly zero light intensity transmission. For the polyimide coated fiber the intensity did not begin to decrease until nearly 4 lbs of load was applied, after which it decreased with varying slope, leveling off at about 18% intensity transmission around 29 lbs. From Figure D.1 it can be concluded that fibers in the double-sided deformers are more sensitive and have a greater linearity than those in the single-sided deformers.

The intensity versus displacement for the four combinations of fibers/deformers is presented in Figure D.2.

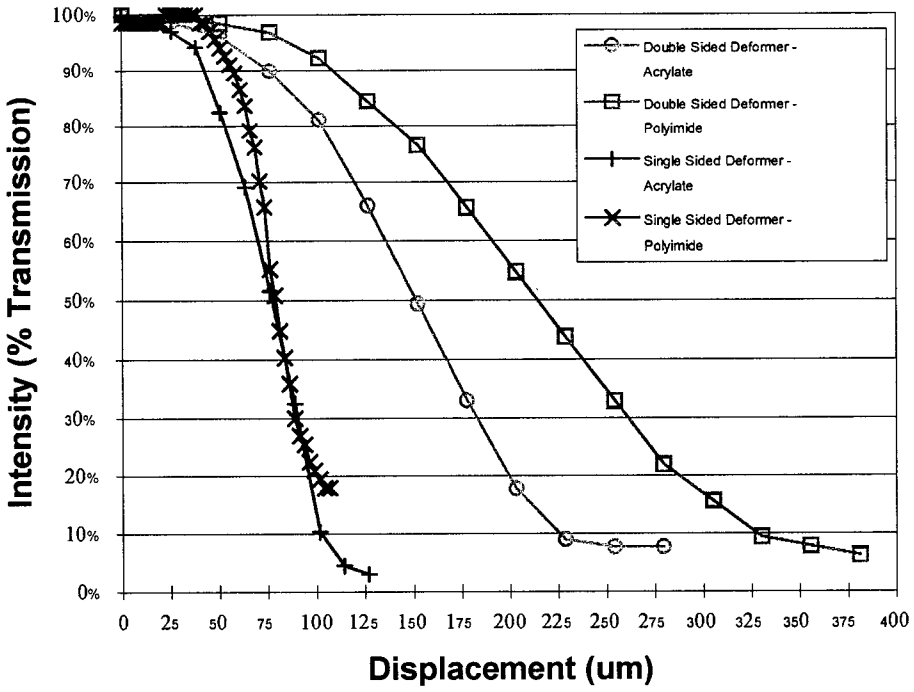

Figure D.2. Intensity versus Displacement for the Polyimide and Acrylate Coated Fibers in the Single and Double-Sided Microbend Deformers

The intensity versus displacement for both fibers in the double-sided deformers and the acrylate fiber in the single-sided deformer exhibited the same shape with varying degrees of magnitude in displacement. For the polyimide fiber in the single-sided deformer, though, the intensity drop, once it began, occurred over a smaller displacement range than the other combinations (about 40 μm from 90% to 20% intensity transmission). It appears that fibers in the double-sided deformers can traverse a much greater displacement than those in the single-sided deformers. However, changes in the spatial wavelength and deformer diameter/shape of the double-sided mechanism could vary as to how much displacement the fiber may undergo, which in turn affects the amount of intensity loss that may occur. The same statement may also be made about the design of the single-sided deformers.

Table D.1 summarizes several of the characteristics of the different combinations of fibers and deformers extracted from Figure D.1 and Figure D.2 .

Table D.1. Load and Displacement Characteristics for the Four Fiber/Microbend Inducing Combinations

Fiber	Deformer Type	Load at 50% Intensity (lbs)	Change in Load from 90% to 20% Intensity (lbs)	Displacement at 50% Intensity (μm)	Change in Displacement from 90% to 20% Intensity (μm)
Acrylate	Double-Sided	0.6	0.6	150	125
Polyimide	Double-Sided	0.9	0.7	215	175
Acrylate	Single-Sided	1.7	3.4	76	50
Polyimide	Single-Sided	18.2	19	78	40

The load versus displacement for the optical fibers was also obtained from this experiment. In order to generate a comparison for this data, the coating from a piece of acrylate coated fiber was removed, leaving the bare silica core/cladding, which was put into the two deformer mechanisms and loaded as described in the procedures previously. For the double-sided deformers, Figure D.3 shows that bare and polyimide coated fibers have a linear relationship in the loaded data range. However, the acrylate fiber exhibited an exponentially increasing relationship.

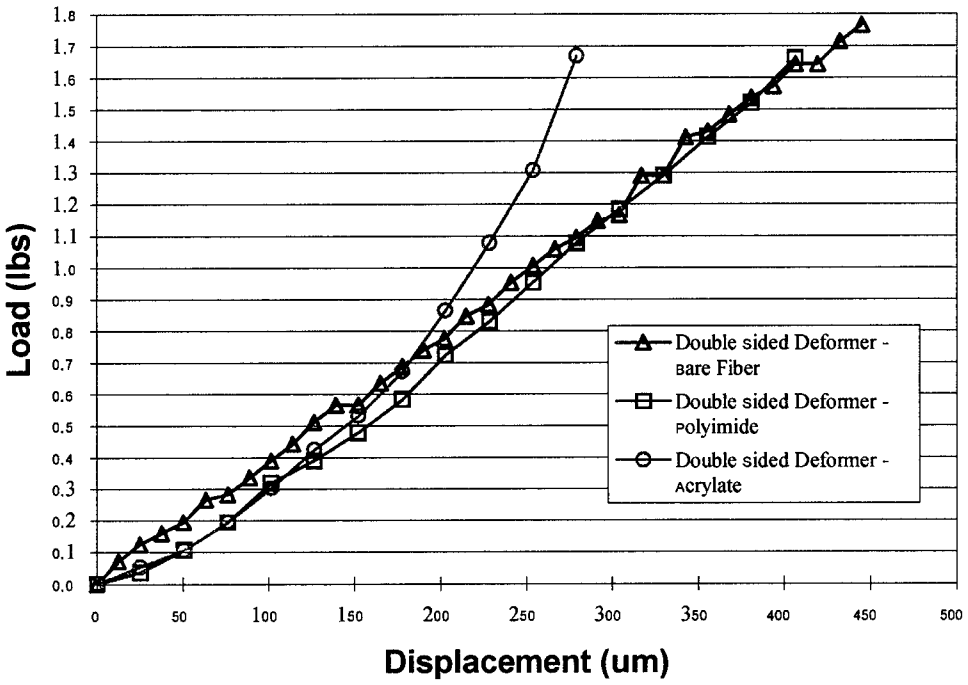

Figure D.3. Load versus Displacement for Three Fibers Subjected to Double-Sided Microbend Deformers

Figure D.4 shows the load versus displacement for the single-sided deformers. The acrylate coated fiber absorbed a much larger displacement at a smaller load than either the polyimide or the bare fibers. The thick acrylate coating surrounding the silica core/cladding region was soft and gave way under the load from the deformers. The thickness of the acrylate coating was 62.5 μm around the silica, while the thickness of the polyimide coating was only 10 μm around the silica.

The bare fiber in Figure D.4 fractured at about 45μm displacement. The coated polyimide fiber did not break over the displacement range (110μm). This shows how the coating helps to protect a fiber in microbending.

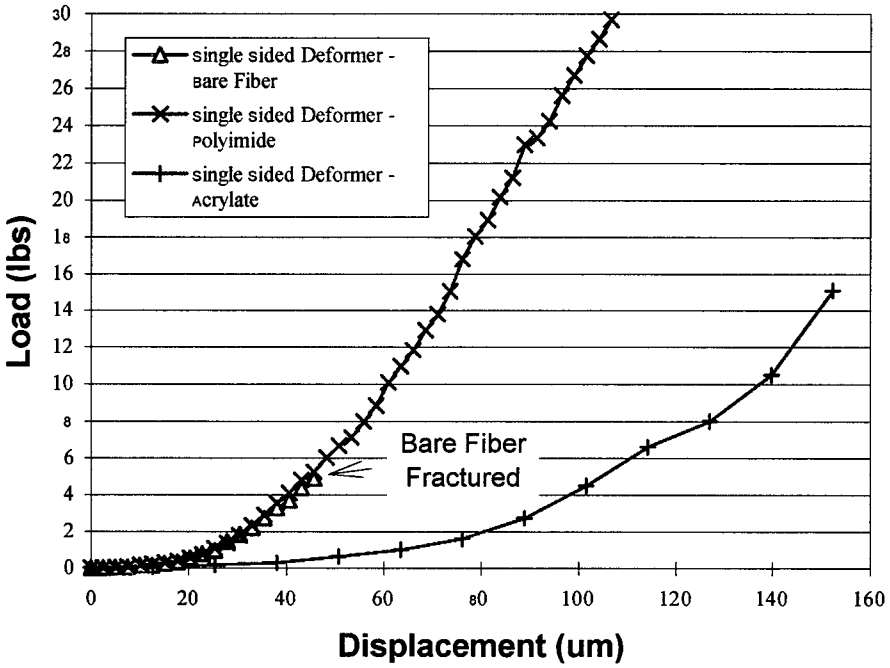

Figure D.4. Load versus Displacement for Three Fibers Subjected to Single-Sided Microbend Deformers

Appendix E
Intensity vs. Static Load

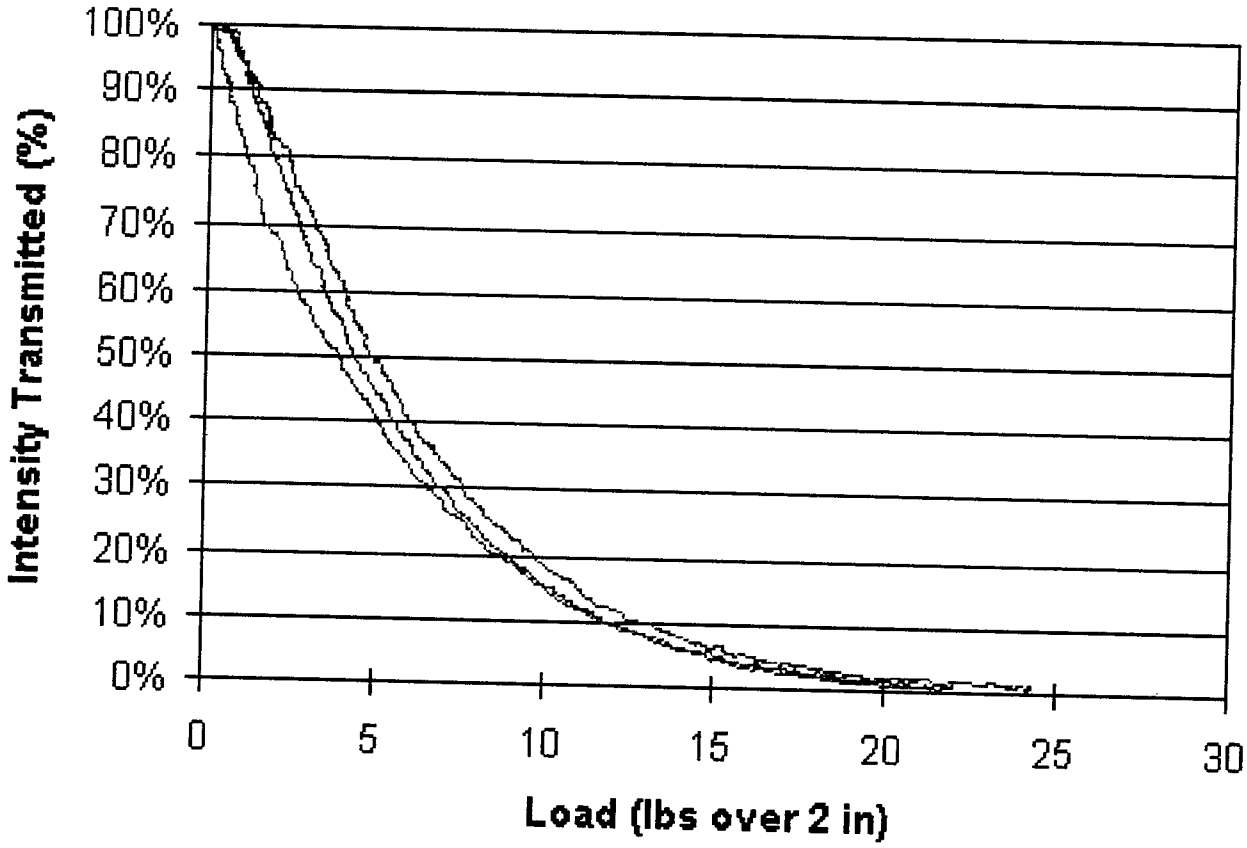

Figure E.1 Corning 62.5/125/250 with Nylon Mesh (24.7 x 25.1 opi)

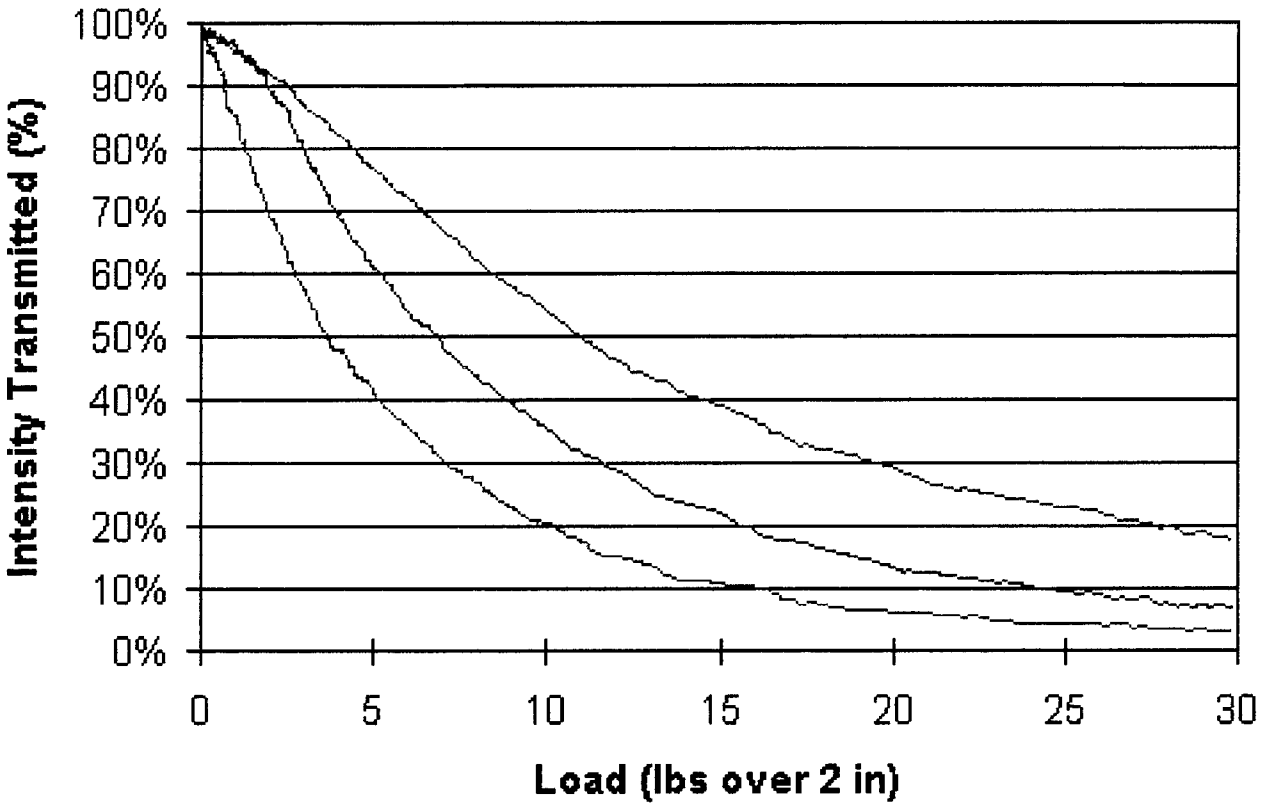

Figure E.2 Corning 50/125/250 with Polypropylene Mesh (24 x 20 opi)

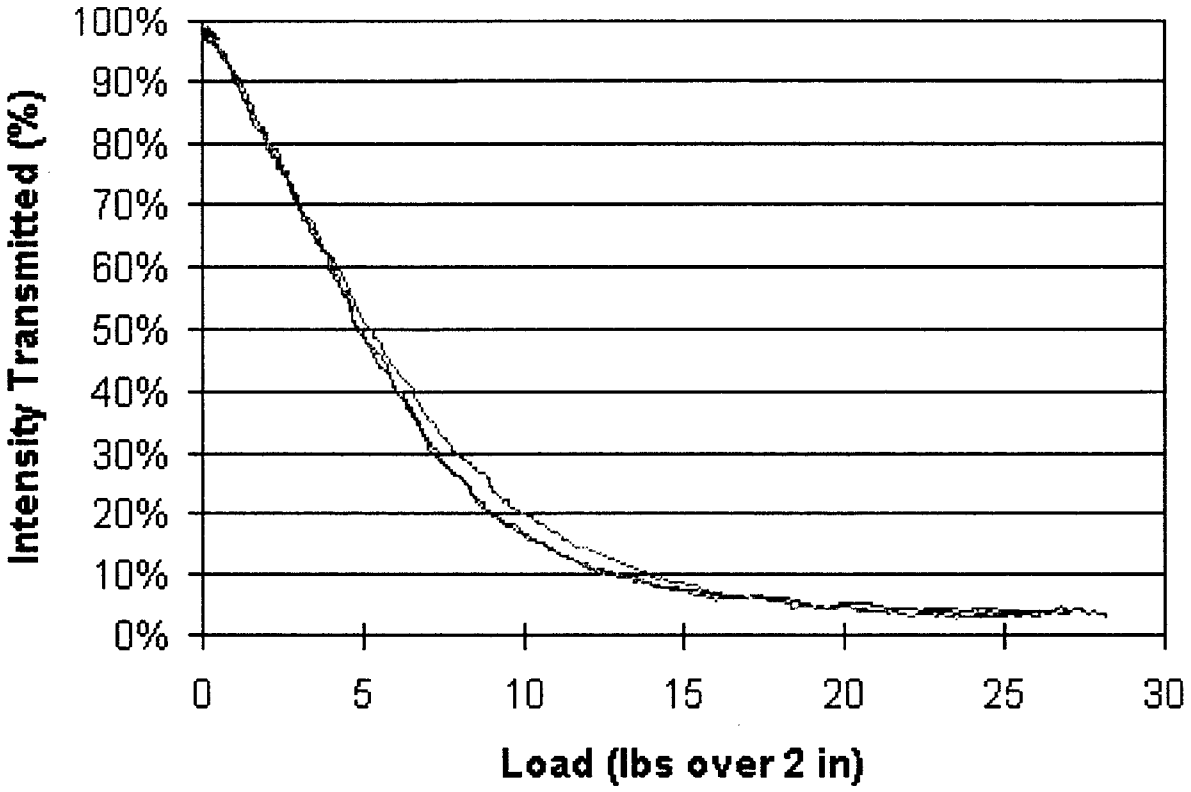

Figure E.3 Corning 62.5/125/250 with Polypropylene Mesh (24 x 20 opi)

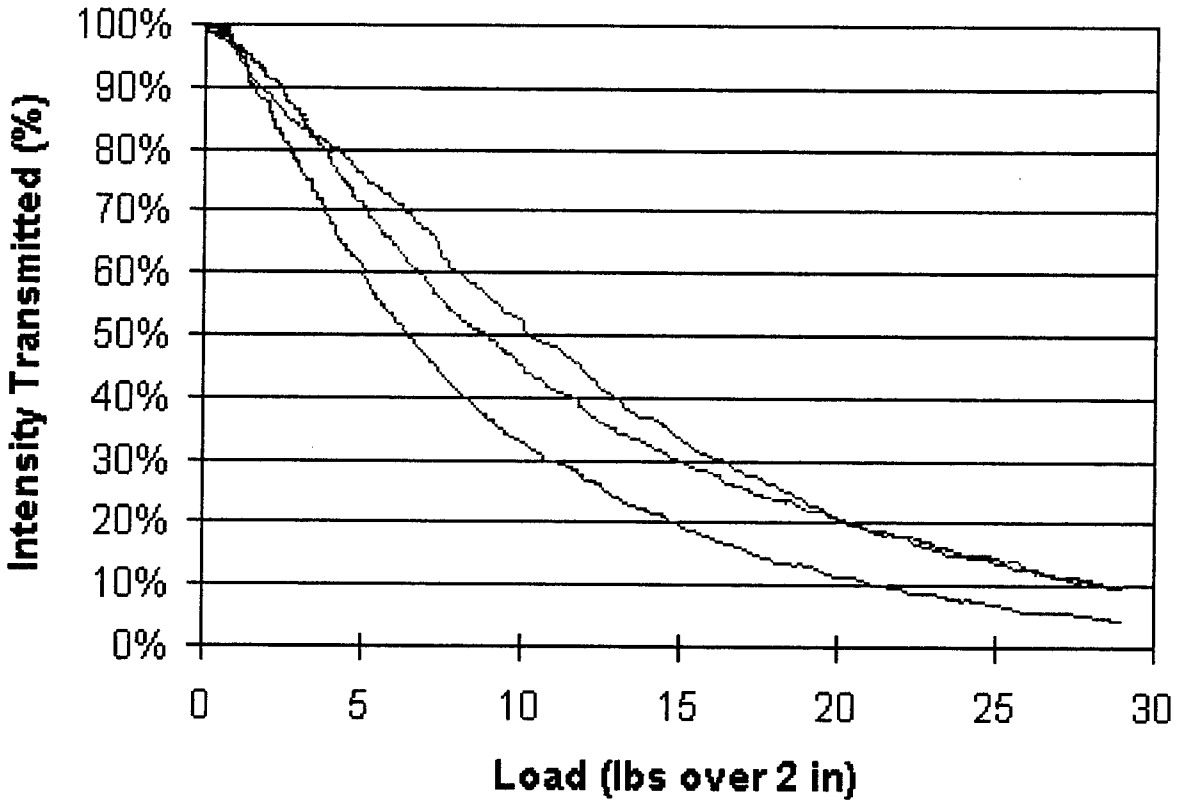

Figure E.4 Corning 50/125/250 with Plypropylene Mesh (23 x 23 opi)

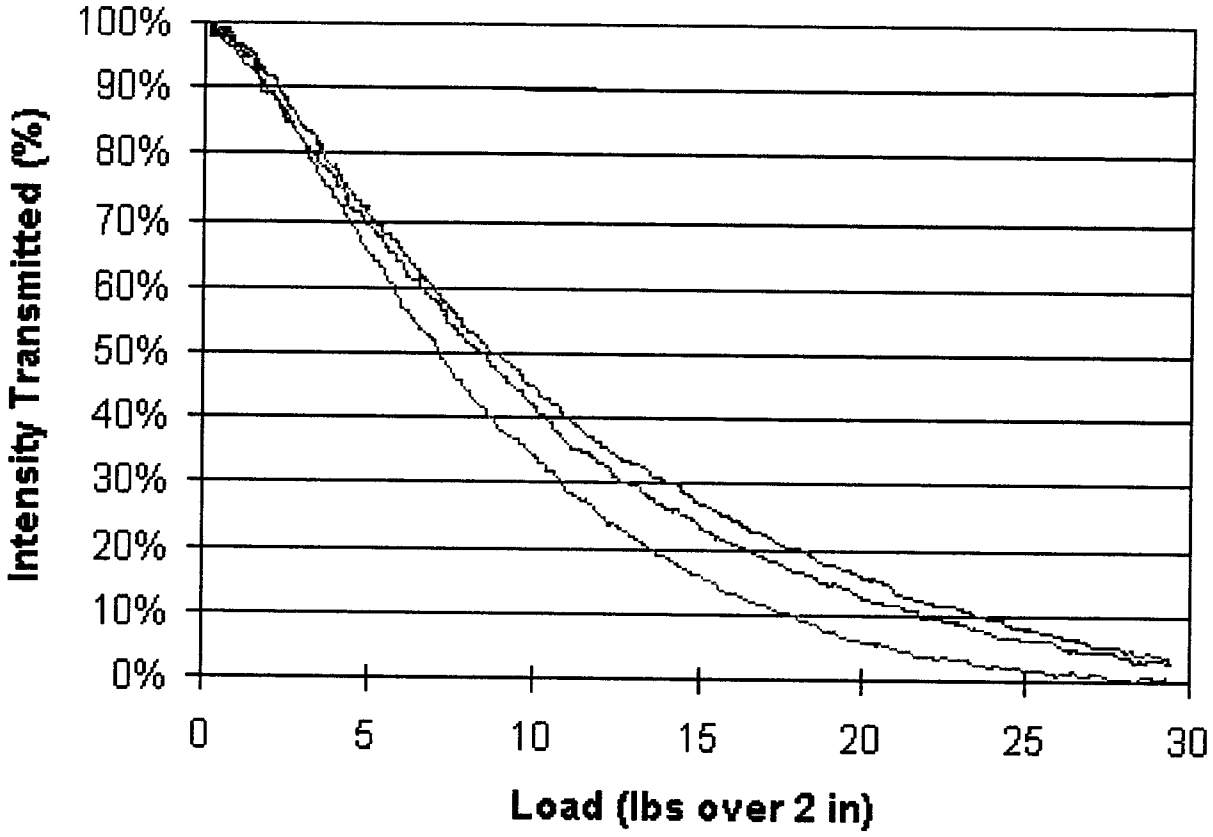

Figure E.5 Corning 62.5/125/250 with Polypropylene Mesh (23 x 23 opi)

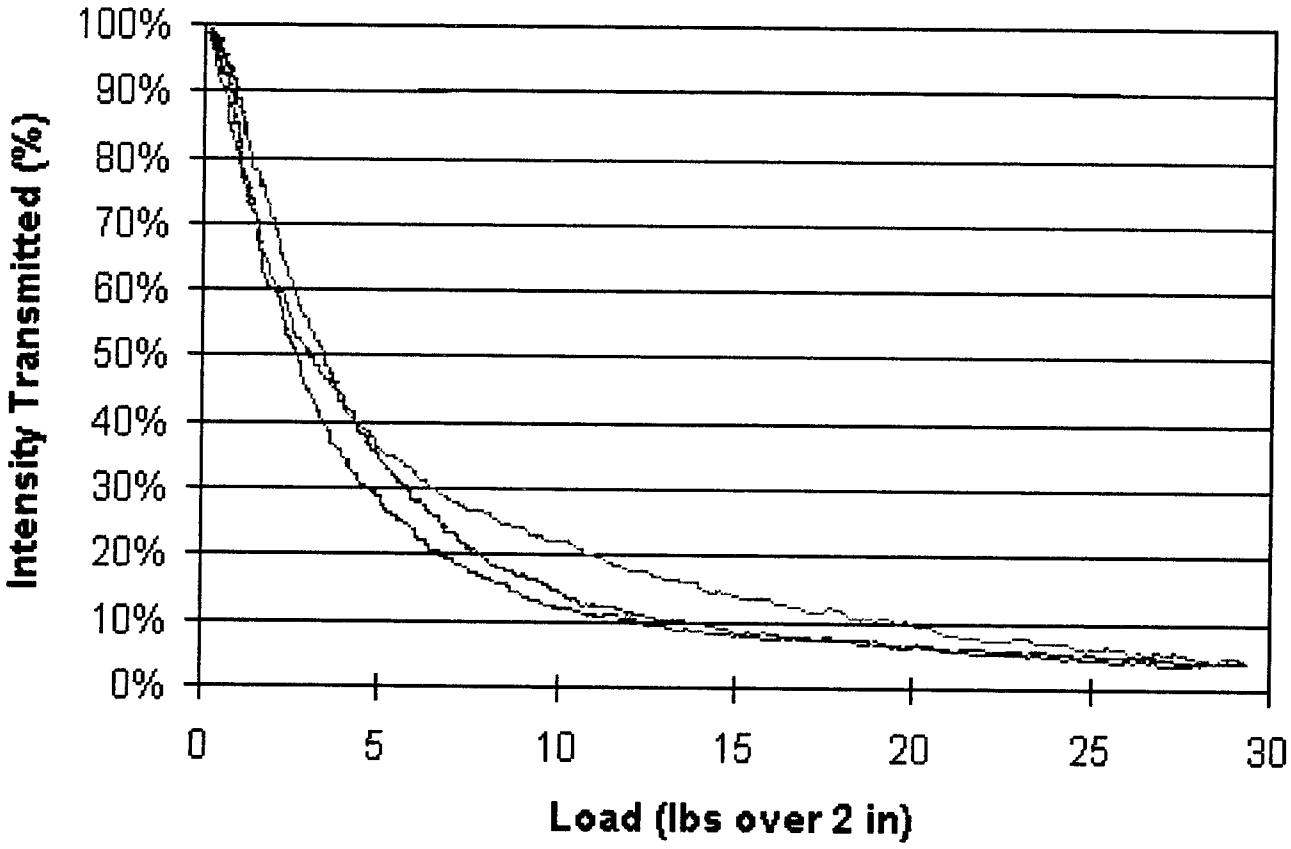

Figure E.6 Corning 50/125/250 with Tefzel Mesh (23.5 x 23.5 opi)

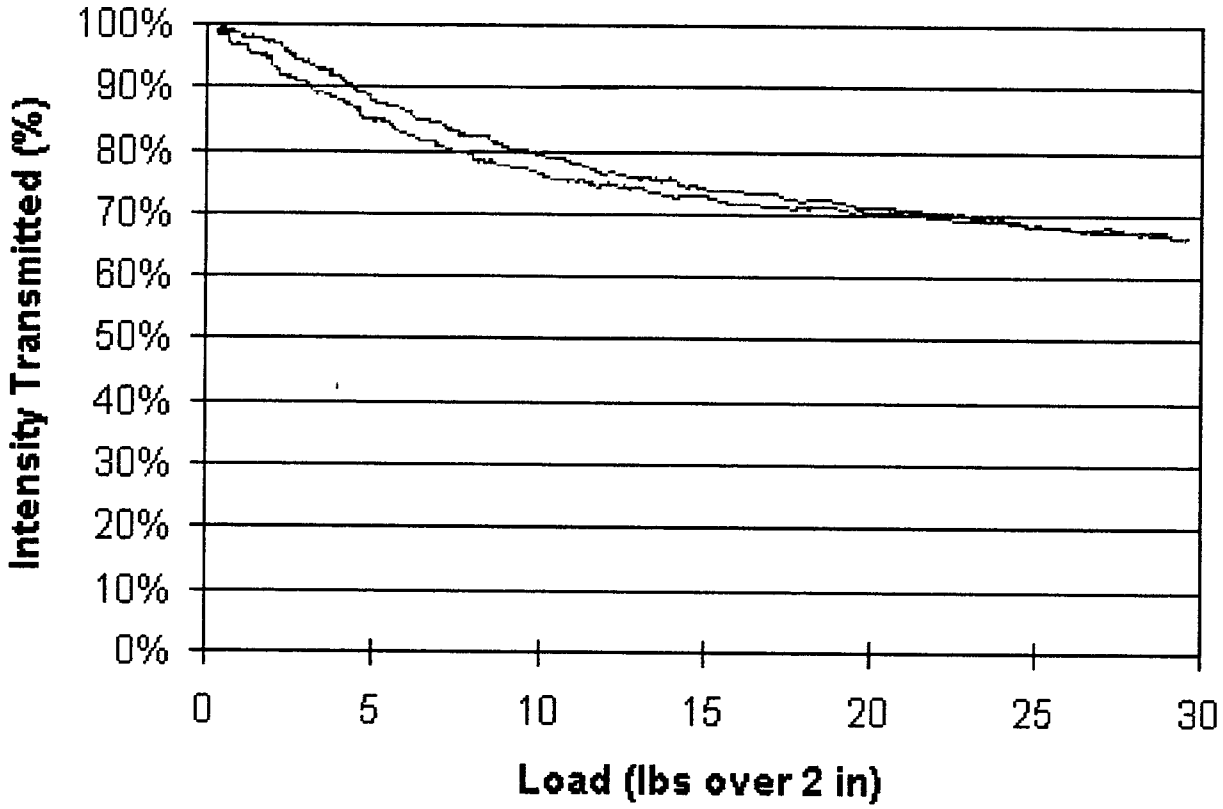

Figure E.7 Corning 62.5/125/250 with Tefzel Mesh (23.5 x 23.5 opi)

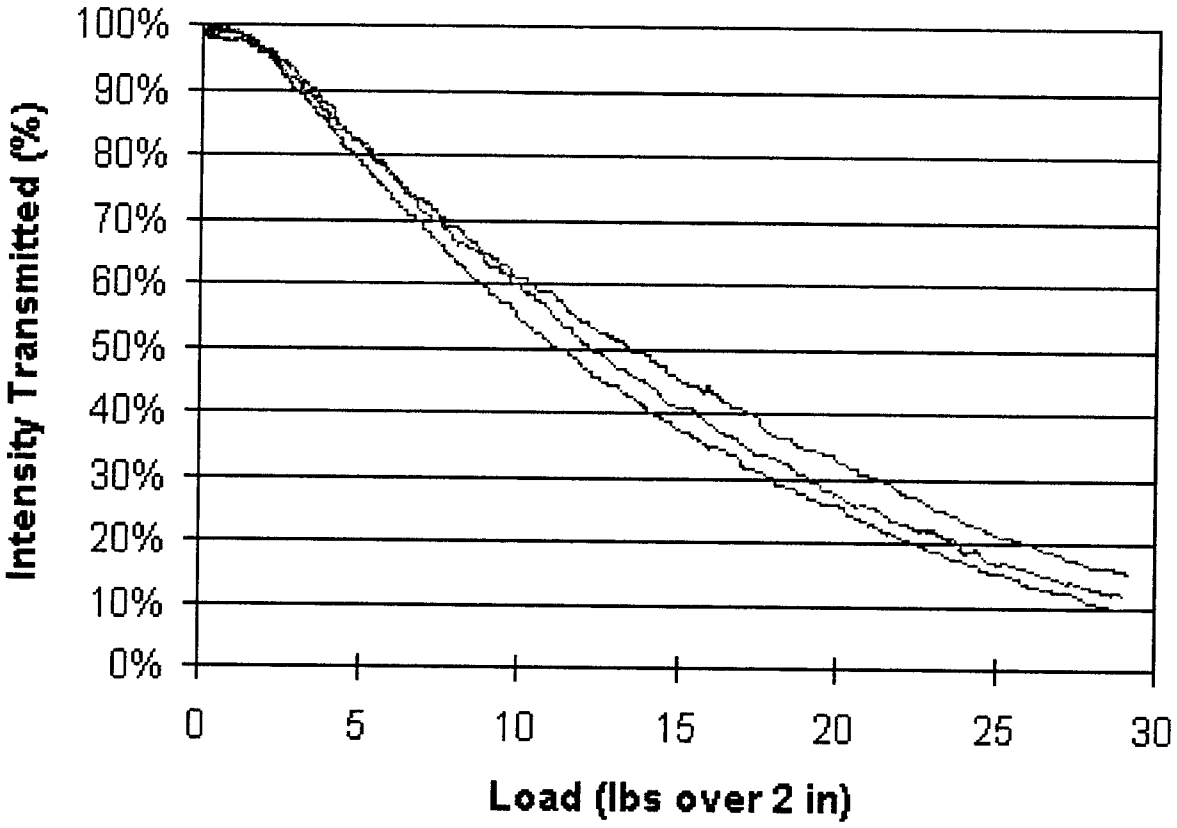

Figure E.8 Corning 50/125/250 with Nylon Mesh (24.7 x 25.1 opi)

Appendix F
Field Installation Procedure

This installation procedure can be followed for both flexible and rigid pavements; however, it has only been performed in flexible pavements to date. The following tasks must be performed prior to the installation process.

- Sensor constructed to desired length with lead-in and lead-out fibers of the desirable length for installation at the chosen site.
- Sensor laboratory evaluation to determine load versus intensity and intensity variations versus length.
- Pavement has been marked with the location(s) of the sensor(s) to be installed.
- All equipment has been obtained and ready for use, including for example street signs, lights if necessary, saws, heaters, epoxies, levels, scopes, etc.
- All installation materials are obtained and ready for use.
- Asphalt is thoroughly heated to a liquid state for pouring.
- Screeding tool is set to desired depth (Figure F.1). (Sensor thickness is added to the depth of the screeding tool to place the top of the sensor at the desired depth.)
- Lead-in and lead-out grooves have been cut for the fiber and conduit has been placed for fiber routing to the electrical cabinet.

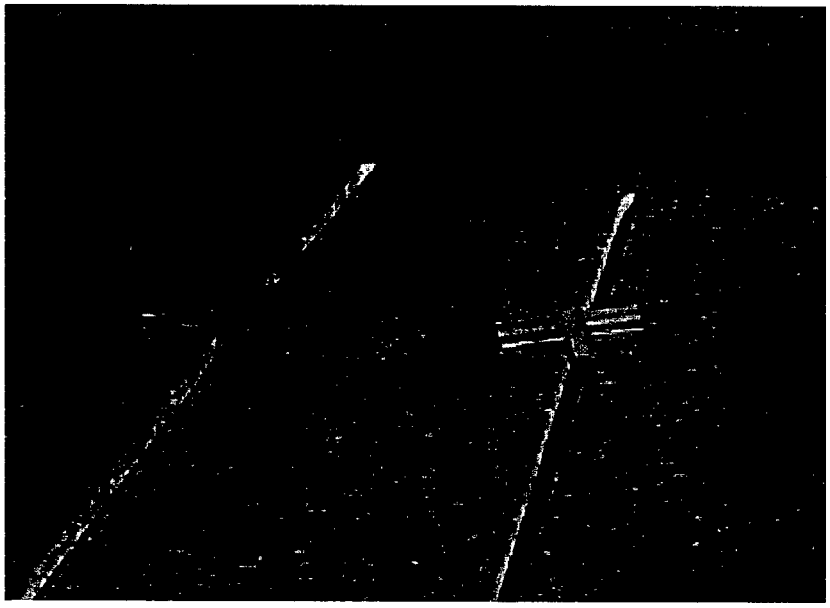

Figure F.1. Cross-section of Screeding Tool Used to Level G100 in Pavement Groove

The procedure for fiber optic sensor installation can now begin.

- *Step 1.* Stack two asphalt cutting blades onto the street saw (two 3/16" blades for 3/8" groove).

- *Step 2.* Start street saw, align blades over the beginning of sensor groove location, and crank handle to lower blade to desired total groove depth (usually about 1"), not to be confused with sensor groove depth.

- *Step 3.* Slowly move saw in a straight line along the sensor groove marking, being sure to only make a single pass. Stop at the end of the marking and raise saw blade.

- *Step 4.* Make any adjustments to groove width at the position in the groove where the loop end of the sensor will be located. It may need to be widened with a circular saw by 1/8" on either side to fit the loop.

- *Step 5.* Follow steps 1 through 4 for additional sensor grooves. All grooves that are located a few feet from one another should be cut prior to sensor installation, so contamination of the sensor in the groove before being covered by asphalt does not occur.

- *Step 6.* Clean out the groove with compressed air.

- *Step 7.* Place fiber-optic sensor in the groove to ensure it fits (Figure F.2). Make any adjustments to the groove.

Figure F.2. Placing Microbend Sensor Into Pavement Groove to Ensure Proper Fit

- *Step 8.* Mix G100 according to manufacturers instructions. Fill groove to approximate depth of sensor.

- *Step 9.* Using the screeding tool, screed out the G100 in the groove so that a flat base of G100 remains in the groove. Fill in any gaps with G100 to level out and screed again.

- *Step 10.* Place fiber-optic sensor flat into the groove. Do not push sensor into the G100, but make sure that the sensor is contacting the G100 along its entire length.

- *Step 11.* Place G100 over the loop end and entrance end of the sensor. Screed it level with the surface of the pavement. This process will protect those areas of the sensors from loading.

- *Step 12.* Wait for the G100 to set, 30 minutes to 1 hour. During this time, the lead-in and lead-out fibers can be placed into a lead in/out groove or pulled through conduit to the equipment box.

- *Step 13.* After the G100 sets, slowly pour the hot roofing asphalt into the groove. Pour enough so that it is above the surface of the pavement. During cooling, a small amount will recede into the groove.

- *Step 14.* After the roofing asphalt is cool to the touch and soft but solid (about 5-10 minutes), use a metal, flat scraper approximately 2-inches wider than the groove to cut the top of the asphalt from the groove to make it level with the surface of the pavement. It will be easier to do if one person pulls the cut asphalt while another cuts the remaining asphalt.

- *Step 15.* Once installation is complete, test the sensor to make sure it works.

Appendix G
Field Data Acquisition Software Description

MULTIPLE WAVEFORM ACQUISITION

Multiple, simultaneous waveform acquisition was accomplished by using a data acquisition card on a laptop computer controlled with custom designed LabVIEW VI (virtual instrument). The data acquisition card was National Instruments DAQCard-1200, a multifunction I/O card with analog inputs for PCMCIA. This card has a fast sampling rate (100kS/s), 8 analog input channels, and external trigger input. The 8 analog input channels meant that at most 8 sensors could be monitored simultaneously. If monitoring more than one channel, the maximum sampling rate per channel would be the maximum sampling rate for the card (100kS/s) divided by the number of channels monitored (i.e., if four analog inputs were selected, the sample rate per channel could at most be 100kS/4 or 25kS/s). The external trigger input allowed a TTL (digital) signal from the opto-electronics interface to tell the card when to start the analog input channel(s) signal acquisition, allowing autonomous acquisitions in some cases.

The laptop computer was a Toshiba Satellite™ T1960CS 486DX-50 running Windows®95 and the software used for the instrumentation development was LabVIEW® version 4.0 for Windows®95. LabVIEW allows the programmer to design a graphical front panel simulating a piece of equipment (such as an oscilloscope, voltmeter, signal conditioner, etc.) and then go behind the front panel and use functional blocks to control signal conditioning and system I/O. The simulation of the instrument in software is the reason it is called a virtual instrument (VI).

The design of the multiple waveform acquisition instrument had several basic components. Figure G.1 shows the graphical interface designed for this instrument. The primary controls for the system included acquisition channels, duration of acquisition, samples per second, input limits, description of data to be acquired, manual trigger start, and timer configurations (typical values are displayed on the front panel in Figure G.1). The timer configurations allowed the user to program the VI to acquire data in set intervals for autonomous data capture.

The settings on this interface were fed into the software to control the data acquisition card for capture and display of the analog inputs. The display of captured input voltages was on the graph in the upper-right corner where the y-axis is volts and the x-axis is the sample number. The combination of these components allowed the user to make an acquisition from the analog input channel(s) and then see the results directly on the screen. What is not shown, however, is the prompt where the user is asked to give a filename to save the data. Upon executing the VI, the user is prompted if they wish to save the data to a text file. The user may then choose to do so and enters a filename, where they can later find the voltages acquired during that execution, separated by acquisition reference numbers.

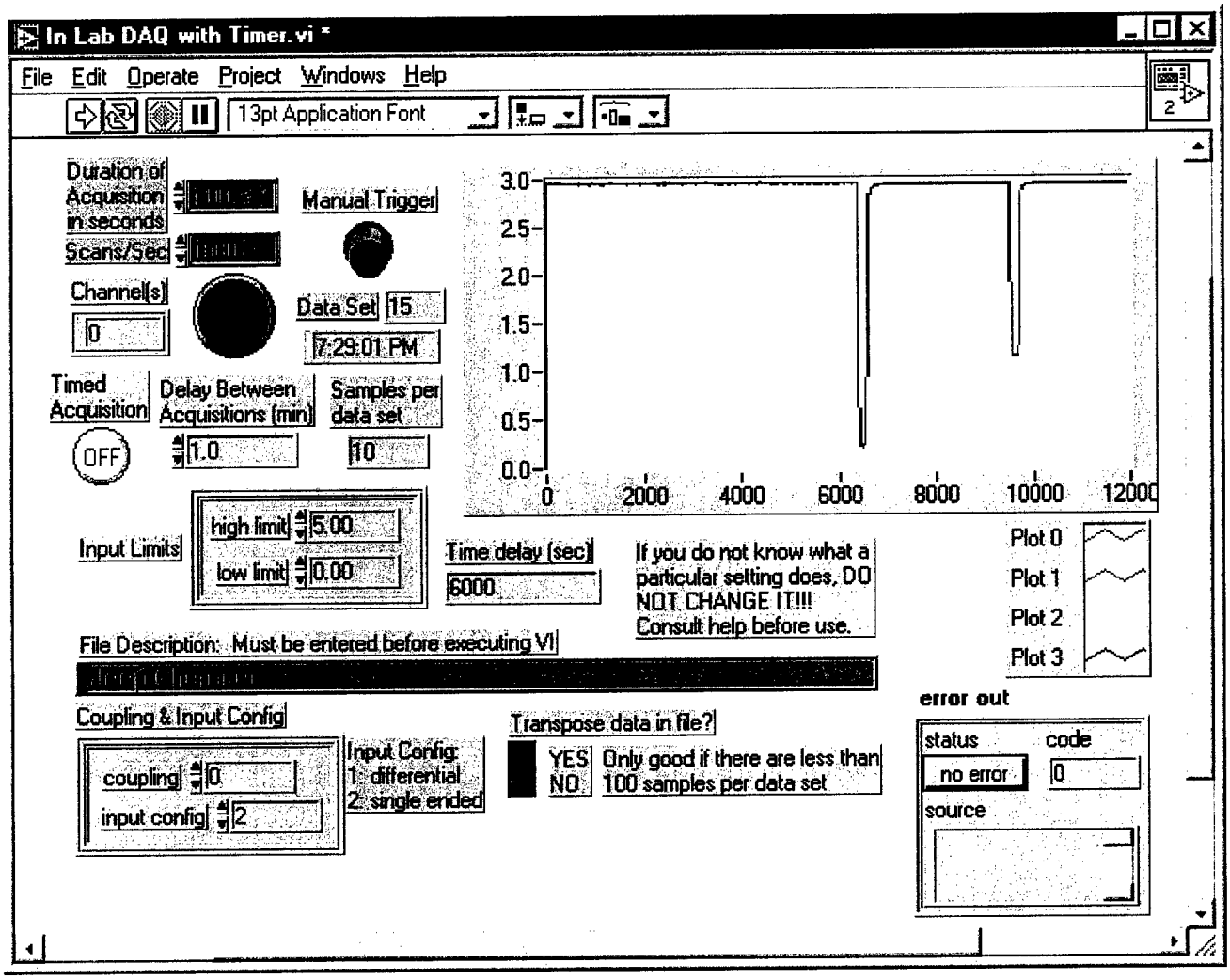

Figure G.1. LabVIEW VI Interface for Multiple Waveform Acquisitions

WAVEFORM VIEW AND SAVE

The multiple waveform acquisition is complemented with a VI that allows the user to open the data file created with the multiple waveform acquisition VI and serially parse through each of the individual data sets and columns contained in each data set. The front panel for this VI is shown in Figure G.2. To begin, the user executes the VI and is prompted to enter the filename of the data (Figure G.3). To view the first set of data, the *Process New Data* button (green) in the stoplight looking controls is pushed (Figure G.4). This brings up another window from which the signal can be zoomed and measured (Figure G.5). After viewing the waveform, the user can select to save the waveform and exit or exit without saving. The saved waveform is written to the file listed in the *Condensed File Path* box with a label noting the data set and column where it was located. The original front panel then returns and the user can select to view another (or the same) column from the same data set (*Process Current Data Again* button (yellow) and *Column Select*), *Process New Data*, or *Exit the Program* (red button) (Figure G.6).

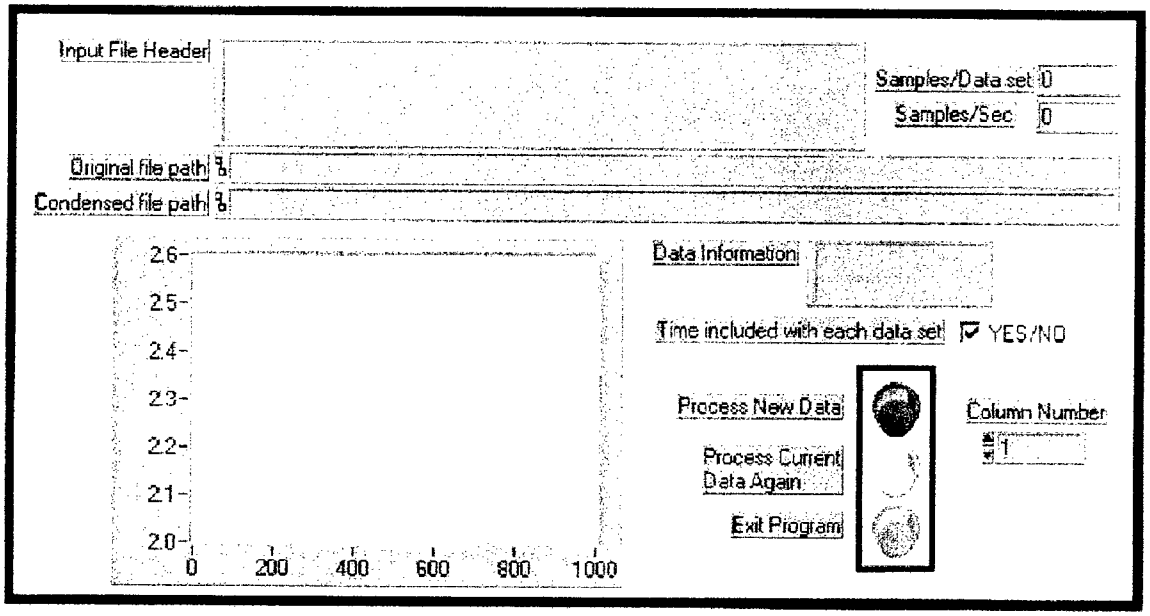

Figure G.2. LabVIEW VI Interface for Waveform View and Save Prior to Execution

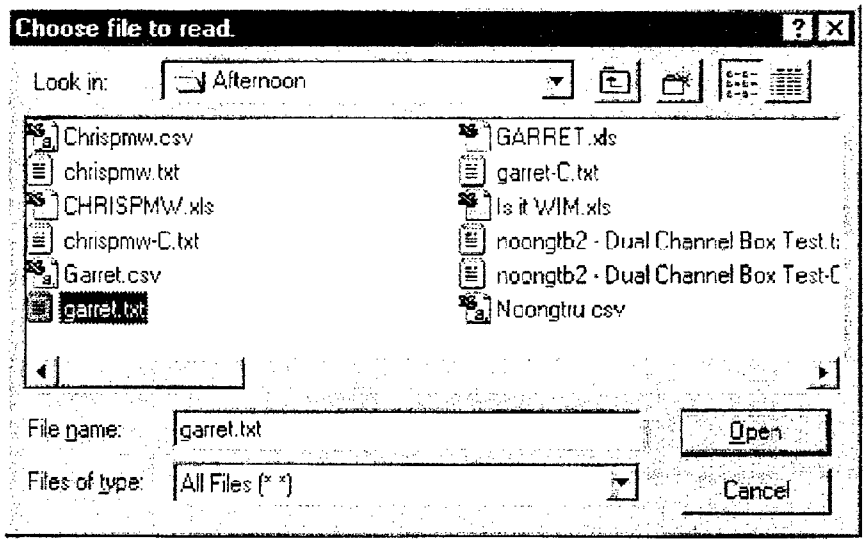

Figure G.3. LabVIEW VI Interface for Prompt for Data Input File

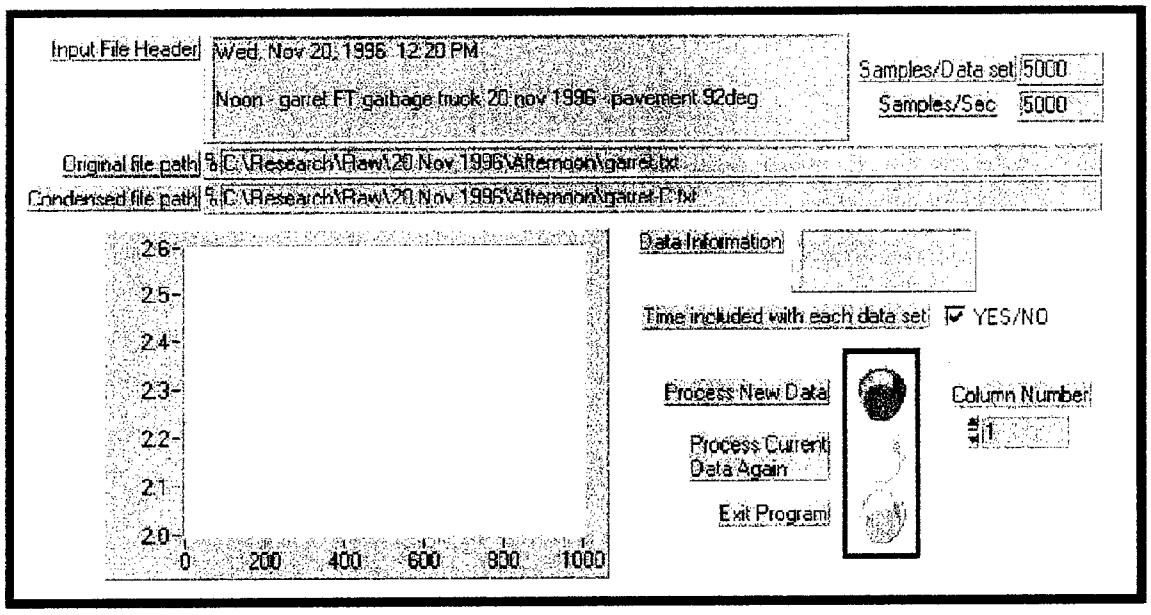

Figure G.4. LabVIEW VI Interface for Waveform View and Save Waiting to Load First Data Set

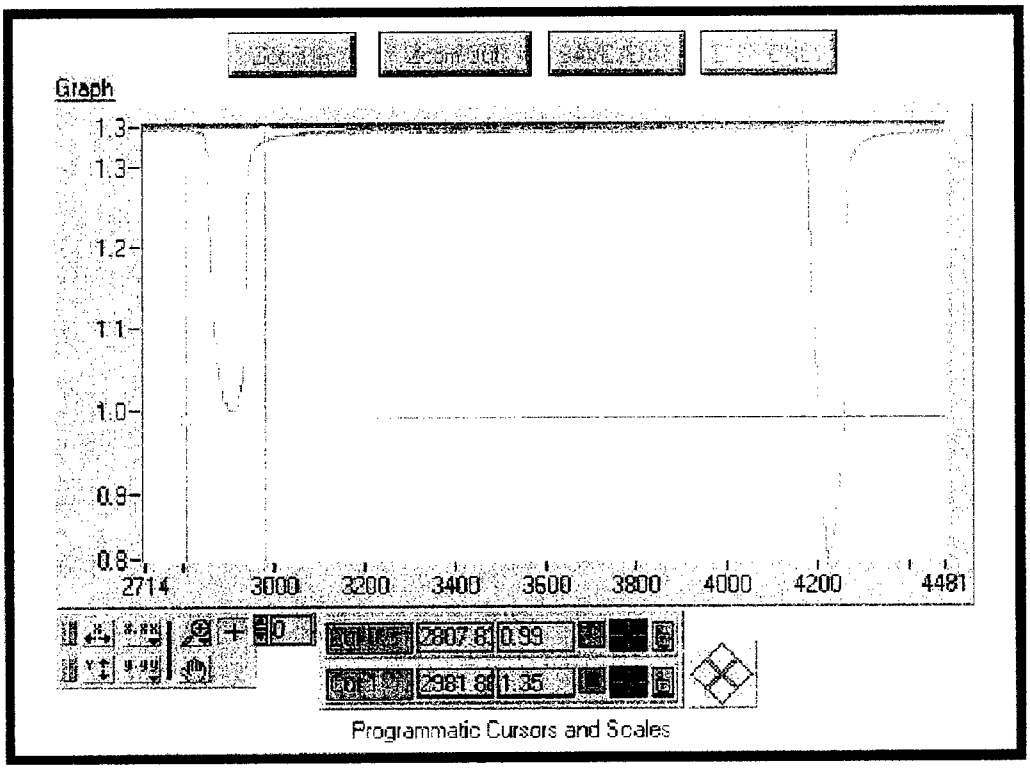

Figure G.5. LabVIEW VI Interface for Zoom, Measurement, Save and Exit Window

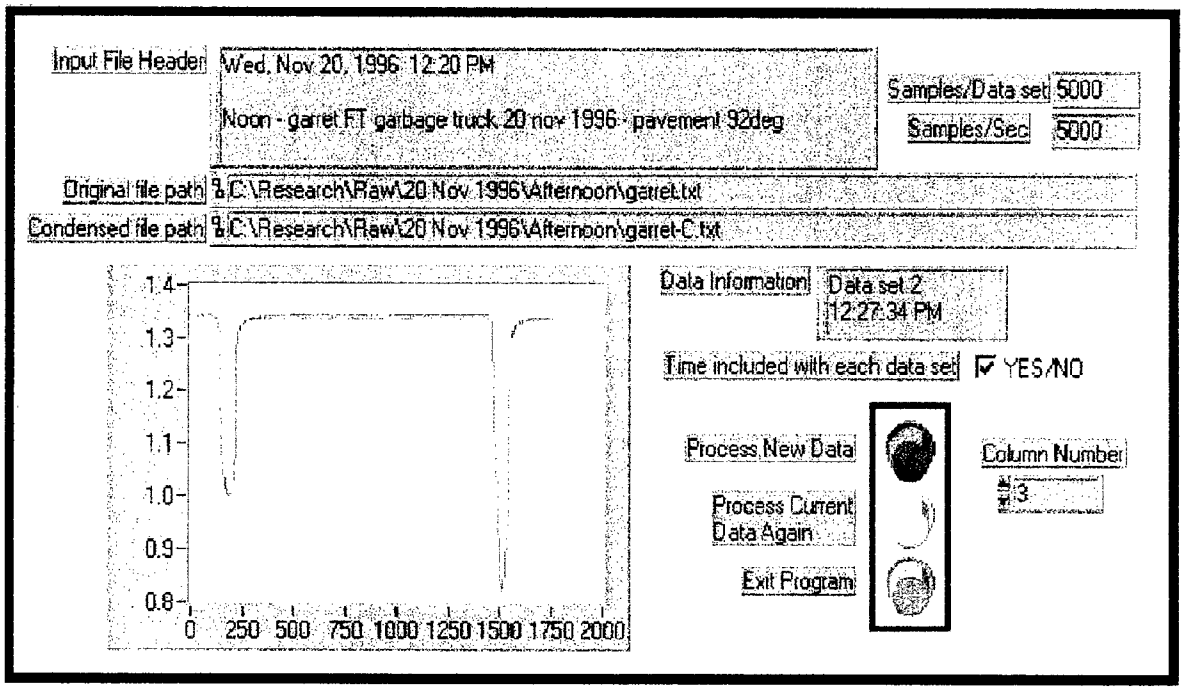

Figure G.6. LabVIEW VI Interface for Waveform View and Save for Selection of Different Column

Reproduced by NTIS

National Technical Information Service
Springfield, VA 22161

This report was printed specifically for your order from nearly 3 million titles available in our collection.

For economy and efficiency, NTIS does not maintain stock of its vast collection of technical reports. Rather, most documents are printed for each order. Documents that are not in electronic format are reproduced from master archival copies and are the best possible reproductions available. If you have any questions concerning this document or any order you have placed with NTIS, please call our Customer Service Department at (703) 605-6050.

About NTIS

NTIS collects scientific, technical, engineering, and business related information — then organizes, maintains, and disseminates that information in a variety of formats — from microfiche to online services. The NTIS collection of nearly 3 million titles includes reports describing research conducted or sponsored by federal agencies and their contractors; statistical and business information; U.S. military publications; multimedia/training products; computer software and electronic databases developed by federal agencies; training tools; and technical reports prepared by research organizations worldwide. Approximately 100,000 *new* titles are added and indexed into the NTIS collection annually.

For more information about NTIS products and services, call NTIS at 1-800-553-NTIS (6847) or (703) 605-6000 and request the free *NTIS Products Catalog,* PR-827LPG, or visit the NTIS Web site **http://www.ntis.gov**.

NTIS
Your indispensable resource for government-sponsored information—U.S. and worldwide

U.S. DEPARTMENT OF COMMERCE
Technology Administration
National Technical Information Service
Springfield, VA 22161 (703) 605-6000